Ultracold dysprosium gas in optical dipole traps : control of interactions between highly magnetic atoms

Chayma Bouazza

THÈSE DE DOCTORAT
de l'Université de recherche
Paris Sciences Lettres – PSL Research University

préparée à l'École normale supérieure

Gaz de Dysprosium ultrafroid dans des pièges dipolaires optiques: contrôle des interactions entre atomes fortement magnétiques

Ultracold Dysprosium gas in optical dipole traps: control of interactions between highly magnetic atoms

École doctorale n°564 Physique en Ile de France
Spécialité: Physique Atomique et Moléculaire Optique

Soutenue par **Chayma Bouazza**
le 04 Mai 2018

dirigée par **Jean Dalibard**
& **Sylvain Nascimbène**

Composition du Jury :

M Pierre PILLET
LAC - Université Paris-Saclay
Rapporteur

M Bruno LABURTHE-TOLRA
LPL - Université Paris-13
Rapporteur

Mme Leticia TARRUELL
ICFO - The Institute of Photonic Sciences
Mediterranean Technology Park
Examinatrice

M Christoph WESTBROOK
LCF - Institut d'Optique Graduate School
Président du jury

M Jean DALIBARD
Directeur de thèse

M Sylvain NASCIMBENE
Co-directeur de thèse

ENS | PSL RESEARCH UNIVERSITY PARIS

Résumé

Dans le cadre de cette thèse, j'ai étudié le refroidissement et le piégeage d'un gaz d'atomes de Dysprosium dans des potentiels lumineux. Cet atome lanthanide possède dans son état électronique fondamental un moment magnétique très élevé, permettant l'exploration du domaine des gaz dipolaires ultrafroids. Ce caractère dipolaire enrichit la gamme des phénomènes physiques réalisés expérimentalement, en tirant avantage de la nature anisotrope et à longue-portée de l'interaction entre dipôles magnétiques. De plus, grâce à sa structure électronique riche, le Dysprosium offre la possibilité de créer un fort couplage entre le spin atomique et des champs lumineux, tout en gardant un taux de chauffage faible par rapport au cas usuel des atomes alcalins. Ceci ouvre la voie vers l'implémentation de champs de jauge artificiels, qui suscitent un vif intérêt dans le domaine des atomes froids dans un contexte de simulation quantique. Ce travail de thèse, consiste en l'étude des mécanismes d'interactions dans un gaz de Dysprosium ultrafroid, allant des collisions assistées par la lumière à la relaxation dipolaire en passant par le refroidissement par évaporation. J'expose également la réalisation expérimentale d'un champ magnétique effectif en utilisant un déplacement lumineux dépendant du spin, permettant de contrôler optiquement la force des interactions atomiques au moyen d'une résonance de Feshbach.

Abstract

In this thesis, I present the study of the laser trapping and cooling of a Dysprosium atomic gas. This latter belong to the lanthanide family, it exhibits a large angular momentum in its electronic ground state, making it a suitable candidate for investigating dipolar quantum gases. These systems present a major interest as they can lead to the observation of novel quantum phenomena thanks to the anisotropic and long-range character of the interaction between magnetic dipoles. Moreover, Dysprosium has a rich electronic structure offering the possibility to implement strong light-spin coupling with a reduced heating with respect to alkali species, which paves the way toward the realization of synthetic gauge fields. In this work, I present the experimental investigation of different interaction mechanisms occurring in an ultracold gas of Dysprosium, ranging from light-assisted collisions to dipolar relaxation and evaporative cooling. I expose also the experimental realization of an effective magnetic field, using spin-dependent light-shift, allowing optical control over atomic interactions by means of Feshbach resonances.

Contents

Introduction . . . 1

1 General properties of Dysprosium . . . 9

1.1 Physical properties 9

1.1.1 Electronic configuration . . . 10

1.1.2 Cooling scheme . . . 11

1.1.3 Isotope shift . . . 13

1.2 Interactions in dipolar quantum gases 13

1.2.1 The anisotropic dispersion interaction . . . 13

1.2.2 The dipole-dipole interaction . . . 15

1.2.3 Scattering properties for a cold dipolar gas . . . 16

2 Experiment . . . 19

2.1 Experimental setup 19

2.1.1 The vacuum and laser systems . . . 19

2.1.2 Typical experimental sequence . . . 21

2.2 Trap losses due to binary collisions 27

2.2.1 Light-assisted collisions: models and limits . . . 28

2.2.2 Experimental investigation of 2-body losses in a Dy MOT . . . 32

2.3 Optical dipole trap 36

2.3.1 Experimental setup . . . 38

2.3.2 Measurement of oscillation frequencies . . . 39

2.3.3 Loading the ODT . . . 42

2.4 Optical transport of a thermal cloud 42

2.4.1 Harmonic case . . . 43

2.4.2 The real trap . . . 45

3 Atom-Light interaction: trapping vs heating . . . 49

3.1 Optical light shift and photon-scattering rate 49

3.2 Lifetime and heating in a dipole trap at $\lambda = 1070$ nm 52

3.2.1 Case of a circular polarization . . . 53

3.2.2 Case of a linear polarization . . . 54

3.3 Lifetime and heating in a dipole trap at $\lambda = 626$ nm 57

3.4 Dipolar relaxation 59

3.4.1 Theoretical derivation of the two-body loss rate and its dependence on the B-field . . . 59

3.4.2 Experimental investigation of the dipolar relaxation in a thermal gas . . . 64

4 Interactions between Dysprosium atoms and evaporative cooling . 67

4.1 Forced evaporation in a single far detuned optical beam 67

4.2 Crossed dipole trap 70

4.2.1 Characterization of the crossed dipole trap . . . 70

4.2.2 Optimizing the loading into the cross dipole trap . . . 73

4.3 Controlling the interactions via Feshbach resonances 75

4.3.1 Nature of Dy Feshbach spectrum . . . 78

4.3.2 Characterization of a Feshbach resonance . . . 79

4.4 Forced evaporation in the cross dipole trap 81

4.4.1 Evaporation model . . . 82

4.4.2 Gravity effects on the evaporation efficiency . . . 85

4.4.3 Interaction effects on the evaporation efficiency . . . 86

4.5 Heating in the cODT 89

5 Manipulating the atomic spin with light . . . 93

5.1 Spin-dependent light-shift 93

5.2 Calibration of the coupling strength 95

5.3 Effective magnetic field 98

Conclusion and perspectives . . . 103

A Design of the transport acceleration profile 111

B Article: Optical cooling and trapping of highly magnetic atoms: the benefits of a spontaneous spin polarization 114

Bibliography 138

Introduction

" The rare-earth elements perplex us in our researches, baffle us in our speculations, and haunt us in our very dreams. They stretch like an unknown sea before us, mocking, mystifying and murmuring strange revelations and possibilities", describes Sir William Crookes, a british chemmist, in 1887. Rare-earth elements continue to intrigue us thanks to their peculiar features, and with their emergence in the field of ultracold quantum gases about ten years ago, they opened the door for exploring a diversity of new phenomena. Apart from Ytterbium (Yb) the rare-earth elements, also known as lanthanides, have a non vanishing total angular momentum in the ground state providing them with quite interesting properties such as a sizable permanent magnetic moment. Thus they make a suitable candidate for studying dipolar quantum gases. These latter expand the scope of ultracold atom experiments by introducing two main features: long-range and anisotropic interactions. The emergence of dipolar gases field was driven by the search for novel quantum many-body phenomena (quantum ferrofluids [1], roton instability [2, 3],...) that would arise from the long-range and anisotropic dipole-dipole interaction (DDI) in contrast to the usually considered short-range and isotropic contact interaction at very low temperatures. A second consequence to the large angular momentum of lanthanides is the richness of the excitation electronic structure, offering various experimental possibilities based on the interaction of the spin with complex light fields.
In the course of this thesis work, we are interested in the Dysprosium (Dy) atomic specie, an element with unsurpassed magnetic dipole moment among all neutral atoms.

Ultracold systems: a unique platform for investigating many-body hamiltonians

The achievement of Bose-Einstein condensates (BEC) [4, 5] in 1995, followed few years after by the successful realization of a degenerate Fermi gases (DFG) [6, 7], these

tremendous progresses mark a turning point in the field of quantum atomic, molecular and optical (AMO) physics. Ever since, great experimental efforts have been made, leading to the observation of a series of fascinating phenomena from which we can cite the superfluid to the Mott-insulator transition [8], the detection and manipulation of single atoms using quantum gas microscopes [9, 10, 11, 12], the realization of low dimensionality systems [13, 14, 15, 16] and the list continues to grow. These experimental developments in the ultracold quantum gases field stimulated an intensive theoretical investigation as well, resulting in the prediction of novel quantum states, for example supersolid systems or topological quantum matter [17, 18, 19].

The high control and flexibility achieved experimentally in ultracold atom experiments make them ideal for studying many-body hamiltonians both in the mean field regime (in degenerate dilute gases) and the strongly correlated limit (*eg.* in optical lattices). It is possible to tune different degrees of freedom of the studied system by means of external fields (magnetic, electric and optical). For example, the interactions between particles can be scanned in strength and even change sign (attractive or repulsive interaction) using Feshbach resonances, by applying an external magnetic field. Feshbach resonances were used to study of the BEC-BCS crossover in superfluid Fermi systems [20, 21] and to create molecules formed from ultracold atoms [22]. The internal state of the atom can be controlled also using laser beams, radio-frequency or microwave fields. In addition, selecting any desired spatial geometry for the system is nowadays possible making use of recent developed technologies, for example spatial light modulators or digital micromirror devices, allowing for potential shape tailoring [23].

This rich and versatile *toolbox* made it possible to implement and study topics normally encountered in condensed matter physics, such as the Ising model [24], electronic transport in metals [25, 26] and even systems that gained an increase interest in solid state field lately like graphene [27, 28].

The idea of mimicking condensed matter systems with ultracold quantum gases is very appealing since they offer an unprecedented clean and tunable platform for investigating different phenomena. This concept of simulating the physics of a complex system with a simplest one provided that both evolve with similar hamiltonians is reminiscent of the proposal made by Feynman in 1982 [29]. Quantum simulation [30] and quantum computation [31] are among the biggest challenges for the ultracold quantum gases community.

What could dipolar gases bring to the field?

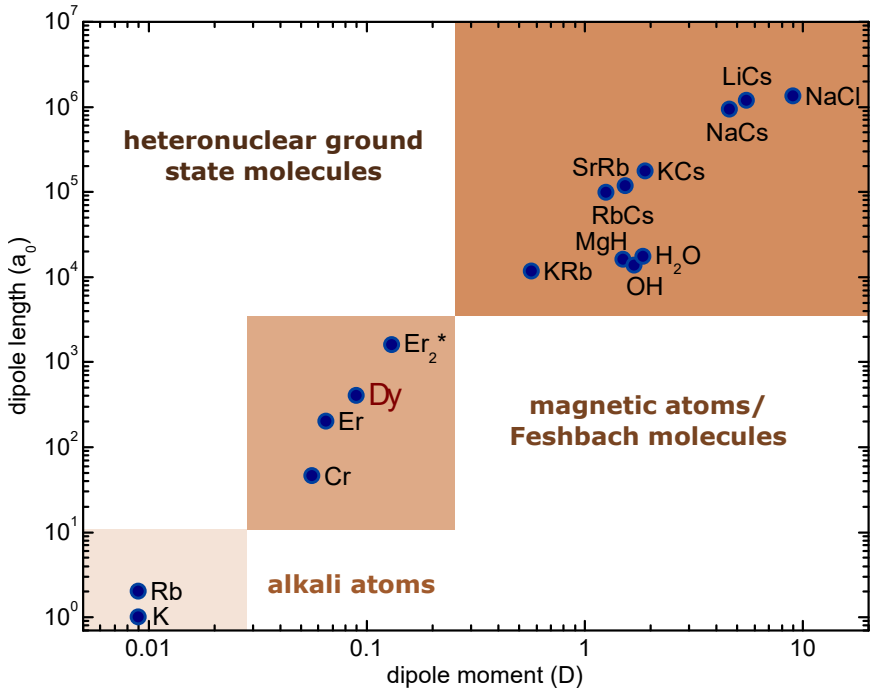

***Figure 1** – A span of the experimentally achievable dipolar systems. Alkali atoms are included for comparison. The dipolar scattering length is presented as a function of the dipole moment (expressed in Debye). One should include also Rydberg atoms which have large electric dipole moments of tens of thousand Debye (out of scope on this graph). This graph is taken from ref. [32].*

As it was mentioned above, dipolar quantum gases introduce long-range and anisotropic interactions between particles which enrich the spectrum of what can be achieved in cold atom systems (Fig. 1 presents a span of different dipolar systems achieved experimentally). The successful laser cooling of magnetic atom Chromium (Cr) in 2005 [33] was the first experimental realization of a dipolar BEC that lead to the observation of a large span of dipolar effects at the many-body level, ranging from the anisotropic deformation of the expanding BEC [34] to the collapse of the BEC in *d*-wave due to dipole-dipole interactions (DDI) [35]. Nevertheless, strong dipolar regime was reached only in the vicinity of Feshbach resonances where the contact interaction, naturally dominant for Cr, can be reduced. We emphasis here the ability offered by ultracold systems to tune the interplay between the long-range anisotropic DDI and the short-range isotropic contact interactions.

In 2011, Dysprosium was brought to degeneracy in the group of B. Lev [36], followed by the Bose-Einstein condensation of Erbium (Er) [37], another element from the lanthanide

family. Both atomic species exhibit a large magnetic dipole moment ($\mu = 10\ \mu_B$ and $7\ \mu_B$ for bosonic Dy and Er in their ground states, respectively). For Dy, DDI is naturally the leading term for interaction potentials allowing the manifestation of a strongly dipolar character; a fascinating example of this manifestation was the observation of self-bounded quantum droplets [38], a novel quantum state produced for the first time in an ultracold quantum gas.

Dipolar quantum gases are also interesting for studying the unconventional maxon-roton dispersion spectrum under proper parameters [39, 40], in close analogy to the excitation spectrum in a superfluid liquid Helium, that has been studied by Landau [41] and by Feynman [42] few years later. In such a system, excitations with low momenta are acoustic phonons for the lowest energy branch, while at higher momenta, the dispersion relation exhibits a local maximum and a minimum with elementary excitations called maxons and rotons, respectively. These type of excitations would arise from the interplay between attractive and repulsive interactions in a Bose gas.
Let us consider a dipolar BEC trapped in a pancake-shaped potential with the dipoles oriented perpendicularly to the trap plan. It was shown in ref. [39] that the BEC can be dynamically stabilized if a strong short-range repulsive interaction is present, otherwise the BEC becomes unstable if its density exceeds a critical value n_c. We can understand this instability in the following way: in the strong dipolar regime, the atoms feel the 3D nature of the DDI interaction despite the quasi-2D trap and for a large atomic density, the BEC collapses. Interestingly, the dispersion relation for a stable BEC has a minimum, in a tight analogy to the roton minimum of Helium (the observation of a roton mode population in a dipolar quantum gas of Er was reported recently [3]). Here it is important to note that the instability expected in the presented above configuration is fundamentally different from the one occurring in a condensate with an attractive short-range interaction (when the scattering length is negative). In the latter, the chemical potential is negative and the ground-state does not exist. On the contrary, the chemical potential is positive for a dipolar BEC and the instability results from the momentum-dependent effective coupling strength. The presence of a roton minimum, just below the instability critical point, suggests the existence of a new ground-state that has a wave order density, a key feature in a supersolid state [43]. It was shown theoretically that the supersolid state in a dipolar BEC is unstable and that the BEC undergoes a series of local collapses due to the roton instability [44, 45]. However, it is predicted that the system can be stabilized

in the presence of a single component polarized Fermi gas [46]. Dysprosium is thus an ideal candidate for implementing such a system as it comes naturally with five relatively abundant isotopes, three bosons and two fermions that were all successively brought to degeneracy.

Another interesting implementation of a dipolar quantum gas would be loading it in an optical lattice [47, 48]. These artificial crystals produced by interfering light fields gained major experimental and theoretical interest in the past decade given its features permitting the simulation of perfect solide state crystalline structure [49]. These systems were used to enter the strongly correlated regime. However the inter-particle interaction remained short-ranged and effective long-range character was mediated by presence of the optical lattice. In contrast, the implementation of such systems with dipolar gases would result in a real next-neighbour interaction [47, 50, 51].

Dysprosium, an ideal candidate for creating artificial gauge fields

As it was explained above, ultracold gases are suitable for performing quantum simulation. However, the charge neutrality of atoms is a limiting factor preventing the observation of a large variety of intriguing phenomena that exist in condensed-matter physics and that arise usually from the Lorentz force, for example the fractional quantum Hall states in a 2D electron system. Nevertheless, it is possible to circumvent this limitation by creating a hamiltonian mimicking the interaction between a charged particle and an applied magnetic field. One can exploit the analogy between the Lorentz and Coriolis forces to create a synthetic magnetic field. The scheme in which the atomic sample is spatially rotated was implemented both in a Bose gas [52] and in a Fermi gas [53]. The emergence of vortices was the manifestation of the synthetic field creation, although the high field regime remained out of reach due to the limited rotation speed achieved experimentally. Another alternative would be to dress the atomic state with light. In the quantum physics formalism, the hamiltonian describing the state of a single particle can be written as:

$$H = \frac{\hbar^2}{2m}\left(\mathbf{k} - \frac{q\mathbf{A}}{\hbar}\right)^2$$

where $\mathbf{A}$ is the vector potential such that $\mathbf{B} = \nabla \times \mathbf{A}$. In comparison to the Lorentz force ($F_L = v \times q\mathbf{B}$), only the terms $q\mathbf{B}$, $q\mathbf{A}$ are relevant. Hence, a synthetic magnetic

field would arise from the creation of a spatially dependent vector potential. This spatial variation can be generated thanks to an opticall dressing of the atomic state with the appropriate configuration [54]. Such atom light coupling links the spin of the particle to its momentum, or the so called spin-orbit coupling (SOC). This scheme was implemented with alkali atoms [55]. In this system a major limitation is the resulting large heating rate due to the increasing photon scattering rate when the frequency of the dressing optical field is tuned close to the atomic transition or when its intensity is increased; making the high field regime out of reach. Using Dy instead turns out to be more efficient. Thanks to its large spin and narrow optical transitions, it is conceivable to generate a synthetic magnetic field with a comparable magnitude to the one achieved with alkalis but with a drastically reduced heating rate [56]. In degenerate Fermi gas, a SOC is predicted to induce p-wave pairing in a superfluid [57], hence the topology of the Fermi surface is modified. The realization of a such topological superfluid paves the way towards the observation of exotic edge states known as Majorana fermions [58, 59]. SOC was implemented experimentally with alkali metals atom (Potassium and Lithium) [60, 61], the limitation for long observation times remained the large heating rate. The experimental realization of a such scheme with Dy fermionic isotope confirmed the possibility of obtaining a long-lived spni-orbit coupled DFG [56].

Spin-dependent interactions

In the field of ultracold gases, the use of optical fields to control the atomic state proved to be an efficient tool. The atom-light interaction is governed by the atomic polarizability on the one hand, and by the optical beam parameters on the other hand. The atomic polarizability is an intrinsic feature of the atomic specie and it is fixed by its electronic configuration. The polarizability comprises three different contributions: a scalar, vector and a tensor part. In the presence of a light field, the resulted interaction between the latter and the atom can by described by the sum of three operators:

$$U_{\text{tot}} = U_s + U_v(\hat{\mathbf{u}}, \hat{J}) + U_t(\hat{\mathbf{u}}, \hat{J}^2)$$

where $\hat{\mathbf{u}}$ is the light polarization unit vector and $\hat{J}$ is the total angular momentum operator. The first operator U_s is independent of the atom internal state, it has an effect of shifting the different spin levels energies by an amount only determined by the light intensity.

In contrast with this scalar operator, the vector U_v and tensor U_t operators depend on the spin of the atom and the light field polarization. This dependency can be used to perform spin selective interaction. In comparison to the case of alkali atoms for which the tensor contribution is negligible, Dy possesses a sizeable tensor term and the balance between this term and the vector term can be tuned by changing the polarization of the optical field. One can take advantage of the flexibility of the atom-light coupling to create non-classical states. For example, we recently generated a coherent superposition between the two maximally stretched spin states with opposite orientation ($|-J\rangle$ and $|J\rangle$). For Dy, $J \gg 1$, hence this state can be considered as a Shrödinger-cat state, *i.e.* a coherent superposition between two quasi-classical states well separated in phase space.

Outline

In this thesis, I will study different types of interactions in a dipolar gas of the bosonic isotope ^{164}Dy and how to control them. The manuscript is organized as follows:

Chapter 1 In this chapter, I give a general description of Dysprosium physical properties (electronic configuration, isotopes, *etc*). I set forth different types of interactions present in a Dy gas, mainly the short-range contact interaction and the long-range dipole-dipole interaction. I discuss the effects of anisotropy on both types of interactions.

Chapter 2 In the first part of this chapter, I expose briefly the experimental setup. I discuss the peculiarity of a Dy magneto-optical trap (MOT) and focus on light-assisted collisions in such a system. In the second part of the chapter, I describe the optical trapping by means of a far detuned beam, that is used to transport atoms from the MOT chamber to the science cell. The study of the transport sequence is also presented and I show that there are optimal transport durations that minimize the centre of mass excitation at the end of the displacement.

Chapter 3 Two main points are studied in this chapter: anisotropy effects on atoms in optical dipole traps and dipolar relaxation, that play a major role in Dy atomic gases. For the first point, I present the experimental investigation of the induced heating in both far detuned optical dipole trap and a trap working close to an atomic transition

at $\lambda = 626$ nm. The observed dependency on the light polarization is linked to the anisotropy of the atomic polarizability. As for the second point, I study the manifestation of the dipolar character of Dy through dipolar relaxation and its variation with the applied magnetic field.

Chapter 4 In this chapter, I describe the dynamics of the system during an evaporative cooling process. I discuss the effects of different physical parameters (gravity, interactions, *etc*) on the evaporation efficiency and discuss the limits. I present also the peculiarity of Dy Feshbach spectrum and focus on a relatively large resonance that can be used to tune the interaction in the system.

Chapter 5 This chapter deals with spin-dependent atom-light interaction in a Dy gas. I show that we can exploit this dependency to create an effective magnetic field. This effect is confirmed by the observation of a Feshbach position shift in the presence of a light field. Furthermore, we recover the Feshbach resonance by scanning the intensity of the optical beam instead of scanning a magnetic field, which could be implemented in future work on the BEC.

Chapter 1

General properties of Dysprosium

The early works on laser cooling techniques [62] opened the door for studying many-body physics with a high degree of control. Experiments mainly used alkalies species driven by the simplicity of their electronic configuration. However, implementing schemes with other species, such as the open-shell lanthanide atoms, can lead to the observation of a rich span of many-body phenomena, thanks to their peculiar features: large angular momenta, rich electronic excitation spectrum, *etc*. In our experiment, we use the highly magnetic Dysprosium atom. The group of B. Lev (Stanford) was the first to obtain a Bose-Einstein Condensate (BEC) in 2011 [36] and a Degenerate Fermi Gas (DFG) one year later [63], then followed by the group of T. Pfau (Stuttgart). Our experiment is the third to be built. Ever since more and more groups are using Dy or other atoms with similar properties like Erbium (Er) or Thulium (Tm), proving that the atomic elements of the lanthanide family open the door to new perspectives in the field. In our experiment, a particular interest is given to the interaction between the large spin of Dy and near resonant light.
The aim of this chapter is to introduce the properties of Dy and give the important parameters for its cooling and trapping.

1.1 Physical properties

Dysprosium was identified for the first time by a french chemist, Paul Émile Lecoq de Boisbaudran, in 1886 when he succeeded in separating this new element from a sample of Holmium. The origin of the appellation Dysprosium comes from Greek δυσπροσιτος (dusprósitos) which means *hard to get* as it was difficult to isolate from the Holmium. The first

pure sample of Dy was obtained in 1950. Dysprosium belongs to the lanthanide family (*cf.*

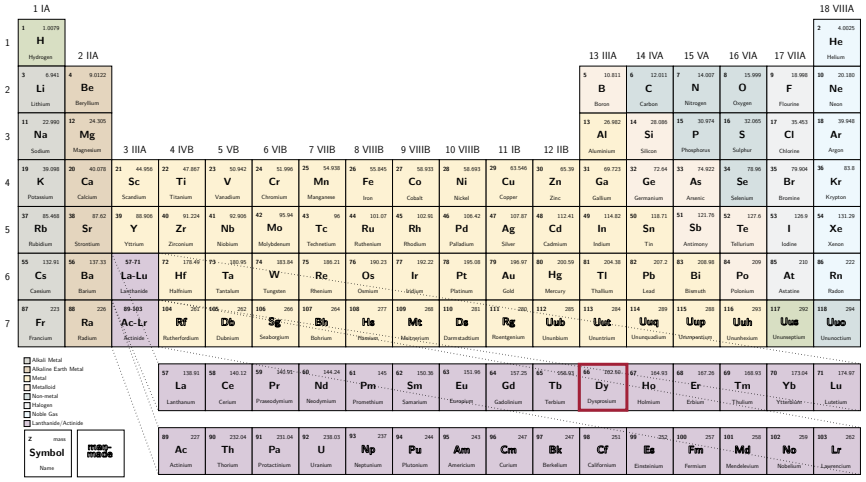

***Figure 1.1** – Periodic table of chemical elements*

Fig. 1.1) with an atomic number $Z = 66$. It has seven stable isotopes, which are reported in Tab. 1.1. The existence of four isotopes with a relatively similar natural abundance is of a great interest in the field of cold atoms as it is possible to study different systems (Bose gas, Fermi gas, mixtures, *etc*) with the same experimental setup. In this work, we will mainly discuss the study and production of ultracold ^{164}Dy samples.

Isotope	^{156}Dy	^{158}Dy	^{160}Dy	^{161}Dy	^{162}Dy	^{163}Dy	^{164}Dy
Natural Abundance	0.06 %	0.1 %	2.3 %	18.9 %	25.5 %	24.9 %	28.3 %
Quantum Statistics	boson	boson	boson	fermion	boson	fermion	boson

***Table 1.1** – Stable isotopes of Dysprosium*

1.1.1 Electronic configuration

Following the Madelung rule for filling the electronic orbitals, one gets that the ground state configuration is $[\mathrm{Xe}]4f^{10}6s^2$. The 4f shell has seven available orbitals ($l = 3$, $|m_l| \leq 3$) for only 10 electrons. According to the Hund rule, the electronic configuration with the lowest energy is the one maximizing the orbital angular momentum L and the spin momentum S:

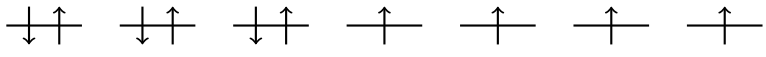

$m_l = \text{-}3$ $m_l = \text{-}2$ $m_l = \text{-}1$ $m_l = 0$ $m_l = 1$ $m_l = 2$ $m_l = 3$

It results in an orbital angular momentum $L = 6$, a spin $S = 2$ and a total angular momentum $J = L + S = 8$. Fermionic isotopes have in addition a nuclear spin $I = 5/2$. This large angular momentum confers important characteristics on Dy, mainly an unsurpassed magnetic moment $\mu \simeq 10\ \mu_B$ with μ_B is the Bohr magneton (Dy magnetic moment is 10 times larger than the one for alkali atoms and it is the largest among neutral elements of the periodic table), hence Dy is a quantum dipolar gas suitable for studying dipolar interactions. It posesses a rich excitation spectrum (a fraction is presented in Fig. 1.2) offering several cooling schemes. In 1970, John Conway and Earl Worden gave a quite detailed description of the Dy spectrum in the University of California Radiation Laboratory Report UCRL-19944, where they listed more than 22000 lines between 230 nm and 900 nm for the neutral and singly-ionized Dysprosium DyI and DyII (*cf.* ref. [64] for more details). The values of the ground state angular momentum J and Landé's factor g were determined experimentally by Cabezas *et al.* in 1961 [65]. These measurements are considered to be the first experimental proof that the ground state level is the $4f^{10}6s^2\ (^5I_8)$. Dy is also used in aeronautic and the production of permanent magnets. And from the fundamental physics point of view, Dy is a promising candidate for realizing P and P-T violation experiments, as it has a pair of almost degenerate levels with opposite-parity and the same angular momentum ($J = 10$) [66].

1.1.2 Cooling scheme

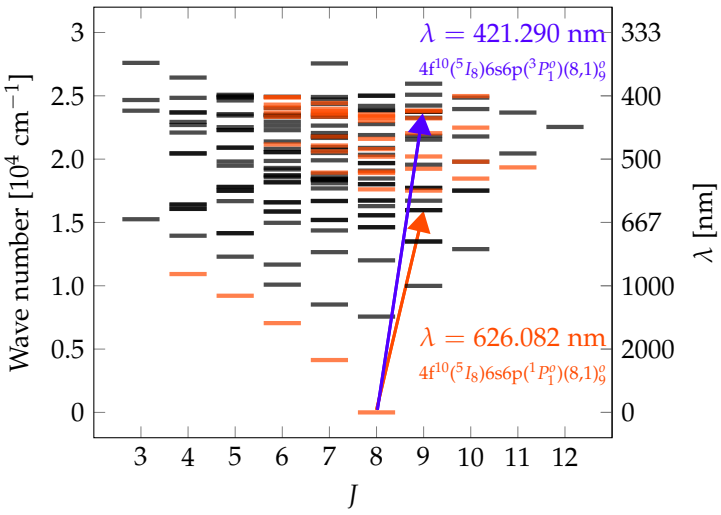

***Figure 1.2** – A glance of Dy's excitation spectrum*

Transition	Blue	Red
Linewidth [$2\pi\times$ MHz]	32.2	0.136
I_{sat} [mW/cm^2]	56.3	72×10^{-3}
T_{Doppler} [μK]	773	3.3
T_{recoil} [nK]	329	149
v_{recoil} [mm/s]	5.8	3.9

***Table 1.2** – Characteristics of the used optical cooling transitions.*

The complexity of the excitation spectrum can be overwhelming at first sight, but from a laser cooling point of view only two transitions are relevant: a broad transition at $\lambda = 421.290$ nm that offers a significant cycling rate ideal for large capture velocities magneto-optical traps (MOTs), Zeeman slowing and imaging, and a relatively narrow transition at $\lambda = 626.082$ nm suited for cold MOTs and atomic spin manipulation (see details in chapter 2). These two transitions result from the promotion of one electron from the outer shell 6s to the excited orbital 6p. For the 421 nm blue transition, the spin is conserved which gives a spectral term $4f^{10}(^5I_8)6s6p(^1P^o_1)$, while it is not for the red transition: $4f^{10}(^5I_8)6s6p(^3P^o_1)$. This latter is a singlet to triplet transition (forbidden) and therefore has a narrow linewidth (*cf.* Tab. 1.2). The coupling between the two angular momenta of the inner shell ($J = 8$) and the outer shell ($J = 1$), gives rise to three excited states with momenta $J' = 7,\ 8$ and 9. A list of the different lines corresponding to these momenta is given in Tab. (1.3). The two excited states that we consider are those with a total angular momentum $J = 9$.

Spectral term	J	λ [nm]	g_J
$4f^{10}(^5I_8)6s6p(^1P^o_1)$	7	404.71	1.26
	8	418.80	1.29
	9	421.29	1.22
$4f^{10}(^5I_8)6s6p(^3P^o_1)$	8	597.61	1.20
	7	599.02	1.22
	9	626.08	1.29

***Table 1.3** – The lines of the $4f^{10}(^5I_8)6s6p(^1P^o_1)$ and $4f^{10}(^5I_8)6s6p(^3P^o_1)$ transitions. J is the total angular momentum of the excited state, λ is the wavelength of the transition in air and g_J is its Landé factor.*

1.1.3 Isotope shift

The charge distribution of the atomic nucleus gets slightly modified for different isotopes. This effect results in an energy shift of the excitation spectrum [67]. The total shift is the sum of a field shift and a mass shift. The first is due to the influence of the nuclear charge distribution on the binding energy of electrons and the second comes from the influence of the nuclear recoil energy. For Dy bosonic isotopes, we measure a shift of $\Delta\nu = \{476, 491\}$ MHz/[m.a.u], for the blue and red transitions, respectively.

1.2 Interactions in dipolar quantum gases

Scattering phenomena play a fundamental role in the study of quantum gases, it is thus important to understand and characterize the different interaction processes. In this section, I will present the main interaction potentials to be considered for a Dy gas: the Van der Waals and the dipole-dipole potentials. We neglect higher order interactions like the electric quadrupole-quadrupole potential as it was shown that it is much weaker than the other two [68]. In the second part of this section, I will recall the expressions of the scattering cross sections for both types of interaction as it will be needed to calculate the collision rate (*cf.* chapter 4).

1.2.1 The anisotropic dispersion interaction

The dispersion potential, also known as the Van der Waals (VdW) potential, arises from the interaction between induced electric dipoles of two atoms and has the following form:

$$U_{\mathrm{VdW}}(r) = -\frac{C_6}{r^6} \tag{1.1}$$

where r is separation between two interacting atoms and C_6 is called the Van de Waals coefficient. This potential is short-ranged and has a spherical symmetry for alkali atoms. For atoms with a strong magnetic character like Dy, the C_6 coefficients depend on the projection of the total angular momentum onto the internuclear axis. The exact calculation of this potential is very challenging for Dy due to the complex electronic configuration, nevertheless numerical simulations have been performed for interacting Dy atoms in their ground states (see refs. [69, 68]).

Let's consider two colliding atoms in their ground states with angular momenta $J_1 = J_2 = 8$. The total angular momentum of the pair is then $J = J_1 + J_2$, and we define Ω to be its projection along the internuclear axis. We consider a weak interaction such that both atoms remain in the $J_1 = J_2 = 8$ manifold after the collision. The matrix elements of the VdW potential are given by [70, 68]:

$$\begin{aligned}
&\left\langle J_1 M_1, J_2 M_2 | U_{\mathrm{VdW}} | J_1 M_1', J_2 M_2' \right\rangle = -\frac{C_6\left(M_1 M_2, M_1' M_2'\right)}{r^6} \\
&= \sum_{\{n_a J_a M_a, n_b J_b M_b\}} \frac{1}{(E_1 + E_2) - \left(E_{n_a J_a} + E_{n_b J_b}\right)} \\
&\times \left\langle J_1 M_1, J_2 M_2 | \hat{V}_{dd} | n_a J_a M_a, n_b J_b M_b \right\rangle \left\langle n_a J_a M_a, n_b J_b M_b | \hat{V}_{dd} | J_1 M_1', J_2 M_2' \right\rangle
\end{aligned} \tag{1.2}$$

where r is the internuclear separation. J_1, J_2 are angular momenta of the two incoming states and M_1, M_2 are their projections along the internuclear axis such that $\Omega = M_1 + M_2$. M_1' and M_2' are the corresponding projections of the outgoing states after the interaction. One has to sum over all electronic states $|n_a J_a M_a, n_b J_b M_b\rangle$ of atoms a and b excluding states with energies equal to the ground states energies E_1 and E_2. J_a, J_b are the intermediate angular momenta for atoms a and b respectively, M_a and M_b are their respective projections along the internuclear axis and n_a, n_b account for the remaining state parameters. $\hat{V}_{dd}$ corresponds to the electric dipole-dipole interaction operator. As we can see from eq. (1.2), the C_6 coefficients depend on the values of M_1, M_2, M_1' and M_2', thus the interaction energy depends on the relative orientation of the atoms. This effect finds its origin in the anisotropic coupling of the unpaired electrons of the 4f shell. The general expression of the C_6 coefficients can be written as [68]:

$$C_6\left(M_1 M_2, M_1' M_2'\right) = \sum_{J_a J_b} K_{J_a J_b}^{J_1 J_2} A_{M_1 M_2, M_1' M_2'}^{J_1 J_2 J_a J_b} \tag{1.3}$$

where

$$\begin{aligned}
A_{M_1 M_2, M_1' M_2'}^{J_1 J_2 J_a J_b} = \sum_{M_a, M_b} &\left(1 + \delta_{M_1, M_a}\right)\left(1 + \delta_{M_1', M_a}\right) \\
&\begin{pmatrix} J_1 & 1 & J_a \\ -M_1 & (M_1 - M_a) & M_a \end{pmatrix} \begin{pmatrix} J_2 & 1 & J_b \\ -M_2 & (M_2 - M_b) & M_b \end{pmatrix} \\
&\begin{pmatrix} J_a & 1 & J_1 \\ -M_a & (M_a - M_1') & M_1' \end{pmatrix} \begin{pmatrix} J_b & 1 & J_2 \\ -M_b & (M_b - M_2') & M_2' \end{pmatrix}
\end{aligned} \tag{1.4}$$

and

$$K^{J_1J_2}_{J_aJ_b} = \left(\frac{1}{4\pi\epsilon_0}\right)^2 \sum_{n_a,n_b} \frac{|\langle J_1 \parallel d_1 \parallel n_aJ_a\rangle\langle J_2 \parallel d_2 \parallel n_bJ_b\rangle|^2}{(E_{n_aJ_a} + E_{n_bJ_b}) - (E_1 + E_2)} \tag{1.5}$$

$\langle \alpha \parallel d \parallel \beta \rangle$ denotes the reduced matrix element of the transition-dipole-moment operator between two levels $|\alpha\rangle$ and $|\beta\rangle$.

The $A^{J_1J_2J_aJ_b}_{M_1M_2,M_1'M_2'}$ coefficients conserve $\Omega = M_1 + M_2 = M_1' + M_2'$, the projection of the total angular moment J along the internuclear axis. The determination of the $K^{J_1J_2}_{J_aJ_b}$ values is the challenging part as it requires a good knowledge of the different transitions frequencies and oscillator strengths from the ground to the various excited states. Numerical calculations show that the C_6 coefficients take values ranging from 1860 to 1890 a.u. depending on the value of Ω.

1.2.2 The dipole-dipole interaction

The presence of a large angular momentum for Dy changes drastically the interatomic interactions. Particles can be considered as magnetic dipoles with a momentum $\mu = \mu_B g_J J \simeq 10\ \mu_B$ for Dy in the ground state. The interaction between two dipoles $\vec{\mu_1}$, $\vec{\mu_2}$ is then mediated by the dipolar potential

$$U_{DDI}(r) = \frac{\mu_0}{4\pi r^3}\left[(\vec{\mu_1}\cdot\vec{\mu_2}) - \frac{3}{r^2}(\vec{\mu_1}\cdot\vec{r})(\vec{\mu_2}\cdot\vec{r})\right] \tag{1.6}$$

where μ_0 is the vacuum permeability and r the internuclear separation. This potential presents two main features: a long-range character through the $1/r^3$ decay (to be compared to the $1/r^6$ decay for the VdW potential) and an anisotropic behaviour as the interaction strength depends on the relative orientation of the dipoles.

In the presence of an external magnetic field that sets the orientation of the dipoles and for identical dipole moments, eq. (1.6) can be written as:

$$U_{DDI}(r,\theta) = \frac{\mu_0\mu^2}{4\pi}\frac{1-3\cos^2\theta}{r^3} \tag{1.7}$$

with θ being the angle between the quantization axis set by the magnetic field and the internuclear axis. The potential vanishes for an angle $\theta \simeq 54.7°$. Also, the potential is negative for $\theta = 0$ *i.e.* the interaction is attractive when dipoles are aligned in a *head to tail* configuration, while it is repulsive when $\theta = \pi/2$ *i.e.* when dipoles are parallel. This

anisotropy of the interaction defines if a BEC is a stable solution of the Gross-Pitaevskii equation (GPE) [35].

1.2.3 Scattering properties for a cold dipolar gas

Elastic collisions assure the thermalization of the atomic cloud, and the efficiency of the evaporation cooling needed to reach quantum degeneracy is strongly related to the collisional rate. The scattering event can be described as a total wave function resulting from the sum over an incoming and outgoing waves [71, 72]. The differential cross-section is given by:

$$\frac{d\sigma}{d\Omega_{\text{solid}}} = |f(\theta)|^2 \tag{1.8}$$

with $f(\theta)$ being the amplitude of the scattered wave. The total cross-section is obtained by the integration of eq. (1.8) over the solid angle Ω_{solid}.

$$\sigma = \frac{4\pi}{k^2} \sum_{l=0}^{\infty} (2l+1) \sin^2 \delta_l \tag{1.9}$$

with k being the wave-number of the incoming wave, l the angular momentum of the outgoing wave and δ_l the phase shift between incoming and outgoing waves at $r \to \infty$. The energy of the collision is $E = \frac{\hbar^2 k^2}{2m_r}$ where m_r is the reduced mass of the atomic pair and it is equal to $m/2$ for identical particles.
For interaction potentials decaying as r^{-i}, the phase shift is proportional to:

$$\delta_l \propto k^{2l+1} \quad \text{for partial waves such as} \quad l < \frac{i-3}{2} \tag{1.10}$$

$$\delta_l \propto k^{i-2} \quad \text{for larger partial waves} \qquad l > \frac{i-3}{2} \tag{1.11}$$

the former is dominant for short-range interaction potentials like the VdW potential and the latter is dominant in the long-range regime. For the VdW potential ($i = 6$) all phase shifts vanish for $k \to 0$ except for $l = 0$ (s-wave). In this case the low-energy interaction is isotropic and it is characterized by a single parameter, the scattering length a:

$$\sigma = 8\pi a^2 \tag{1.12}$$

The value of a can be tuned through an external magnetic field (Feshbach resonances). For a DDI potential ($i = 3$) all phase shifts are proportional to k and therefore all partial waves contribute to the scattering cross-section.

This extra potential introduces a new length scale to the system, the dipolar length:

$$a_D = \frac{\mu_0 \mu^2 m}{12\pi\hbar^2} \simeq 130.8\, a_0 \tag{1.13}$$

which for ^{164}Dy in its ground state has a comparable magnitude to the background scattering length a_{bg}. The dipolar interaction strength is often described as the ratio of a_D by a, $\epsilon_{dd} = a_D/a$ on the order of 1.3 for $a = a_{\mathrm{bg}}$. This means that naturally the DDI is the dominant interaction which is interesting for studying dipolar gases without making use of Feshbach resonances which are accompanied by atom losses due to three-body recombination (*cf.* chapter 4).

Dipolar scattering theory predicts a universal behaviour of the elastic cross-section at low energy [73, 74]. It exists two different regimes:

- **low energy collisions:** the cross-section is constant and set by the dipolar moment and atomic mass.
- **high energy collisions:** $\sigma \sim a_D/\kappa$, with κ being the wave-number of the relative motion of the colliding partners.

The transition between the two regimes occurs at $E_D = \frac{\mu_0\mu^2}{4\pi a_D^3}$. $E_D/k_B \simeq 185\ \mu$K ($\simeq$ 3.8 MHz) for ^{164}Dy, hence we are always in the low collision energy regime. The constant values of the cross-sections in the regime $E < E_D$ are given by [75, 76, 77]:

$$\sigma_B = \frac{32\pi}{45} a_D^2 + 8\pi a^2 \quad \text{for identical bosons (sum over even partial waves).} \tag{1.14}$$

$$\sigma_F = \frac{32\pi}{15} a_D^2 \quad \text{for identical fermions (sum over odd partial waves).} \tag{1.15}$$

To conclude, the presence of the dipole-dipole interaction changes drastically the properties of a quantum gas. The long-range and anisotropic characters expand the scope of ultracold atom experiments and attract considerable attention.

Chapter 2

Experiment

Lanthanide atoms have a complex electronic structure with respect to alkali species but cooling schemes still relatively simple [78, 79, 80, 81]. In our experiment, only two optical transitions are used: the broad transition at $\lambda = 421$ nm that has a natural linewidth $\Gamma = 2\pi\times$ 32 MHz, and the narrow-line transition at $\lambda = 626$ nm, with a natural linewidth $\Gamma = 2\pi\times$ 136 kHz. The first transition is used for the Zeeman slower (ZS), the transverse cooling and for the imaging, and the latter is used for the magneto-optical trap (MOT) and further atomic spin manipulation.
This chapter sets forth the different cooling stages in our setup. In the first section, I will give a short summary of the general features of the experimental apparatus and cooling lasers as well as the experimental sequence. A more detailed description of the experimental setup can be found in Davide Dreon's Ph.D. thesis [82]. The study carried on light-assisted collisions in the MOT will be discussed in the second part of this chapter. In the last part, I will detail the procedure for trapping and transporting atoms by mean of an optical dipole trap (ODT).

2.1 Experimental setup

2.1.1 The vacuum and laser systems

Our vacuum system (shown in Fig. 2.1) can be decomposed in two sections separated by a differential pumping stage: the high vacuum part (HV) which pressure is on the order of 10^{-8} mbar, and the ultra-high vacuum part (UHV) with a pressure two orders of magnitude lower.

- The HV section comprises the oven and spectroscopy chambers. Our oven is a commercial double effusion cell. We refill the crucible with $\sim$ 10 g of metallic Dy crumbs every six months approximatively. The sample is heated to 1050 °C in order to obtain an atomic jet (the melting point of Dy is 1412 °C at atmospheric pressure). The oven is shielded and water cooled in order to keep it at room temperature during operation.

  After exiting the oven, atoms enter a cubic chamber where we perform spectroscopy on the red, λ = 626 nm narrow transition. We use a technique based on the fluorescence Lamb-dip to lock the MOT laser. We have a 40 L ion pump connected to this chamber. Then atoms cross an octagonal chamber where we carry out spectroscopy on the blue transition λ = 421 nm. We use a modulation transfer spectroscopy technique to lock the laser, which allows us to reach a stability of 1 MHz on the blue line. In this chamber we implement also transverse cooling of the atomic beam.

- There are three main parts in the UHV section: the Zeeman slower, the MOT chamber and finally the science cell. We installed a gate valve at the entrance of the ZS that offers the possibility to open and refill the oven without affecting the vacuum in the UHV section. We have also a mechanical shutter that permits to block the atomic jet if needed. At the same level, we implemented a second ion pump. Typical pressure in this region is 5×10^{-9} mbar. At the exit of the 50 cm long ZS, atoms enter the MOT chamber. It is a cubic piece with CF60 windows on the facets and CF16 connections on the vertices. A third ion pump is connected to this chamber, and the typical pressure is 4×10^{-10} mbar. The final piece of our vacuum system is the glass cell. It is connected to the MOT chamber through a custom T-shape piece. At the level of this piece we have a hybrid ion-getter pump that assures a pressure below 10^{-11} mbar. The glass cell has parallelepiped shape with 6 cm long, 2.5 cm large and 5 mm thick, with no coating.

The used lasers are: a commercial Toptica laser[a] for the blue transition and a home made laser for the red transition. This latter is obtained by a sum-frequency generation of $\lambda_1 = 1050$ nm and $\lambda_2 = 1550$ nm using a non-linear crystal.

[a] TA-SHG Pro, TOPTICA Photonics AG

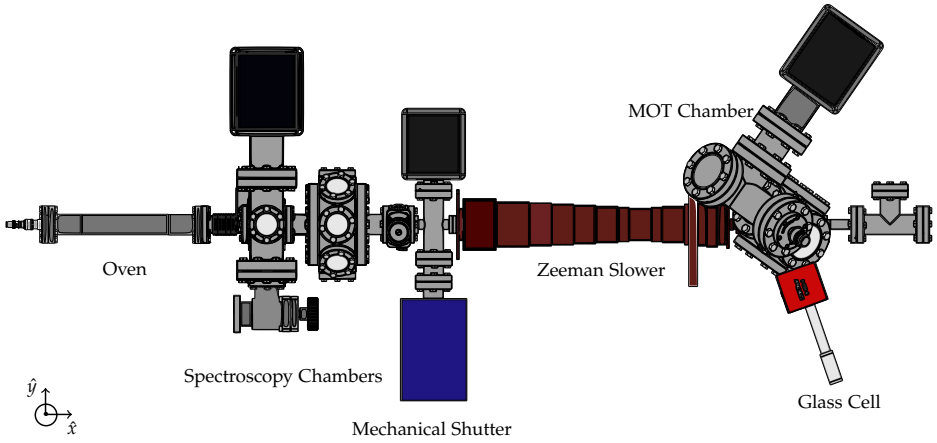

***Figure 2.1** – Top view of the vacuum system*

2.1.2 Typical experimental sequence

In this section, I will concentrate only on the first stage of the experimental sequence: from the MOT loading to the transport of atoms to the glass cell. Further manipulations taking place in the glass cell will be discussed in chapter 4 and 5.
At the exit of the oven, atoms have a typical velocity of $v \sim 520$ m/s. Therefore multiple cooling steps are necessary in order to load the MOT which has a capture velocity on the order of $v_c \sim 8$ m/s[a].

Transverse cooling

We start with a 2D-cooling scheme that enhances the collimation of the atomic beam by reducing the transverse velocity of the particles and thus increases the atomic flux in the MOT chamber. We apply two retro-reflected blue beams perpendicularly to the atomic trajectory. The beams have an elliptical shape with an aspect ratio of 1 : 3, a detuning $\Delta = -\Gamma_{\text{Blue}}/2$ and a power P $\sim$ 50 mW per beam ($I/I_{\text{sat}} \simeq$ 1.13). The implementation of the transverse cooling increases the atom number loaded in the MOT by a factor 2.5, as shown in Fig. 2.2.

Zeeman slower

The deceleration of atoms to the MOT capture velocity takes advantage of the radiation pressure force as they undergo multiple absorption/emission cycles. We send a resonant blue beam in the counter-propagation direction of atoms with a typical power of 60 mW.

[a]This low capture velocity is due to the narrow linewidth of the MOT transition ($\Gamma_{\text{Red}} = 2\pi \times 136$ kHz).

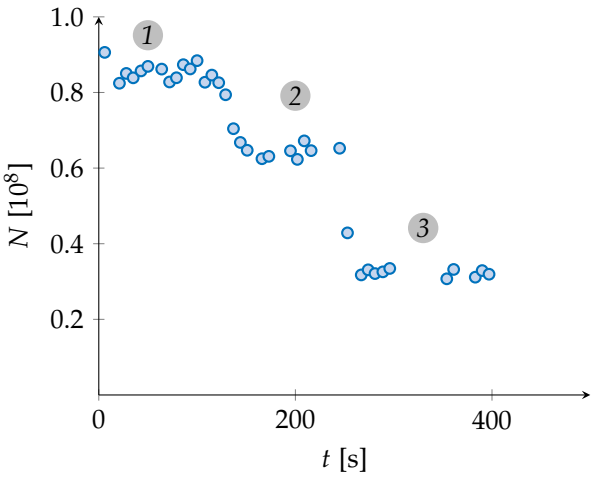

Figure 2.2 *– Measured atom number in the MOT with: 1) Transverse cooling at full power, 2) Transverse cooling at half power and 3) without transverse cooling.*

Along their path, atoms slow down such that their Doppler shift brings them out of resonance. To compensate for this effect, we use a well designed magnetic field that shifts Zeeman levels such that the resonance condition is always fulfilled.

Magneto-optical trap

We prepare the MOT in two steps: a loading phase followed by a compression phase. Fig. 2.3 shows a typical loading sequence. During the first step, we enhance the loading by artificially brodening the red transition linewidth. This is done by modulating the MOT light at a frequency $\nu = 135$ kHz over a total range of 6 MHz. This technique allows us to increase the atom number in the MOT by a factor of 2. We load up to 3×10^8 atoms. At the end of the 7 s loading step, we ramp down the modulation as well as the power of the MOT light and the detuning in order to obtain a colder and denser cloud. The reached values of the intensity and detuning at the end of the compression phase are critical for the ODT loading. We realized a full study of the MOT behaviour under different regimes and we developed a model based on rate equations [83] (*cf.* Appendix B). Here, I will only expose the main results of this study.

The peculiarity of a Dy MOT with respect to an alkali MOT is the linewidth of the transition on which it is operating ($\Gamma_{\text{Red}} = 2\pi \times 136$ kHz against few MHz for alkalis) and the large spin of the atom (J = 8 in the ground state for the bosonic isotope). These two features lead to a complex dynamic of the MOT. The narrow linewidth of the red transition results in a weak optical force. The radiative pressure force along the vertical

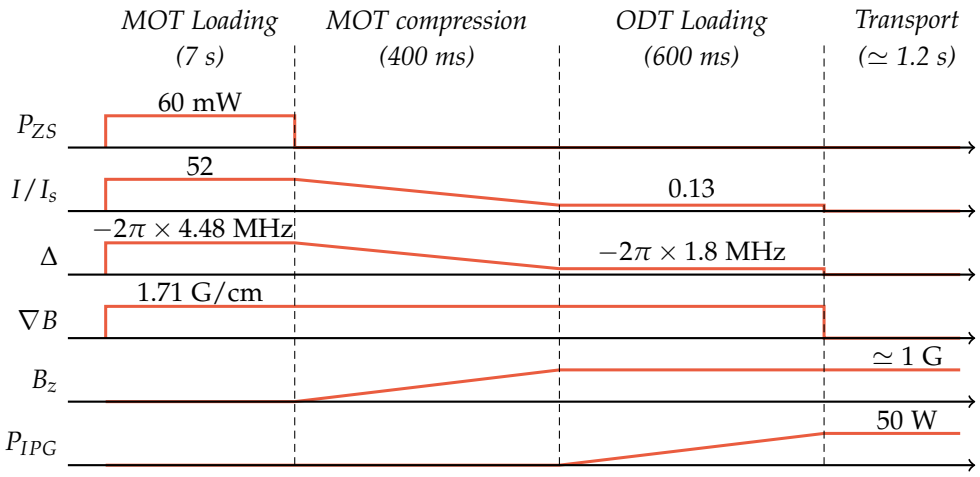

Figure 2.3 *– Typical experimental sequence: only the first stage (from the MOT loading to the transport) is presented here. P_{ZS} is the power of the Zeeman slower beam, I/I_s is the saturation parameter per MOT beam, Δ is the MOT laser detuning from the atomic resonance, ∇B is the magnetic field gradient, B_z is a vertical bias magnetic field and P_{IPG} is the power of ODT beam.*

direction z around equilibrium position z_c and for an atom at rest is given by

$$F_z = \frac{\hbar k \Gamma}{2} \frac{s}{1 + 2s + 4\Delta_{\text{loc}}^2/\Gamma^2} \tag{2.1}$$

with $s = I/I_s$ being the saturation parameter per beam (the saturation intensity for the red transition $I_s = 72\ \mu\text{W/cm}^2$) and $\Delta_{\text{loc}} = \Delta - \delta\mu Bz/(2\hbar)$ is the local detuning at a position z, taking into account the laser detuning Δ and the Zeeman shift. Note that this expression corresponds to half the radiative force from a laser beam oriented upwards, of saturation parameter $2s_0$, and this is due to the geometry of our MOT beams.

When the laser detuning (intensity) increases (decreases), the optical force gets weaker and gravity starts to play a key role. The MOT begins to fall under the effect of the latter, as one can see in Fig. 2.4.*a*, and it equilibrates in a region far from the zero of the quadrupole magnetic field. Then the splitting between different Zeeman sub-levels increases and transitions other than the one between $|J = 8, M_J = -8\rangle$ and $|J' = 9, M'_J = -9\rangle$ get inhibited, as they become far detuned. This mechanism leads to a spontaneous spin polarization of the sample in the absolute ground state. This behaviour was observed also in a narrow-line Er MOT [80]. The interplay between trapping forces and gravity was studied in ref. [84] for a Sr MOT. Our model is inspired from this work to which we add effects due to the large spin.

In the *spin-polarized* regime (for large detunings), we recover a simple 2-level system and

the problem can be solved analytically. We get that the temperature becomes independent from the detuning and can be written as:

$$T = \alpha \frac{\hbar\Gamma}{k_B} \frac{s\eta}{2\sqrt{s\,(\eta - 2) - 1}} \tag{2.2}$$

with α a coefficient taking into account the geometry of our MOT beams and $\eta = \frac{\hbar k\Gamma}{2mg} \sim 168$ the ratio between the radiative force and the gravity (η is on the order of 10^5 for alkalis).

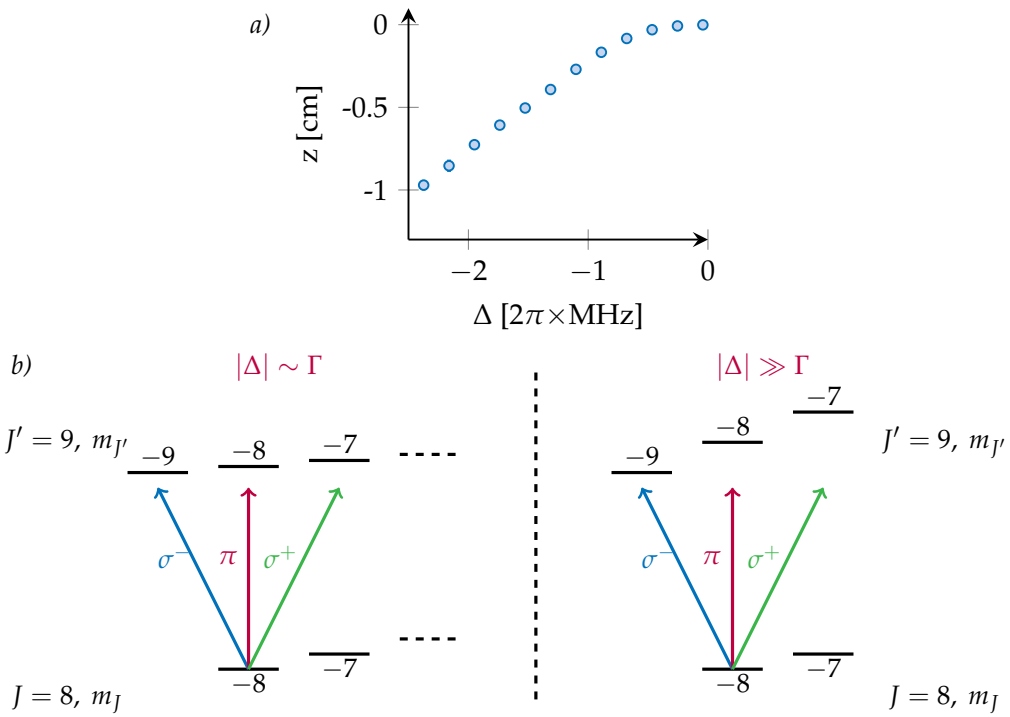

Figure 2.4 *– a) MOT's vertical position as function of the laser detuning. b) Schematic of the lowest Zeeman sub-levels in the case of a small (left) or large laser detuning (right).*

In Fig. 2.5.*a* the measured temperature as function of the detuning for a saturation parameter s = 0.65 and a magnetic field gradient ∇B = 1.71 G/cm is shown. We can see that the temperature becomes independent of the detuning for $|\Delta| > 2\pi\times1$ MHz. The solid black line represents the expected value for the simple 2-level model.

The temperature as a function of the saturation parameter is shown in Fig. 2.5.*b*. The measurement is done at a detuning $\Delta = -2\pi\times1.8$ MHz and with the same gradient. The solid line curve is obtained from the 2-level simple model and the dashed line curve is the expected temperature value when taking into account heating due to intensity fluctuation

in the low field regime. The theoretical curve reproduces the overall behaviour but we see a clear deviation from the model for large intensities. This deviation is due to the fact that the sample does not remain spin-polarized due to optical pumping, hence the 2-level model breaks down. In fact in our model we calculate the temperature from the

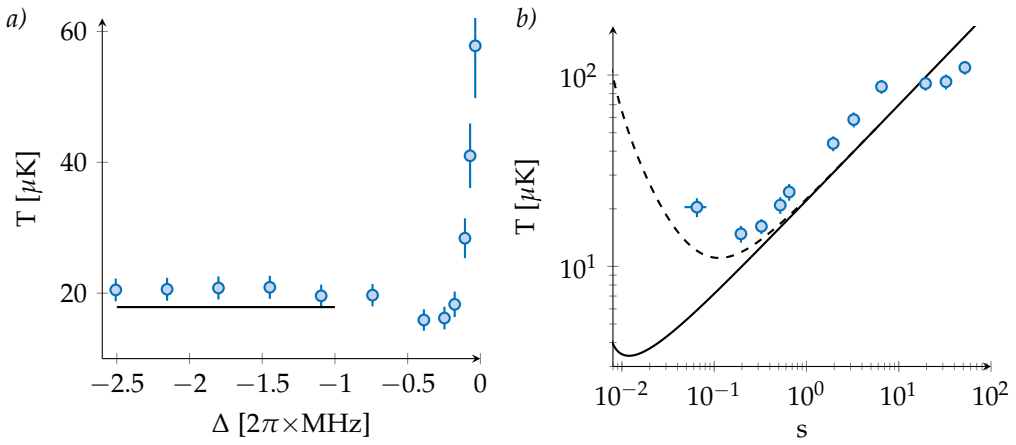

Figure 2.5 *– a) Variation of the temperature with the detuning for a fixed intensity $I/I_s = 0.65$. The solid line gives the expected value from the spin-polarized model. b) Variation of the temperature with the intensity for a fixed detuning $\Delta = 2\pi\times 1.8$ MHz. The solid line is obtained from the simple 2-level model, the dashed line curve takes into account heating due to experimental imperfections.*

competition between friction forces and heating caused by photon scattering. We neglect other mechanisms that can lead to an increase of the temperature. For example, we see that this latter increases linearly with the atomic peak density (density at the centre of the trap) (*cf.* Fig. (2.6)). This phenomenon was studied before [85, 86] and it was attributed to multiple scattering of photons within the cloud which heats the sample. The total temperature is then given by:

$$T(n_{\text{peak}}) = T_{\text{single atom}} + \gamma n_{\text{peak}} \tag{2.3}$$

Experimentally, we measure the temperature for different atomic densities for $s = 0.65$ and $\Delta = -2\pi \times 1.84$ MHz. The atomic density is changed by changing the magnetic field gradient. We obtain

$\gamma = 8(1) \times 10^{-11} \mu\text{K/cm}^3$.

The measured atom number, volume and peak density for different light intensities are reported in Fig. 2.7. We observe two different behaviours at low or large intensity. There is a quick increase of the loaded atom number at the beginning as the trap depth

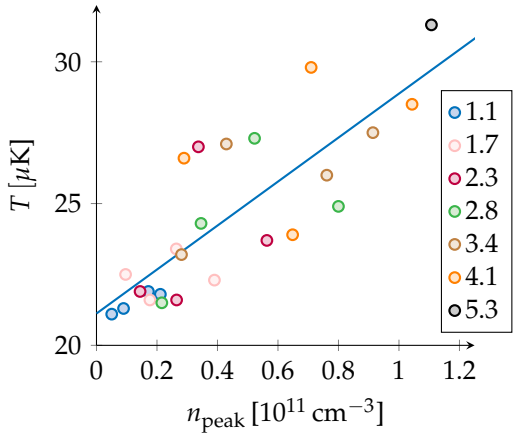

***Figure 2.6** – Variation of the temperature with the atomic peak density. Different colors correspond to different data sets taking for different values of the magnetic gradient. The values of the gradient in the legend are given in G/cm.*

increases. Then we observe a slow decay of the atom number in the MOT as the intensity continues to increase (for s > 5). We link this decay to 2-body atom losses (to be discussed in the following section). As for the volume, the quick increase at the beginning results from the temperature increase, since the MOT size is related to the temperature by:

$$\sigma_u = \sqrt{\frac{k_B T}{m\omega_u^2}} \tag{2.4}$$

with ω_u the angular trapping frequency along the direction $u = \{x, y, z\}$. For the high intensity regime, we observe a reduction of the MOT size that cannot be explained by eq. (2.4). A possible origin of this behaviour can be the multiple-scattering effect [87, 85, 86]. As the atomic density increases (Fig. 2.7.*c*), an absorbed photon can be emitted and then reabsorbed by a neighbouring atom. The multiplication of the absorption/emission cycles results in a repulsive interaction between atoms due to the radiation pressure force. Let us consider the simple case of a spherically symmetric harmonic trap (we neglect anisotropic geometry of the MOT, as well as the anisotropic light diffusion). The repulsion force between two atoms separated by a distance r reads

$$F = \Gamma \Pi_e \hbar k \frac{\sigma_{\text{abs}}}{4\pi r^2} \tag{2.5}$$

where we introduce the excited state population Π_e and the absorption cross section σ_{abs}. The balance between thermal effects and repulsion between atoms leads to an atomic

density:

$$n = \frac{2\pi}{2^{1/3}} s\eta \left(\frac{s\,(\eta - 2) - 1}{s\eta} \right)^{1/3} \frac{1}{\lambda^2 |z_c|^{2/3} z_{c,0}^{1/3}} \tag{2.6}$$

where z_c ($z_{c,0}$) is the vertical MOT position for a detuning $\Delta \neq 0$ ($\Delta = 0$). For a large saturation parameter s we expect to reach a constant value of the atomic density. The volume can then be obtained using $V = \frac{N}{n}$. The solid line curve in Fig. 2.7.*b* presents the expected value from this model. The agreement with the experimental measurement is relatively good.

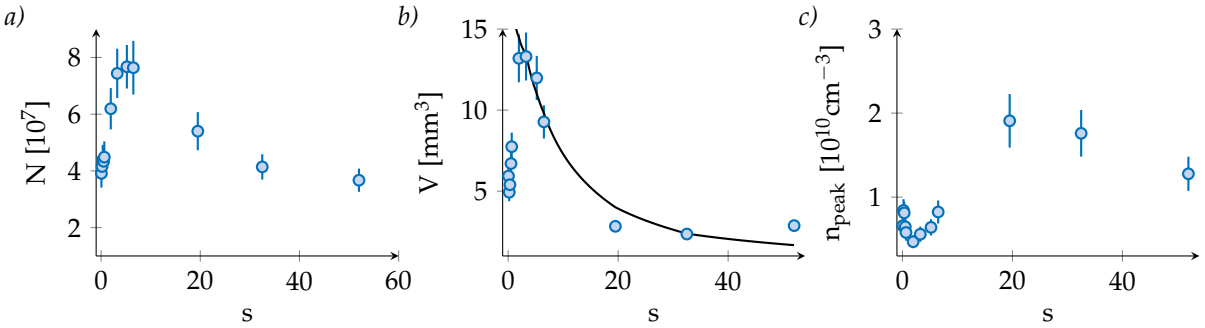

Figure 2.7 *– a)Loaded atom number in the MOT as function of the saturation parameter (for s ranging between 0.065 and 52). b)The variation of the MOT volume with the light intensity, the solid line is given by a constant density model (cf. text). c) The measured peak density as a function of the saturation parameter.*

2.2 Trap losses due to binary collisions

The development of optical cooling and trapping techniques revived the interest in the study of collisions in atomic gases. The lower temperature regime presents two main differences with respect to thermal collisions:

- a long de Broglie wavelength, typically hundred times the chemical bond.
- a long interaction time with respect to the spontaneous emission lifetime. Multiple photons can be exchanged during the collision.

The intensive studies of cold and ultracold collisions, starting from 1986 [88], were motivated by various questions, for example:

- how do collisions affect densities in atomic traps?
- how can the outcome channel of a collision be modified by an optical field?
- what is the quantum nature of the scattering process?

- Is it possible to reach quantum degeneracy with laser cooling techniques?

In this section, I will focus on light-assisted inelastic collisions in MOTs. I will start by giving an overview of the developed models and main experimental investigations of atomic trap loss due to binary collisions [71, 89]. Then, I will present our experimental study of two-body losses in a Dy MOT for different light parameters, and conclude with the MOT parameters leading to an optimal loading of the optical dipole trap.

2.2.1 Light-assisted collisions: models and limits

During an exothermic collision, the internal atomic energy (*e.g.* fine or hyperfine structure splitting energy) converts into kinetic energy shared by the atomic pair, which as a consequence heats the atomic sample. If the acquired energy is sufficiently high for the atoms to escape the trap, the collision results solely in atom losses. A simplified collisional scheme is presented in Fig. 2.8. Two atoms in the ground state interact through the attractive C_6/R^6 potential with R being the internuclear separation (shown as the $S+S$ potential in Fig. 2.8). In the presence of an optical field, one or both atoms of the pair can absorb a photon and get promoted to an excited state. In this case, the interaction is mediated by the resonant dipole-dipole force and the atomic pair approaches along attractive or repulsive C_3/R^3 potential depending on the light detuning with respect to the asymptotic resonance. The three possible excitation configurations are presented by the numbers 1, 2 and 3 in Fig. 2.8:

1. a resonant excitation with respect to the asymptotic resonance frequency ω_0, defined as $V_e(R) - V_g(R) = \hbar\omega_0$ in the asymptotic regime (*i.e.* for a large internuclear separation R) with V_e and V_g being the excited-state and ground-state potentials respectively.
2. If the laser field has a frequency ω_1 detuned to the blue with respect to the asymptotic resonance, then the repulsive C_3/R^3 potential will prevent the atomic pair from shrinking and thus 2-body collisions get prohibited. This mechanism is called *optical shielding* [90].
3. The third case corresponds to the situation where the laser field frequency is red detuned with respect to the asymptotic resonance. The absorption of a photon excites the atomic pair around the Condon point R_c and forms a quasimolecule. This process is called *photoassociation* [91, 92]. After the excitation, the quasimolecule vibrates within the potential and can be ionized in the presence of a second laser

field of a frequency ω_2 or decay to the ground state accompanied by the emission of a photon. The photoassociation technique is used to perform precision spectroscopy measurements that give an insight into the properties of the scattering process (molecular potentials, radiative lifetimes, *etc*) [93, 94].

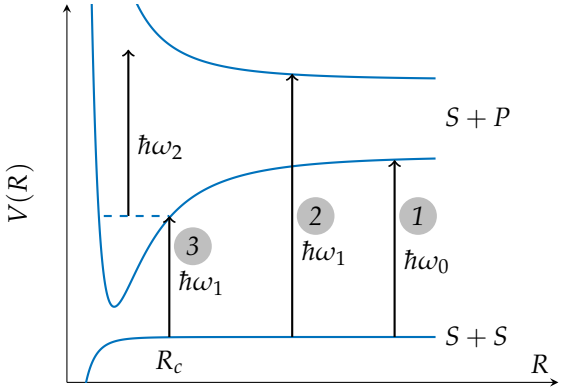

***Figure 2.8** – A simplified schematic of excited-state binary collisions: 1) laser field resonant with the excited molecular potential, 2) blue detuned laser field and 3) red detuned laser field.*

We now focus on the first case. It is possible to divide collisions in two categories:

- **ground-state collisions**: two atoms in the ground state interact through the $S + S$ potential for which the encounter pair could undergo an elastic collision (not exothermic) or a hyperfine-structure changing collision (HCC). The latter corresponds to the transition to a lower molecular hyperfine level during the collision and the released energy is equal to the Zeeman energy difference between the initial and final hyperfine levels. Since the released energy is relatively small (few GHz), the HCC mechanism dominates for low intensity optical fields as the trap becomes shallow and the needed energy for an atom to escape the trap decreases.
- **excited-state collisions**: atoms can absorb a MOT beam photon and this light-assisted collision occurs on an excited state. The two atoms approach each other along the attractive C_3/R^3 potential (here we consider only attractive potentials since repulsive potentials do not contribute to collisions that result in atom losses) and during this time, the pair can undergo a fine-structure changing collision (FCC) or a radiative escape (RE). The former mechanism is comparable to the HCC mechanism but taking place between two fine-structure levels. The latter mechanism describes a spontaneous emission occurring during the approach and the quasimolecule relaxes to the ground state. The gained kinetic energy can be

sufficient for the pair to escape the trap.

The Gallagher-Pritchard model

In 1989, Gallagher and Pritchard developped a semi-classical model [95] motivated by the experimental observation of trap atom losses due to exothermic collisions in a cold sample of Cs atoms [96]. They calculated the FCC and RE rates for a Na MOT and predict that the FCC is the dominant collisional mechanism. The scheme for the FCC

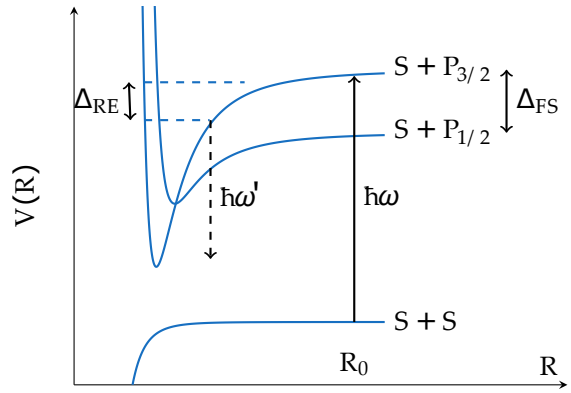

***Figure 2.9** – Schematic of the FCC and RE mechanisms for the Na example*

and RE mechanisms is shown in Fig. 2.9. The absorption of a photon at a frequency ω excites the population to the $S + P_{3/2}$ state (for the Na example). If the quasimolecule incurs a crossing to the $S + P_{1/2}$ potential, the collision leads to an energy transfer of $\Delta_{FS}/2$ for each atom (Δ_{FS} is the fine-structure splitting). If a spontaneous emission takes place before reaching the potentials crossing, then the energy transferred to each atom is $\frac{\hbar}{2}(\omega - \omega')$ with ω' being the frequency of the emitted photon.

The rate of exciting quasimolecules starting from two atoms at an internuclear separation R_0, in the presence of laser field of a frequency ω_L and an intensity I, is given by [71]:

$$\mathcal{R}\left(R_0, \omega_L, I\right) = \left[\frac{\left(\Gamma_M/2\right)^2}{\Delta_M^2 + \left(\Gamma_M/2\right)^2}\right] \frac{I}{\hbar\omega_L}\sigma \tag{2.7}$$

where $\Delta_M = \omega_L - \omega(R_0)$ is the laser detuning with respect to the resonance frequency taken at an internuclear separation R_0 (distance at which the excitation occurs). This latter is given by $\omega\left(R_0\right) = \omega_A - C_3/\hbar R_0^3$, with ω_A being the atomic resonant frequency. Γ_M is the molecular spontaneous decay rate and σ is the photoabsorption cross section taking into account all attractive molecular potentials.

After the excitation, the atoms start to accelerate toward each other until reaching a short range distance R. The acceleration time can be calculated as following:

$$t(R_0) = \sqrt{m/4} \int_0^{R_0} \mathrm{d}R \left[\frac{C_3}{R^3} - \frac{C_3}{R_0^3} \right] \tag{2.8}$$

this time can be also expressed as function of the detuning: $t(R_0) = \left(\frac{\Delta_\tau}{\Delta}\right)^{5/6} \Gamma_M^{-1}$, Δ_τ being the detuning at the reached distance R_τ.
If the atomic pair survives spontaneous emission, then the probability of undergoing a FCC is

$$P_{\mathrm{FCC}} = \frac{\eta\gamma}{1-\gamma^2+\eta\gamma^2} \tag{2.9}$$

where η is the FCC probability after a single passage through the crossing and $\gamma = e^{-\Gamma_M t(R_0)}$ is the survival probability against a spontaneous emission. Using eqs. (2.7), (2.8) and (2.9), one can calculate the FCC rate constant between an excited-state and a ground-state atoms:

$$\beta_{\mathrm{FCC}} = \frac{1}{4} \frac{\Delta_M^2 + \Gamma_A^2/4}{\Gamma_A/4} \frac{\hbar\omega_L}{I\sigma} \int_0^\infty \mathrm{d}R_0 4\pi R_0^2 \mathcal{R}\left(R_0, \omega_L, I\right) P_{\mathrm{FCC}}(R_0) \tag{2.10}$$

with Γ_A being the atomic spontaneous emission decay rate.
The RE rate constant can be calculated in the same fashion with replacing $P_{\mathrm{FCC}}(R_0)$ by $P_{\mathrm{RE}}(R_0)$. The probability that a spontaneous emission occurs at $R < R_E$ with R_E being the internuclear separation at which the gained kinetic energy is sufficient to escape the trap is given by:

$$P_{\mathrm{RE}}(R_0) = \frac{t_E(R_0)\Gamma_M\gamma}{1-\gamma^2+\eta\gamma^2} \tag{2.11}$$

where $t_E(R_0)$ is the time spent in the region $R < R_E$.

The Julienne-Vigué model

In 1991 Julienne and Vigué revisited the Gallagher-Pritchard model, taking into account the role of the angular momentum and thermal averaging [97]. In this updated

model, the rate of FCC and RE is written in the following form:

$$\beta = \frac{1}{2d_g^2}\frac{\pi v}{k^2}\sum_{l,\epsilon}(2l+1)P_{TL}(\epsilon,l)P_{ES}(R,\epsilon,l,\Delta,I) \tag{2.12}$$

d_g is the ground-state degeneracy, k is the wave vector of the reduced particle, v is the asymptotic velocity when the two atoms are far apart, P_{TL} is the probability that the loss mechanism supervenes after reaching an internuclear separation R_{TL}, P_{ES} is the excitation and survival probability and ϵ accounts for all attractive excited potentials that contribute to the collision.
Julienne and Vigué discussed also the nature of the collision interaction. They demonstrated that the FCC mechanism arises from spin-orbit (radial) coupling at short range and Coriolis (angular) coupling at long range. Thus spin-orbit coupling dominates for heavy atoms and Coriolis coupling dominates for light atoms with small spin-orbit terms.

To summarize, both Gallagher-Pritchard and Julienne-Vigué models predict FCC and RE rates in pretty good agreement with experimental results. Nevertheless they present some limitations, for example both semiclassical models assume that the decayed population after a first excitation does not contribute to the collision any more. This condition is valid for low intensity lasers, but for high intensity fields the decayed population can get re-exited which modifies significantly the probability of excitation at different internuclear separations along the collision path.

2.2.2 Experimental investigation of 2-body losses in a Dy MOT

The experimental investigation of the 2-body collisional losses can be done by measuring the MOT atom number's decay with time, governed by the following equation:

$$\dot{N}(t) = -\frac{N(t)}{\tau} - \beta\int_V n^2(r,t)\,d^3r \tag{2.13}$$

where one should integrate the spatial atomic density over the total volume V. τ is the one-body lifetime resulting from collisions with residual gas in the vacuum chamber. It is estimated to $\tau = 12(2)$ s.
In the low density regime, the density can be approximated by a gaussian profile, and

eq. (2.10) can be rewritten as:

$$\dot{N}(t) = -\frac{N(t)}{\tau} - \frac{\beta N^2(t)}{(2\pi)^{3/2} w_x w_y w_z} \tag{2.14}$$

with $w_{x,y,z}$ the $1/e$ MOT sizes. For high density regime, the atomic density becomes constant as the volume increases with the atom number [87]. In this case, eq.(2.10) has an analytical solution:

$$N(t) = \frac{N_0 e^{-t/\tau}}{1 + \frac{N_0 \tau \beta}{\overline{V}} (1 - e^{-t/\tau})} \tag{2.15}$$

with $\overline{V} = (2\pi)^{3/2} w_x w_y w_z$.

Experimental sequence and fitting procedure

We prepare the MOT as described in the previous section, then we hold it for variable time durations and we record the atom number and the trap sizes. In the following, the given values of the laser detuning or intensity are those reached at the end of the compression phase. We performed two sets of experiments to measure: the variation of β as a function of the detuning for a fixed $s = 0.65$, and as a function of the intensity for a fixed detuning $\Delta \sim -2\pi \times 4.4$ MHz. Fig. 2.10 shows an example of two decay curves measured for different detunings $\Delta/2\pi = -0.7$ and -2.17 MHz (circles and triangles respectively). The fitting procedure of the data is slightly tricky as none of the previously

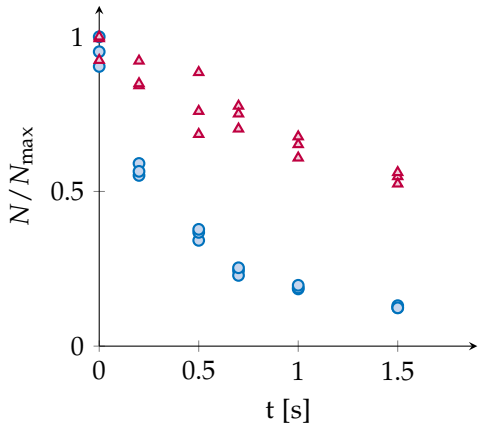

Figure 2.10 *– Decay curves for $\Delta = -2\pi \times 0.7$ MHz (circles) and $\Delta = -2\pi \times 2.17$ MHz (triangles).*

announced cases (constant volume or constant density) is observed experimentally. Both the atomic density and the MOT volume changes with time and atom number as shown

in Fig. 2.11. We start by fitting the growth of the volume with atom number (we observe

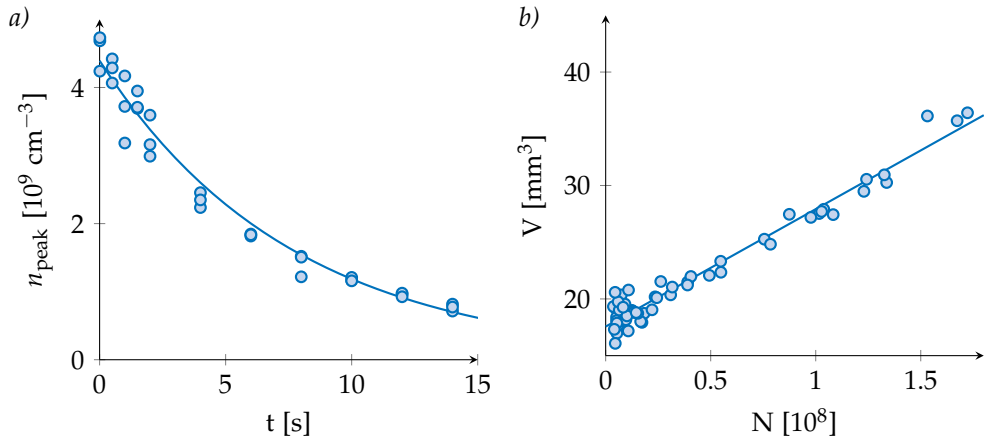

Figure 2.11 *– a) Variation of the atomic peak density with time during an atom number decay sequence. The exponential fit gives an initial peak density $n_0 = 4.4 \times 10^9$ cm^{-3} and a decay time $\tau = 7.6$ s. b) Variation of the MOT volume with atom number. The fitted slope is $\alpha = 10.3$ $mm^3/10^8 at$.*

a linear dependency) then we include this result in the differential equation (2.14) that we solve numerically. We fit the data (atom number decay over time) with the obtained solution with three free parameters: the initial atom number N_0, the one-body lifetime τ and the two-body loss constant β. The binary collisional loss process dominates at short times as the density is high while background collisions (one-body loss mechanism) account for the observation at longer times. We use *bootstrap* fitting technique [a] to have a robust estimation of the fitting parameters and the corresponding error bars. Results are presented in Fig. 2.12.

Interpretation of experimental results

The fitted value of the 2-body loss constant β accounts for all collisional loss processes and it is difficult to attribute the losses to a specific process without further experimental investigation.

We developed a simple model inspired from the above exposed models. Details of this model can be found in refs. [82, 83]. As a first approximation, we consider only one effective excited potential described by $V_{\text{mol}} = \frac{-\lambda\hbar\Gamma}{(kr)^3}$, with a $1/e$ molecular lifetime $(\mu\Gamma)^{-1}$, where Γ is the excited state natural linewidth (Γ_{Red} in our case) and k is the light wave-vector. λ and μ are dimensionless parameters that characterize the molecular

[a] It is a fit procedure that relies on random sampling with replacement. It is convenient since it does not require any knowledge of the statistic distribution of the fitted parameter.

potential. With this simple model, β can be extracted by:

$$\beta = \int \mathrm{d}r \Gamma_{\mathrm{ass}}(r) P_{\mathrm{loss}}(r) \tag{2.16}$$

where the quasi-molecule association rate Γ_{ass} and the loss probability P_{loss} are given by:

$$\Gamma_{\mathrm{ass}}(r) = \frac{\mu\Gamma}{2} \frac{2s}{1 + 4\left[\Delta_{\mathrm{loc}} - V_{\mathrm{mol}}(r)/\hbar\right]^2 / (\mu\Gamma)^2} \tag{2.17}$$

$$P_{\mathrm{loss}}(r) = \exp\left[\frac{-\mu}{2\sqrt{\lambda}}(kr)^{5/2}\sqrt{\frac{\hbar\Gamma}{2E_{\mathrm{r}}}} f\left[\left(1 + \frac{E^\star}{|V_{\mathrm{mol}}(r)|}\right)^{-1/3}\right]\right] \tag{2.18}$$

with E_{r} being the recoil energy, $f(x) = \int_x^1 \frac{\mathrm{d}u}{\sqrt{u^{-3}-1}}$ and $E^\star$ is the cutoff energy above which a particle leaves the trap.

In the spin-polarized regime, the collisional loss constant β has an analytic expression:

$$\beta_{\mathrm{pol}} = \frac{2\pi^2\lambda^2\mu}{3}\left(\frac{\Gamma}{\Delta_{\mathrm{loc}}}\right)^2 \frac{s\Gamma}{k^3} \exp\left[-0.264\lambda^{1/3}\mu|\frac{\Gamma}{\Delta_{\mathrm{loc}}}|^{5/6}\sqrt{\frac{\hbar\Gamma}{E_{\mathrm{r}}}}\right]. \tag{2.19}$$

The obtained values from eq. (2.19) are presented with the dashed lines in Fig. 2.12. The solid line in Fig. 2.12.*a* is the fit result with λ and μ as free parameters. We get $\lambda = 0.75$ and $\mu = 0.5$. For the variation of β with the laser intensity, the agreement with the model is good for large values of the saturation parameter (plotted for $\lambda = 0.68$ and $\mu = 1.05$). The values of λ and μ can be compared to those obtained by averaging over all excited states. The large spin of Dy results in a complex net of molecular potentials ($(2(2J+1)(2J'+1) = 646$ molecular potentials). When averaging over 323 attractive molecular curves one gets $\bar{\lambda} = 0.68$ and $\bar{\mu} = 1.05$.

To conclude, we measure $\beta_{\mathrm{min}} \simeq 2.3(5) \times 10^{-11}\mathrm{cm}^3/\mathrm{s}$ in the spin-polarized regime, for a saturation parameter $s = 0.65$, which is the optimal starting point for loading the optical dipole trap.

In the presented above model, we consider only RE mechanism. The FCC mechanism can be mapped to the case of Dy by replacing the fine-structure levels with levels resulting from the $j - j$ coupling between electrons from the inner 4f shell and 6s outer shells. The difficulty remains in the determination of the excited states participating to the collision, due to the complexity of Dy's electronic structure.

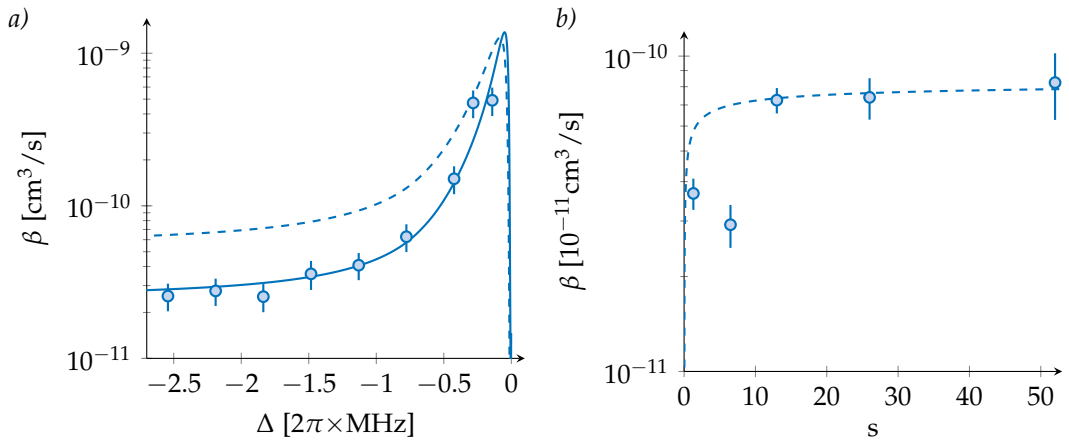

Figure 2.12 *– a) Variation of the 2-body loss constant with the detuning for s = 0.65. The solid line is a fit result with $\lambda = 0.75$ and $\mu = 0.5$. The dashed line is obtained for $\lambda = \bar{\lambda}$ and $\mu = \bar{\mu}$. b) Variation of the 2-body loss constant with the saturation parameter for $\Delta \simeq -2\pi\times 4.4$ MHz. The dashed line is obtained for $\lambda = \bar{\lambda}$ and $\mu = \bar{\mu}$.*

2.3 Optical dipole trap

The idea of trapping and storing neutral atoms using a laser field was firstly suggested by Letkhov in 1978 [98]. The first experimental demonstration of such a trap was done by Chu et *al.* in 1986 [99] and it is considered as a breaking through result in the field of cold atoms as it opened the door to different implementations: evaporative cooling, optical tweezers for single atoms, optical lattices, *etc*. Here, I will recall the principal of an optical dipole trap (ODT) and give the important parameters to characterize it. A more detailed description can be found in ref. [100].

Let's consider an atom in the presence of an external electric field $\vec{E}\,(r,t) = \hat{e}E(r)e^{-i\omega t} + c.c$ where $\hat{e}$ is the polarization unit vector, $E(r)$ is the electric field amplitude at a position r and ω is the field frequency. The atom can be considered as an oscillator with an induced dipole moment $\vec{p} = \alpha(\omega)\vec{E}$. We introduce here the complex polarizability α that is a function of the frequency ω. The resulting interaction potential can be written as

$$U_{\text{dip}} = -\frac{1}{2}\langle \vec{p}\cdot\vec{E}\rangle = -\frac{1}{2\epsilon_0 c}\Re[\alpha]I(r) \tag{2.20}$$

the brakets $\langle\cdot\rangle$ correspond to time average and $I(r) = 2\epsilon_0 c|E(r)|^2$ to the laser intensity. The force felt by the atoms in the presence of the laser field is given by $\vec{F}_{\text{dip}} = -\vec{\nabla}U_{\text{dip}}(r)$. We can calculate also the scattering rate by considering the atom as an oscillator that undergoes absorption/emission cycles. The power absorbed by the atom and the scattering

rate are

$$P_{\text{abs}} = \langle \dot{\vec{p}}\vec{E} \rangle = 2\omega \Im[pE^*] = \frac{\omega}{\epsilon_0 c} \Im[\alpha] I(r) \tag{2.21}$$

$$\Gamma_{\text{sc}} = \frac{P_{\text{abs}}}{\hbar\omega} = \frac{1}{\hbar\epsilon_0 c} \Im[\alpha] I(r) \tag{2.22}$$

The presence of an external electric field shifts the energy levels of an atom. The interaction hamiltonian is $H_{\text{int}} = -\hat{\mu}E$ with $\hat{\mu} = -e\hat{r}$ being the electric dipole operator. The energy shift can be calculated using a second order time dependent perturbation theory for non-degenerate levels. In the simple case of a 2-level atom:

$$\Delta E = \pm \frac{|\langle e|\mu|g\rangle|^2}{\Delta_{eg}} |E|^2 = \pm \frac{3\pi c^2}{2\omega_0^3} \Gamma I(r) \left(\frac{1}{\omega - \omega_0} + \frac{1}{\omega + \omega_0} \right) \simeq \pm \frac{3\pi c^2}{2\omega_0^3} \frac{\Gamma}{\Delta} I(r) \tag{2.23}$$

the $\pm$ sign accounts for the shift of the ground and excited states respectively, Γ is the linewidth of the excited state and Δ is the laser detuning with respect to the atomic resonance. According to eq. (2.23), a *red-detuned* laser beam (*i.e.* $\Delta < 0$) will result in shifting the ground state level downward thus atoms get attracted to high intensity regions. In the same way atoms get repelled from high intensity regions for a *blue-detuned* laser field ($\Delta > 0$). In the general case of a multi-level atom, one needs to know all dipole matrix elements $\mu_{ij} = \langle j|\mu|i\rangle$ (*cf.* next chapter). The calculation of the μ_{ij} coefficients for Dy is challenging due to the complexity of the electronic spectrum. Few theoretical works exist with this regard [101, 69]. Experimentally, we use gaussian laser beams with an intensity profile:

$$I(r,z) = \frac{2P}{\pi w^2(z)} \exp\left(\frac{-2r^2}{w^2(z)} \right) \tag{2.24}$$

where z is the propagation direction, P is the power of the laser beam and $w(z) = w_0 \sqrt{1 + \left(\frac{z}{z_R}\right)^2}$ is the $1/e^2$ radius where w_0 denotes the beam waist and $z_R = \frac{\pi w_0^2}{\lambda}$ is the Rayleigh length. Combining eqs. (2.20) and (2.24) one can approximate the dipolar potential with a harmonic potential around $z = 0$ and $r = 0$:

$$U_{\text{dip}} \simeq -U_0 \left[1 - 2\left(\frac{r}{w_0}\right)^2 - \left(\frac{z}{z_R}\right)^2 \right] \tag{2.25}$$

we define the radial and axial frequencies as:

$$\omega_r = \sqrt{\frac{4U_0}{mw_0^2}} \tag{2.26}$$

$$\omega_z = \sqrt{\frac{2U_0}{mz_R^2}} \tag{2.27}$$

where $U_0 = \frac{P\Re[\alpha]}{\epsilon_0 c \pi w_0^2}$. Hence a good characterization of the trap depth requires a good knowledge of the atomic polarizability. Recent measurements by the group of R. Grimm of the Dy dynamical polarizability at $\lambda = 1064$ nm determined the values of scalar and tensor polarizabilities $\alpha_s = 184.4\ (2.4)$ a.u. and $\alpha_t = 1.7\ (6)$ a.u. [102]. They measured collective oscillations in the optical trap and then used Potassium atoms, trapped by the same beam, as a reference. This technique enhanced the accuracy with which the atomic polarizability is determined. The announced values are larger than the measured ones by both Lev and Pfau groups and in a good agreement with the reported numerical studies [69].

2.3.1 Experimental setup

At the end of the MOT compression phase we shine on a 50 W laser beam[a] working at $\lambda = 1070$ nm and focused at the MOT position. We use this trap to transport atoms from the MOT chamber to the science cell. The transport is done by moving the focal point position thanks to a motorized translation stage[b]. The optical scheme is shown in Fig. 2.13.

We measure the size of the beam at different positions and extract $w_{x0} = 34.5(2)\ \mu$m and $w_{y0} = 34.2(7)\ \mu$m for the horizontal and vertical directions respectively. The fitted M^2 is on the order of 1.1 for both directions. We observe a slight astigmatism $\simeq 0.5$ mm, which is smaller than the Rayleigh length $z_R = 3.5$ mm. The presence of astigmatism reduces the axial confinement which is a crucial aspect for this beam as we use it to transport atoms from the MOT chamber to the glass cell. To estimate the quality of our beam, we compute a power series expansion around $z = 0$ to get the curvature of the $\frac{1}{w_x(z)w_y(z)}$ curve that is proportional to the intensity. For a gaussian beam the quadratic term is

[a] IPG Ytterbium Fiber Laser Model YLR-50-LP-Y12
[b] Aerotech ANT130-160-L

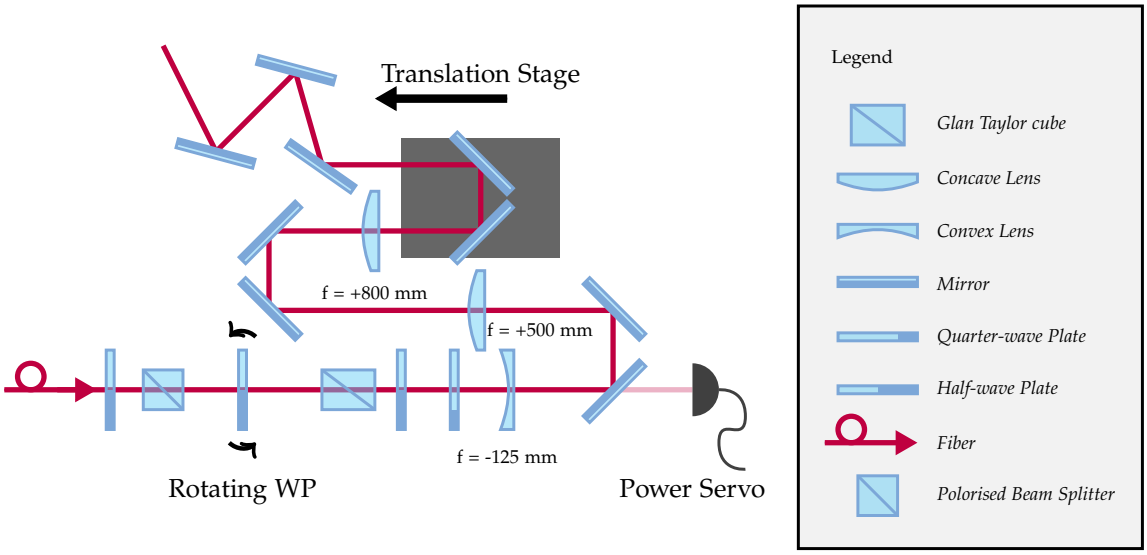

***Figure 2.13** – Optical scheme of the transport trap*

proportional to $\frac{\lambda^2}{\pi^2 w_0^6}$, as a consequence one gets $\omega_z \propto \sqrt{\text{curvature}}$. We obtain

$$\sqrt{\frac{\text{curv}_{\text{exp}}}{\text{curv}_{\text{ideal trap}}}} = 0.85$$

consistent with the measured astigmatism.

2.3.2 Measurement of oscillation frequencies

Axial dipole mode

The axial trapping frequency is recorded through the center of mass oscillation after applying a sudden position shift δ of the potential along the axial direction z. Let us consider the 1D-motion of a single atom along z in a finite depth trap, the oscillation frequency can be expressed as:

$$\omega = \omega_z f\left(z_{\text{max}}/z_R\right) \tag{2.28}$$

$$f(x) = \frac{\pi}{2} \Bigg/ \int_0^x \mathrm{d}u \left(\frac{1}{1+u^2} - \frac{1}{1+x^2}\right)^{-1/2} \tag{2.29}$$

with ω_z defined in eq. (2.27) and z_{max} is the maximum value of z reached during the oscillation. Two main points have to be noted:

- the finite excitation amplitude leads to a frequency downshift. For a zero-temperature cloud in a real trap, the oscillation would be dampless, of frequency $\omega(\delta/z_R)$. One

should keep in mind that the center of mass oscillation amplitude is constant in an ideal harmonic trap even for $T > 0$, the damping we are considering here is due to anharmonicities).

- For a finite-temperature cloud, the thermal energy distribution leads to a distribution of oscillation frequencies, leading to damped oscillations, with a mean oscillation frequency Ω lower than ω_z.

In the limit of a small excitation amplitude δ, the center of mass oscillation can be approximated by:

$$z(t) = \delta \int \mathrm{d}\epsilon \rho(\epsilon) e^{-\epsilon/(k_B T)} \cos\left[\omega(z_{\max}(\epsilon))\right] \Big/ \int \mathrm{d}\epsilon \rho(\epsilon) e^{-\epsilon/(k_B T)} \tag{2.30}$$

$$\simeq A \cos\left[\Omega t + \phi\right] e^{-t/\tau} \tag{2.31}$$

$\rho(\epsilon)$ is the density of state for a 1D dipole trap. The frequency Ω and damping time τ depend on the truncation parameter $\eta = U_0/(k_B T)$.

So far we assumed that the atom was located on the z axis. However, at finite temperature we expect a thermal excitation of the radial motion. This leads to an effective reduction of the axial potential energy, given by the thermal average over the radial coordinate:

$$U_{\mathrm{eff}}(z) = \langle U_{\mathrm{dip}}(r, z) \rangle_r \tag{2.32}$$

Expected corrections to the oscillation frequency as a function of the finite excitation amplitude the temperature are shown in Fig. 2.14. Experimentally, we fit the sloshing

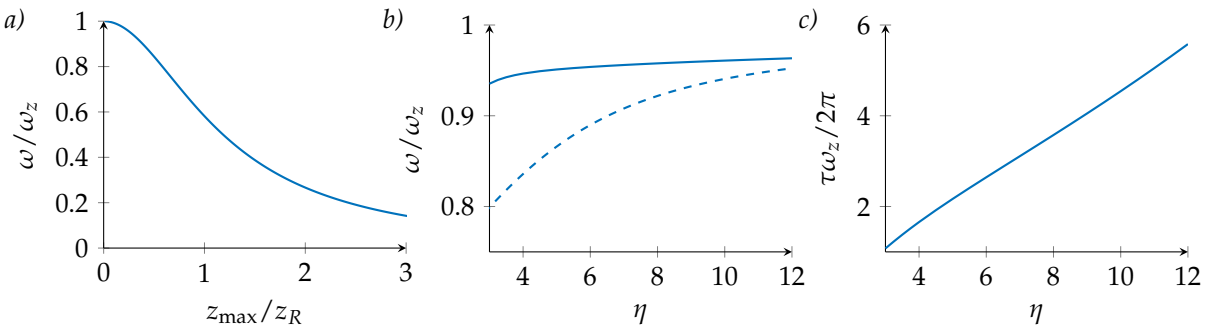

Figure 2.14 *– a) Variation of the axial trapping frequency with the oscillation amplitude. b) Variation of the axial trapping frequency with the η: for a 1D system (solid line) and when taking into account radial effects (dashed line). c) Oscillation damping time τ as a function of η.*

motion of the atomic cloud's centre of mass (*cf.* Fig. 2.15) and extract the values of axial

frequency $\omega = 2\pi \times 10.7(3)$ Hz and $\tau = 0.24(0.02)$ s, that corresponds to a truncation parameter $\eta \simeq 7$.

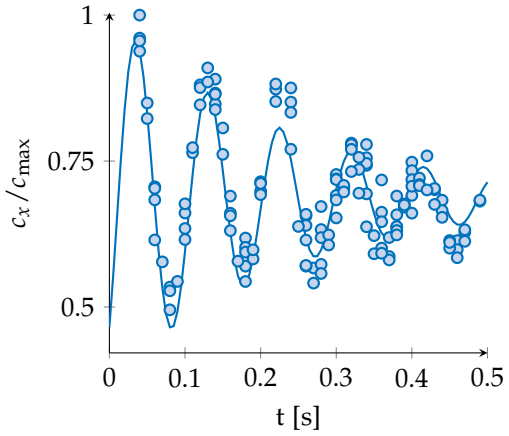

Figure 2.15 *– Center of mass oscillation along the axial direction. The fit function (solid line) is given by eq.* (2.31).

Transverse radial mode

The previous analysis of large amplitude motion can be transposed to the radial direction using:

$$\omega = \omega_r g(r_{\max}/w_0) \tag{2.33}$$

$$g(x) = \frac{\pi}{\sqrt{8}} \Big/ \int_0^x \mathrm{d}u \left(e^{-2u^2} - e^{-2x^2}\right)^{-1/2} \tag{2.34}$$

For the radial direction, the confinement is much higher thus the radial motion is very small and it is difficult to measure with our imaging system. Instead we measure the trapping frequency by exciting the breathing mode. This is done by ramping down the laser power adiabatically then ramp it up to its maximal value suddenly. The description made above can be transposed to the radial breathing mode in the collisionless regime, with an expected breathing frequency of $2\omega_r$ in the harmonic regime. The frequency gets reduced in the presence of collisions [103].

Experimentally, we measure $\omega_r = 2\pi \times 1.83(4)$ kHz and $\tau = 2.6(2)$ ms.

The scalar part of the dynamical polarizability can be deduced from the trapping frequencies values:

$$\alpha_s = \frac{\omega_r^2 m \pi w_0^2 \epsilon_0 c}{4P} \tag{2.35}$$

$$= \frac{\omega_z^2 m \pi z_R^2 w_0^2 \epsilon_0 c}{2P} \tag{2.36}$$

From the previous discussion, we see that we cannot determine α_s with an accuracy higher than 20% due to the uncertainty on the value of the frequencies. It is mostly the thermal effects that limit the precision of the measurement. In ref. [102], the authors measured the trapping frequencies for different temperatures and they extrapolate to the zero-temperature regime. Using $\alpha_s = 184$ a.u. and a power $P = 40$ W we get a trap depth $U_0 \simeq 1$ mK.

2.3.3 Loading the ODT

The starting point for loading the ODT is the spin-polarized regime for the MOT in order to minimize binary collisional losses. Then we play with the loading duration, the MOT position with respect to the focal point of the laser beam and the MOT density to optimize the loading efficiency. For example, we see that the loading is more efficient when we are out of focus as the effective volume of the trap is larger. Fig. 2.16.*a* shows the atom number loaded in the ODT as function of the MOT loading duration. The exponential fit gives a characteristic time $\tau = 4.13$ s.

The density of the MOT plays also an important role during the loading of the trap. For a fixed intensity $I/I_s = 0.13$ and gradient $\nabla B = 1.71$ G/cm, we compare the efficiency of the loading at three different detunings $\Delta = -2\pi \times \{1.1, 1.8, 2.2\}$ MHz (always in the spin polarized regime). Results are plotted in Fig. 2.16.*b*. We measure the loaded atom number in the trap while holding the MOT and the laser beam on for various durations. We clearly see that the efficiency decreases for the large value of the detuning $\Delta = -2\pi \times 2.2$ MHz (triangles) as the MOT volume increases and hence the density gets lower.

After all optimizations, we get an overall loading efficiency ≥ 10 % with $N_{\text{dip}} \simeq 1.5 \times 10^7$.

2.4 Optical transport of a thermal cloud

Cold atom experiments get to be more and more complex with multiple stages. Different lasers and magnetic fields are necessary to control the atomic state. Hence a good flexibility of the experimental apparatus is needed. In order to have more optical access, we perform optical transport from the MOT chamber to the glass cell.

In the first part of this section, I will expose the simple case of a harmonic trap and

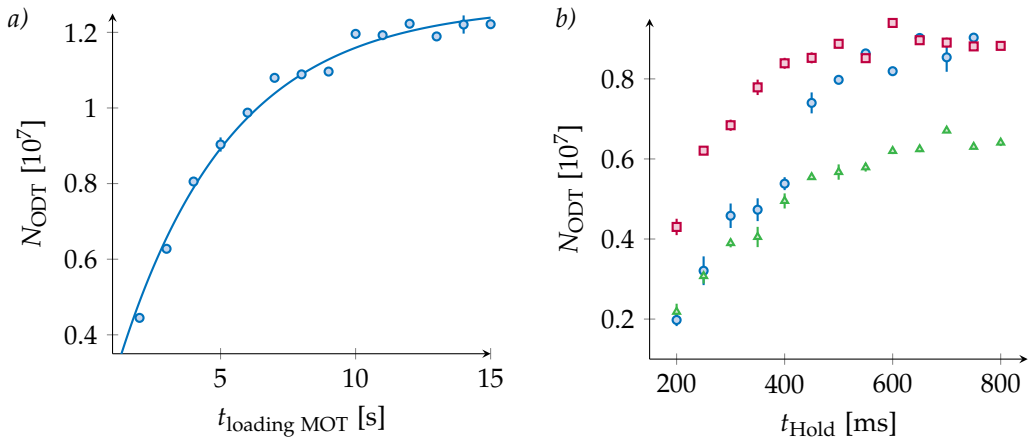

***Figure 2.16** – a) Atom number loaded in the ODT as function of the MOT loading duration. b) Atom number loaded in the ODT as function of the holding time of the MOT and trap together for $\Delta = -2\pi\times1.1$ MHz (circle), $\Delta = -2\pi\times1.8$ MHz (square) and $\Delta = -2\pi\times2.2$ MHz (triangle).*

show that there are optimal transport times for which the excitation induced during the movement is reduced. Then, I will consider the case of a real trap. Finally, I will compare experimental results to simulations and discuss optimal transport parameters.

2.4.1 Harmonic case

The transport problem can be treated classically. We consider only the motion of the atoms along the axial direction as the radial confinement is ~ 100 times larger than the axial one, thus the excitation of the motion can be neglected along the radial direction over the transport duration. As a first approximation, we consider the trapping potential to be harmonic with an axial trapping frequency ω_z. We note $z_0(t)$ the center position of the trap at a time t. In the moving frame attached to the trap, the potential acceleration can be considered as an extra force described by $-m\ddot{z}_0(t)$. One can get the cloud's center of mass position by applying Newton's law:

$$z(t) = z_0(t) + \int_0^t dt' \sin\left[\omega_z\left(t'-t\right)\right]\ddot{z}_0\left(t'\right) \tag{2.37}$$

We set the boundary conditions to be: $z(0) = \dot{z}(0) = 0$. For a finite transport time T, the center of mass position is given by:

$$z(t > T) = \frac{|F[\ddot{z}_0](\omega_z)|}{\omega_z}\sin(\omega_z t + \phi) \tag{2.38}$$

with $F\left[\ddot{z}_0\right](\omega_z)$ the Fourier transform of $\ddot{z}$ defined as:

$$F\left[\ddot{z}_0\right](\omega_z) = \int_{-\infty}^{+\infty} \ddot{z}_0(t)\, e^{-i\omega_z t} dt \tag{2.39}$$

Using the relation: $F\left[f^{(n)}(t)\right](\omega_z) = (i\omega_z)^n F\left[f(t)\right](\omega_z)$, we can rewrite eq.(2.38) as:

$$z(t > T) = \left|F\left[\dot{z}_0\right](\omega_z)\right| \sin(\omega_z t + \phi) \tag{2.40}$$

At the end of the transport, the cloud center of mass oscillates at the trap frequency ω_z and with an amplitude given by the Fourier transform of the velocity profile applied to the trap. These oscillations can be translated into heating (or atom losses for finite trap depth). One can reduce this effect by choosing wisely the velocity profile of the trap displacement.

An example of the acceleration and velocity profiles used in our experiment is presented in Fig.2.17 (*cf.* Appendix A for more details on the used velocity profiles). For this example, the Fourier transform of the velocity profile can be calculated analytically and we get that the center of mass oscillation amplitude $\mathcal{A} \propto \text{sinc}\left(\frac{\omega_z T}{4}\right)$. We define $T_0 = \frac{2\pi}{\omega_z}$, the trap oscillation period. Then we see that $\mathcal{A}$ vanishes for transport duration $T = 2nT_0$, with $n \in \mathbb{N}$. In principle, one can transport an atomic cloud in a non-adiabatic manner without introducing any heating. This technique is widely studied in literature and known as the *Shortcut to Adiabaticity* [104].

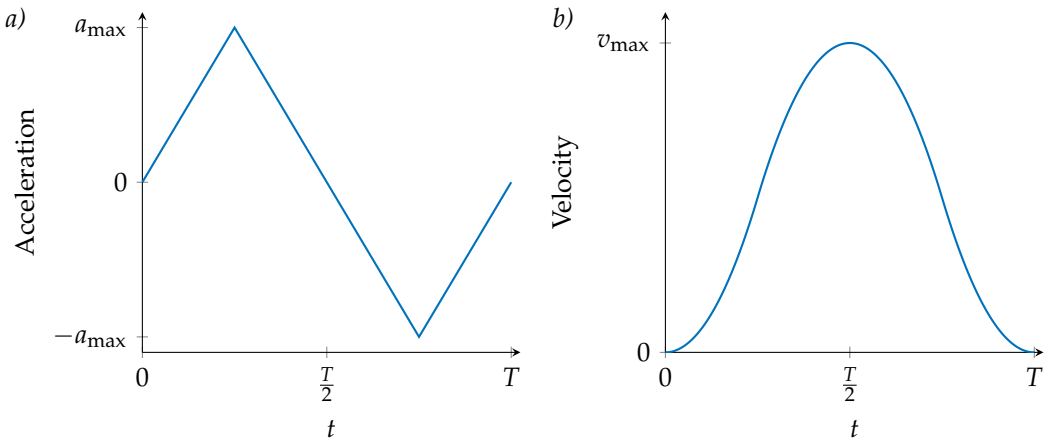

Figure 2.17 *– Example of acceleration and velocity profiles applied to the translation stage*

2.4.2 The real trap

Experimentally, two points need to be taken into consideration in order to optimize the transport. First, real traps have a finite depth and for large oscillation amplitudes, anharmonicity starts to play a role. Secondly, the finite lifetime in the dipole trap sets an upper bound on the transport duration. In Fig.2.18.*a*, is presented the measured oscillation amplitude of the center of mass as function of the transport duration. The calculated amplitudes for the used acceleration profiles, following the simple model presented in the previous paragraph, are also plotted (square). We see that for $T > 1.1$ s we have a good agreement between our experimental results and the expected values. For shorter times, the observed deviation can be due to anharmonicities. As one can see in Fig.2.18.*c* the center of mass oscillation is quickly damped, thus the harmonic trap approximation fails. We observe effects of shortcut to adiabaticity at $T \simeq 0.9$ s and $T \simeq 1.2$ s for which we see local minima of the oscillation amplitude $\mathcal{A}$. Fig. 2.19.*a* shows the measured atom number after transport as a function of the duration of the latter. For large T, the observed atom loss can be explained by the finite lifetime in the dipole trap. For short T, the dipole trap potential becomes tilted due to acceleration. In the moving frame, the expression of the trapping potential is given by:

$$U(r,z) = -\frac{U_0}{1+\frac{z^2}{z_R^2}} e^{-2r^2/w^2(z)} + maz \tag{2.41}$$

with a being the acceleration profile applied to the trap. For maz_R on the order of U_0, the trap becomes highly asymmetric and its effective depth gets reduced. In this case, atom loss is caused by spilling (*cf.* Fig. 2.19). We set the time duration of the transport to $T = 1.173$ s (duration that corresponds to the minimization of the sloshing at the end of the transport).

We perform two sets of measurements to estimate the overall efficiency of the transport and the lifetime in the ODT along the path from the MOT chamber to the glass cell. We do round-trips between the MOT position and different positions along the transport path with a variable waiting time either at the reached position z or at MOT position (Fig. 2.20) such that the total duration of each measurement is equal to $2T = 2.346$ s. Firstly we notice that we have large losses around $z = 80$ mm from the MOT position, which corresponds to the position of an ion pump. The magnetic field created by this pump can be responsible for the observed losses, either by deforming the trap or by causing losses

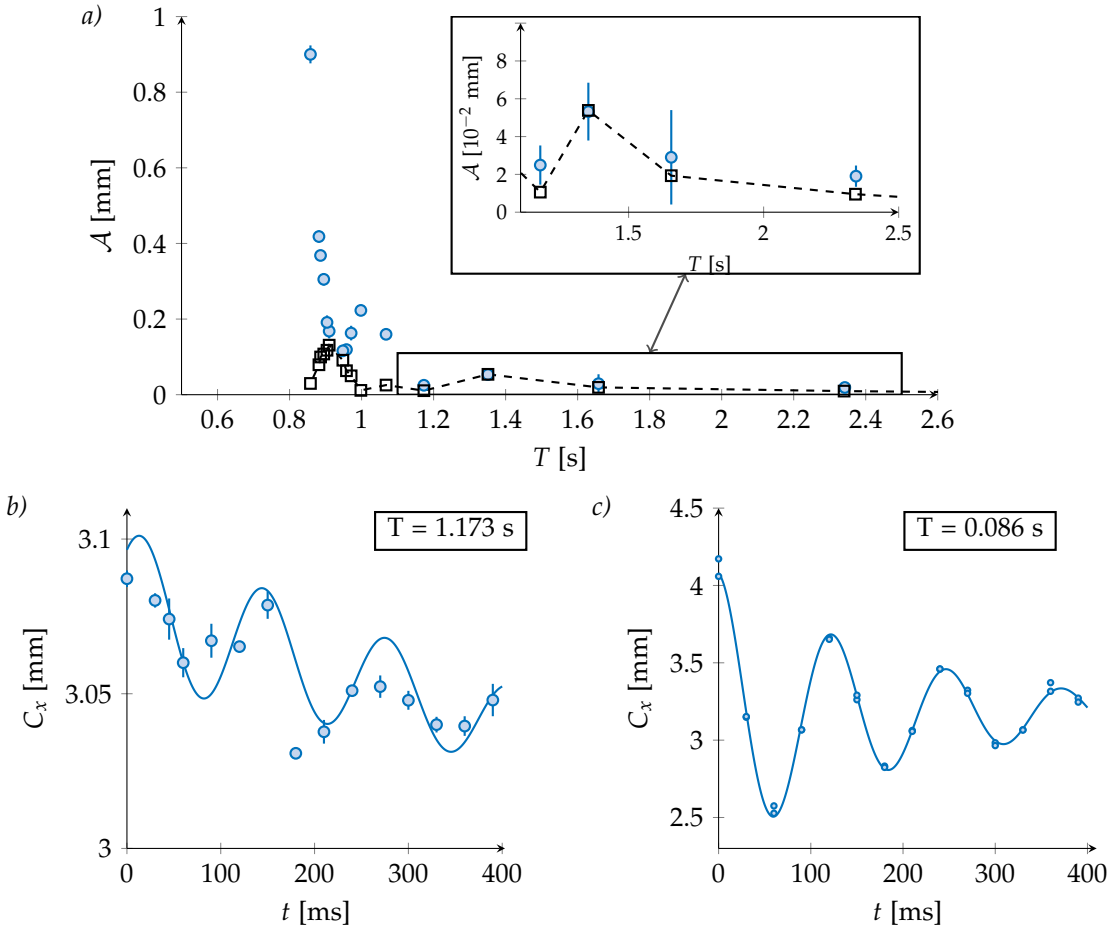

***Figure 2.18** – a) Oscillation amplitude at the end of the transport as function of the transport duration. The expected values from the harmonic model calculated for the experimentally applied velocity profiles are presented in black squares (the dashed line is drawn to guide the eye). b,c) Examples of centre of mass oscillation at the end of transport for long and short transport duration.*

through dipolar relaxation (to be studied in the next chapter). We use coils set around the optical table to compensate for this field. Secondly, taking into account that the lifetime in the glass cell is approximatively twice larger than the one in the MOT chamber (*cf.* Fig. 2.19.*b*), we can set a lower limit to the mechanical efficiency of the transport. We compare the remaining atom number in the trap after a wait time $t_{\text{wait}} = 2.346$ s in the MOT chamber (time needed to do a round trip between the MOT chamber and the glass cell) to the one obtained after a round trip to the glass cell multiplied by $e^{\tau_{\text{MOT}}}/e^{\tau_{\text{cell}}}$, with $\tau_{\text{MOT}} = 4.7(7)$ s and $\tau_{\text{cell}} = 9.7(4)$ s the lifetimes in the MOT chamber and glass cell, respectively. We measure an efficiency of 94%. In the glass cell, we have $N_{\text{dip}} \simeq 1 \times 10^7$.

To conclude, we were able to transport atoms from the MOT chamber to the glass cell using a shortcut to adiabaticity technique that minimizes the induced heating during

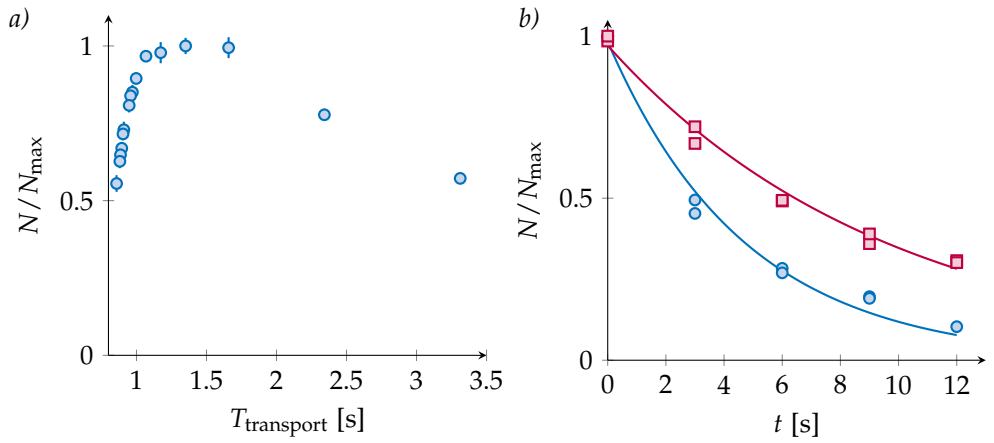

Figure 2.19 – *a) Atom number after transport (normalized to the maximum value) as a function of the transport duration. b) Measured decay curves in the MOT chamber (circle) and in the glass cell (square). The fitted lifetime durations are* $\tau_{MOT} = 4.7(7)$ *s and* $\tau_{Cell} = 9.7(4)$ *s.*

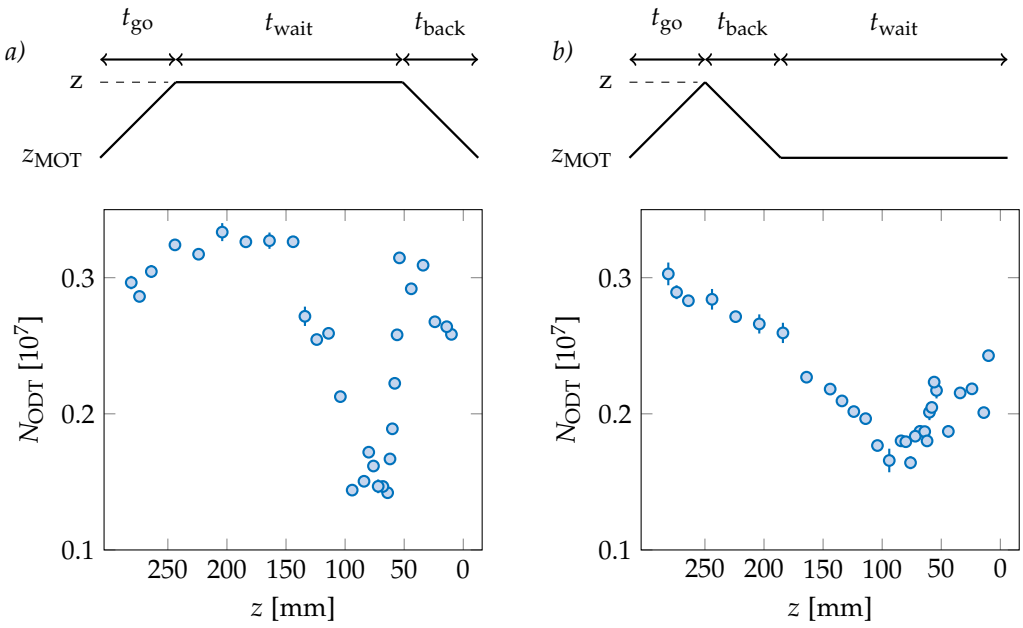

Figure 2.20 – *Atom number in the ODT after a round trip starting from the MOT position (*$z = 0$*).* $z \simeq 280$ *mm is the glass cell central position. The total round trip duration is fixed to* $T = 2.346$ *s. a) The holding takes place at the reached position. b) The holding takes place at the MOT position after the round-trip.*

the movement. At the end of the transport, the centre of mass oscillation amplitude is ~ 30 μm *i.e.* ~ 100 times smaller than the Rayleigh length z_R. The oscillation amplitude is also small with respect to the cloud size along the axial direction which is 1.3 mm. We have $\sim 1 \times 10^7$ atoms in the ODT which is a good starting condition for loading the cross-dipole trap and proceed with the evaporation cooling to reach quantum degeneracy.

Chapter 3

Atom-Light interaction: trapping vs heating

The atom light interaction is an essential ingredient in cold atoms experiments. From trapping to atomic state manipulation with light, examples are numerous. In the first part of this chapter, I will introduce the peculiarity of Dy when interacting with an external AC electric field. Due to its large spin ($J = 8$ in ground state), vectorial and tensorial contributions of the atomic polarizability cannot be neglected. As a consequence, the atom-light interaction is spin-dependent. The second part of the chapter will deal with with inter-atomic interactions in the presence of an external magnetic field. As it was explained in chapter 1, the DDI plays a key role in dipolar gases. In this section I will focus on one aspect of the DDI which is the dipolar relaxation; a binary loss mechanism dependent on the strength of the applied magnetic field. I will start by reminding the theoretical model from which we can derive the 2-body loss rate constant, and I will then present and discuss our experimental results.

3.1 Optical light shift and photon-scattering rate

Let us start by recalling the equations connecting the atomic polarizability to the optical potential felt by atoms in the presence of an external laser field. We consider an atomic cloud submitted to a laser beam of angular frequency ω and intensity $I(r)$. The atoms are in the state $|\beta J M_J\rangle$, where J is the total angular momentum, M_J is the azimutal quantum number corresponding to the projection of the angular momentum on the quantization axis and β contains all the remaining quantum numbers.

The presence of a laser beam will induce an energy shift on the atomic levels. This effect is the well known light shift, or also called the dynamical Stark shift. For a laser beam which electric field polarization is set by the complex unit vector $\mathbf{u}$, the light shift operator takes the following form [105]:

$$\hat{V}_J = -\frac{1}{2\epsilon_0 c} I(r) \times \left(\alpha_s(\omega)\hat{\mathbb{1}} - i\alpha_v(\omega)\left[\mathbf{u}^\star \times \mathbf{u}\right]\frac{\hat{\mathbf{J}}}{2J} + \alpha_t(\omega)\frac{3\left[\left(\mathbf{u}^\star\cdot\hat{\mathbf{J}}\right)\left(\mathbf{u}\cdot\hat{\mathbf{J}}\right)+\left(\mathbf{u}\cdot\hat{\mathbf{J}}\right)\left(\mathbf{u}^\star\cdot\hat{\mathbf{J}}\right)\right]-2\hat{\mathbf{J}}^2}{2J\left(2J-1\right)} \right) \tag{3.1}$$

where the coefficients $\{\alpha_s, \alpha_v, \alpha_t\}$ stand for scalar, vector and tensor dynamic dipole polarizabilities respectively and $\hat{\mathbf{J}}$ is the total spin operator.

The first remark that one can make is that the vector part vanishes for a linear polarization of the laser electric field as $[\mathbf{u}^\star \times \mathbf{u}] = 0$. Secondly, the tensor part vanishes for a total spin $J = 1/2$ (*cf.* eq. (3.4)). The situation is different for lanthanide atoms like Dysprosium or Erbium that have respectively $J = 8$ and $J = 6$ in their ground state.

Moreover the quadratic dependence on M_J of the tensor part opens the door to spin-dependent manipulation of the atomic system. This kind of selective atom-light interaction can be used to create non-classical spin states, as it will be explained in the chapter 5.

The difficulty remains in the correct determination of the atomic polarizabilities as it requires a good knowledge of the excitation spectrum of the atomic species. They can be calculated using the following formulas [69]:

$$\alpha_s = -\frac{1}{\sqrt{3\left(2J+1\right)}}\alpha_J^{(0)}(\omega) \tag{3.2}$$

$$\alpha_v = \sqrt{\frac{2J}{\left(J+1\right)\left(2J+1\right)}}\alpha_J^{(1)}(\omega) \tag{3.3}$$

$$\alpha_t = \sqrt{\frac{2J\left(2J-1\right)}{3\left(J+1\right)\left(2J+1\right)\left(2J+3\right)}}\alpha_J^{(2)}(\omega) \tag{3.4}$$

where $\left\{\alpha_J^{(0)}(\omega), \alpha_J^{(1)}(\omega), \alpha_J^{(2)}(\omega)\right\}$ take into account the parameters of all dipole-allowed transitions. They can be obtained by a sum-over-state formula:

$$\alpha_J^{(K)}(\omega) = \sqrt{2K+1} \times \sum_{J'} (-1)^{J+J'} \begin{Bmatrix} 1 & K & 1 \\ J & J' & J \end{Bmatrix} |\langle J' || \mathbf{d} || J \rangle|^2 \times \frac{1}{\hbar} \Re \left[\frac{1}{\omega_{J'J} - \omega - i\Gamma_{J'}/2} + \frac{(-1)^K}{\omega_{J'J} + \omega - i\Gamma_{J'}/2} \right] \tag{3.5}$$

In the equation (3.5), $|\langle J' || \mathbf{d} || J \rangle|^2$ denotes the reduced dipole transition element from spin state J to an intermediate spin state J', $\omega_{J'J}$ is the transition frequency and $\Gamma_{J'}$ is the linewidth of the spin state J'. The curly brackets correspond to the Wigner 6-j symbol. The photon-scattering operator can be obtained in the same fashion by replacing $-\frac{1}{2\epsilon_0 c}$ by $\frac{1}{\hbar\epsilon_0 c}$ in eq. (3.1) and taking the imaginary part of:

$$\left[\frac{1}{\omega_{J'J} - \omega - i\Gamma_{J'}/2} + \frac{(-1)^K}{\omega_{J'J} + \omega - i\Gamma_{J'}/2} \right].$$

The estimation of the photon-scattering rate is very important, as it sets the typical time for coherence and atom losses.

For Dy, a few theoretical [101, 69] and experimental [36, 106, 107, 102] investigations were carried out with the goal of determining the values of α_s, α_v and α_t, but the effects of the anisotropy on the trap depth and the heating rate were less treated. The anisotropic character of the dynamical polarizability was studied in an Erbium atomic ensemble [108], where it was demonstrated that the depth of the optical dipole trap depends on the laser field polarization. The potential depth is linked to the total polarizability by

$$U_0 = -\frac{1}{2\epsilon_0 c} \Re \left[\alpha_{tot}(\omega) \right] I_0$$

where α_{tot} is the total polarizability (accounting for the scalar, vector and tensor contributions), $I_0 = \frac{2P}{\pi w_x w_y}$ is the intensity at the center of a Gaussian laser beam of power P and $\{w_x, w_y\}$ are the beam waists. The determination of α_{tot} was done by measuring ω_i, $i \in \{x, y\}$, the radial trapping frequencies as a function of the light polarization. The value of $\alpha_{tot}$was then extracted through the use of the following relation:

$$\omega_i = \sqrt{\frac{4\alpha_{tot} P}{\epsilon_0 c \pi w_x w_y w_i^2 m}}$$

To recapitulate, the anisotropy of the dynamical polarizability leads to a dependency of the light-shift operator on the laser field polarization. Recent results obtained in our transport beam show that for some specific laser polarizations, the light-shifts of the ground and excited states are identical [109], in a similar fashion to the effect obtained with a *magic* wavelength.

Next we will discuss the lifetime and heating of a cold atomic sample in the ODT and their dependence on the laser field polarization. A good knowledge of this dependence allows one to choose the most suitable experimental parameters, in terms of light polarization and magnetic field orientation, in order to increase the lifetime and minimize the heating. This optimization is crucial for the transport of atoms from the MOT chamber to the glass cell.

Two sets of measurements were carried out in order to characterize the effects of the polarizability anisotropy: the first was done with a laser beam at a wavelength λ, of 1070 nm (the transport beam, described in chapter 1) and the second, close to the 626 nm narrow transition that is used both for the MOT and for spin dynamics experiments (see chapter 5).

3.2 Lifetime and heating in a dipole trap at λ = 1070 nm

The electronic excitation spectrum of Dysprosium is quite complex due to the unpaired electrons of the submerged 4f shell. The calculation of the polarizabilities at λ = 1070 nm far detuned from any resonance, should account for all excited states. In practice, it is mostly the broad transitions corresponding to the different excited state manifolds $J' = \{7, 8, 9\}$ (with $\lambda_7 = 404.7$ nm, $\lambda_8 = 418.8$ nm and $\lambda_9 = 421.291$ nm) that contribute to the value of α_s, but the spin-dependent terms are actually dominated by the rest of the spectrum.

For a laser beam with a general polarization along $\mathbf{u} = \cos\theta\mathbf{z} + e^{i\phi}\sin\theta\mathbf{x}$, the photon-scattering rate can be written as follows:

$$\hat{\Gamma}_{sc,J} = \frac{1}{\hbar\epsilon_0 c} I(r) \left[\alpha'_s(\omega)\hat{\mathbb{1}} + \frac{\alpha'_v(\omega)}{2J} \sin 2\theta \sin\phi \hat{\mathbf{J}}_\mathbf{y} \right.$$
$$\left. + \alpha'_t(\omega) \frac{3}{J(2J-1)} \left(\cos^2\theta \hat{\mathbf{J}}_\mathbf{z}^2 + \sin^2\theta \hat{\mathbf{J}}_\mathbf{x}^2 + \sin 2\theta \cos\phi \left(\frac{\hat{\mathbf{J}}_\mathbf{z}\cdot\hat{\mathbf{J}}_\mathbf{x} + \hat{\mathbf{J}}_\mathbf{x}\cdot\hat{\mathbf{J}}_\mathbf{z}}{2} \right) - \frac{\hat{\mathbf{J}}^2}{3} \right) \right. \quad (3.6)$$

where α'_s, α'_v and α'_t are the imaginary parts of the scalar, vector and tensor polarizability, respectively. No experimental measurements exist for these three coefficients at $\lambda = 1070$ nm. However, the calculated values for $\lambda = 1064$ nm read: $\{\alpha'_s, \alpha'_v, \alpha'_t\} = \{49.4, -11.3, 5.8\}$ a.u.. It shows that the vector and tensor contributions are considerable and should be taken into account.

3.2.1 Case of a circular polarization

Let us now consider a circularly polarized ODT, *i.e.* $\mathbf{u} = \frac{\mathbf{z} \pm i\mathbf{x}}{\sqrt{2}}$ (in this case the quantization axis is the $\hat{\mathbf{y}}$ axis). We denote σ^+ and σ^- the right and left handed polarizations respectively. The photon-scattering rate reads:

$$\hat{\Gamma}_{sc,J} = \frac{1}{\hbar\epsilon_0 c} I(r) \left[\alpha'_s(\omega)\hat{\mathbb{1}} \pm \frac{\alpha'_v(\omega)}{2J}\hat{\mathbf{J}}_\mathbf{y} - \alpha'_t(\omega)\frac{3\hat{\mathbf{J}}_\mathbf{y}^2 - \hat{\mathbf{J}}^2}{2J\,(2J-1)} \right] \tag{3.7}$$

and the projection over the state $|J, M_J\rangle$ gives:

$$\langle J, M_J|\hat{\Gamma}_{sc,J}|J, M_J\rangle = \frac{1}{\hbar\epsilon_0 c} I(r) \left[\alpha'_s(\omega) \pm \alpha'_v(\omega)\frac{M_J}{2J} - \alpha'_t(\omega)\frac{3M_J^2 - J\,(J+1)}{2J\,(2J-1)} \right] \tag{3.8}$$

with $(\pm)$ corresponding to the $\sigma^{(\mp)}$ polarization. The lifetime in the dipole trap is expected to reach its maximal value for a σ^- polarization, for an atomic sample spin polarized in the ground state $|J = 8, M_J = -8\rangle$ (the quantization axis is set by an external magnetic field along the y direction). On the one hand, the photon-scattering rate is reduced in such a configuration according to eq. (3.8), and on the other hand, the only possible excitation occurs between $|J = 8, M_J = -8\rangle$ and $|J = 9, M_J = -9\rangle$; thus the sample remains spin polarized in the absolute ground state and dipolar relaxations are prohibited. In order to verify this prediction, we measure the lifetime in the ODT as a function of the polarization. We set the **B** field to be coinciding with the propagation direction of the beam. We extract the decay time τ with an exponential fit. Results are presented in Fig. 3.1. The two sets of data correspond to the same direction of **B**-field but with opposite polarities, so the σ^- polarization (squares) is transformed into a σ^+ polarization (circles). The angle $\theta = 0$ defines the angle of the $\lambda/4$ wave-plate that gives a circular polarization ($\sigma^\pm$).

Our experimental result confirms the hypothesis made above: the lifetime is maximal for a σ^- polarization.

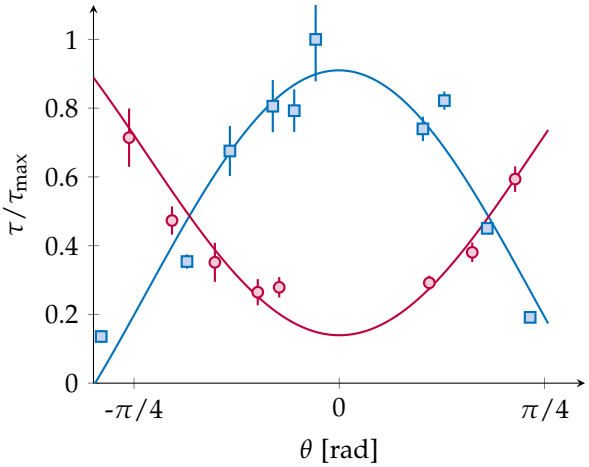

Figure 3.1 *– Variation of the lifetime in the ODT as function of the polarization. θ denotes the angle of the $\lambda/4$ wave-plate, $\theta = 0$ gives the σ^+ (circle) and σ^- (square) polarizations. The two curves correspond to the B-field pointing into opposite directions.*

3.2.2 Case of a linear polarization

We prepare the MOT in the spin-polarized regime, as it was explained in the previous chapter. In this conditions, the MOT equilibrium position is well below the zero of the quadrupole magnetic field (which is at the center of the MOT chamber). We use a vertical bias **B**-field to adjust the zero position in order to have a spatial matching of the MOT and the ODT. Then it is not possible to set a circular polarization for the trap. Let us now consider the case where the laser beam is linearly polarized in the $\{x, z\}$ plane (*i.e* for $\phi = 0$). The quantization axis is set by an external magnetic field, $\mathbf{B} = B\,\mathbf{z}$. The Rayleigh scattering rate (process after which the atom returns to its initial state) is given by:

$$\begin{aligned}\left\langle J, M_J|\hat{\Gamma}_{sc,J}|J, M_J\right\rangle = \frac{1}{\hbar\epsilon_0 c} I(r) \left[\alpha_s'(\omega)\right. \\ \left. + \alpha_t'(\omega)\frac{3}{J\,(2J-1)}\left[M_J^2\left(\cos^2\theta - \frac{1}{2}\sin^2\theta\right) + J\,(J+1)\left(\frac{1}{2}\sin^2\theta - \frac{1}{3}\right)\right]\right.\end{aligned} \tag{3.9}$$

The heating rate due to the gained recoil energy after the spontaneous emission can be deduced from eq. (3.6):

$$\dot{Q} = \frac{\hbar^2 k^2}{2m}\Gamma_{sc,J} \tag{3.10}$$

with $k = \frac{2\pi}{\lambda}$ being the wave vector and m the atomic mass.

For a spin polarized atomic sample in the absolute ground state $|J = 8, M_J = -8\rangle$, we

can see from eq. (3.9) that the heating rate is minimal for $\theta = \pi/2$, *i.e.* a laser polarization perpendicular to the magnetic field direction. Experimentally, we measure the number of loaded atoms in the ODT as function of its polarization angle θ, as well as the in situ size of the cloud which is proportional to $\sqrt{T}$. As one can see in Fig. 3.2, we get the expected behaviour: the heating is maximal for a linear polarization parallel to the magnetic field direction and it is π-periodic. Also, we compare the ratio between the maximal and minimal expected heating (*cf.* Fig. 3.3) calculated using the theoretical values of the polarizability given in ref. [69], with the observed one: $\dot{Q}_{th}(\theta = 0)/\dot{Q}_{th}(\theta = \pi/2) = 1.19$ and $\sigma^2_{exp}(\theta = 0)/\sigma^2_{exp}(\theta = \pi/2) = 1.23(13)$. The agreement between the model and our results is relatively good.

To make sure that the observed behaviour is not due to Raman transitions caused by

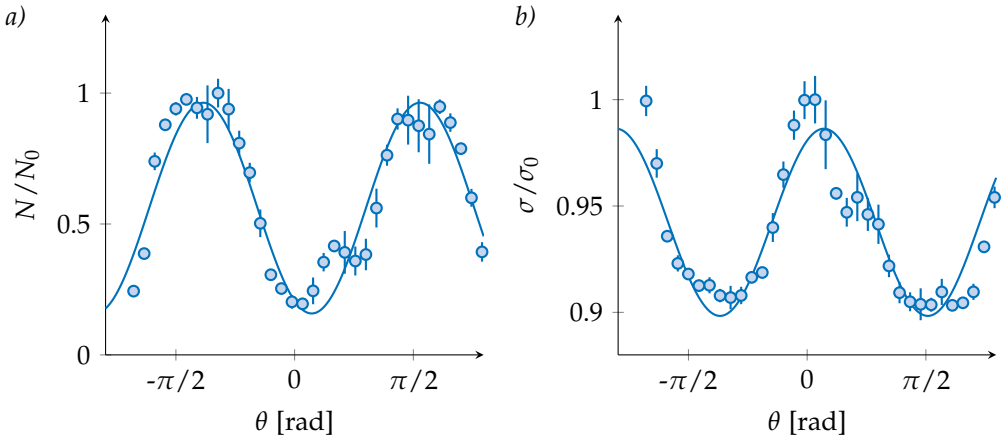

Figure 3.2 *– a) Atom number loaded into the dipole trap as a function of the laser beam polarization. We normalize to N_0, the atom number loaded in the trap for a horizontal polarization and a vertical magnetic field. b) Variation of the cloud size with the laser beam polarization normalized to the maximum value.*

the multi-mode character of the IPG laser, as it was explained in ref. [107], we repeat the same experiment with a single-mode laser[a], working at λ = 1064 nm with P = 45 W. The latter is focused at the MOT position with a waist similar to the previously used IPG laser ($w \simeq 35$ μm).

The same behaviour is recorded and clearly indicates that Raman transitions induced by the multimode nature of the laser have no significant effect on the temperature increase (*cf.* Fig. 3.4).

To summarize, we find that the behaviour of the far detuned ODT at $\lambda = 1070$ nm depends on the polarization of the laser field. This anisotropic effect is not observed for

[a] Azur Light fibre laser ALS-IR-1064-50-I-SM

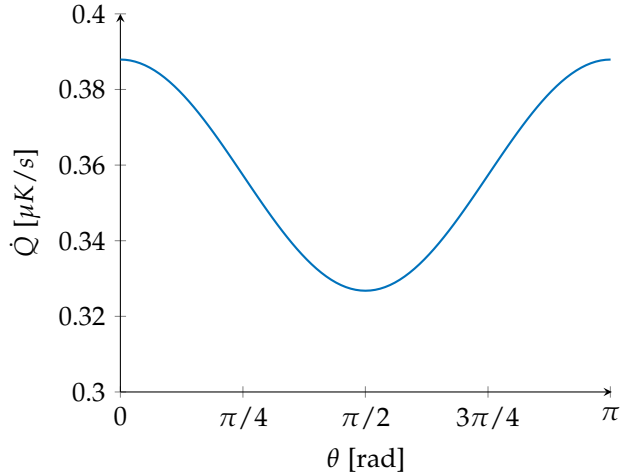

Figure 3.3 *– Calculated heating rate for a linearly polarized laser beam with $\lambda = 1070$ nm, $P = 45$ W and $w = 35$ µm. The initial sate is the absolute ground state $|J = 8, M_J = -8\rangle$.*

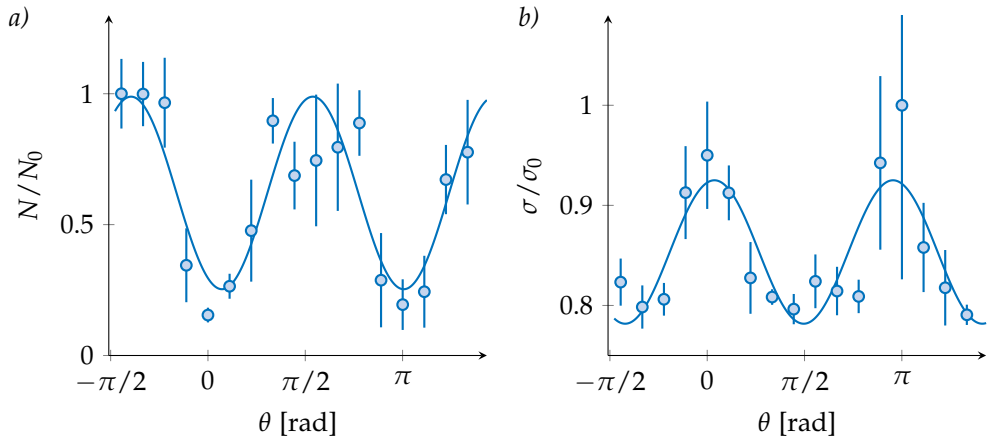

Figure 3.4 *– a) Variation of the loaded atom number in the single-mode laser beam with respect to its polarization, to be compared to the behaviour in a multi-mode laser beam (Fig. 3.2). We normalize to N_0 the maximal loaded atom number. b) Variation of the cloud size with respect to the polarization normalized to the maximum value.*

alkalis for example, showing the importance of the vector and tensor contributions from the dynamical polarizability. For the transport beam, we choose a linear polarization perpendicular to the vertical quantization axis. This polarization can be decomposed as $\frac{1}{2}(\sigma^- + \sigma^+)$. We have also demonstrated that the σ^- would be the optimal polarization for loading the ODT if the direction of the magnetic field can be set arbitrary with respect to the beam propagation. As for the σ^+ contribution it can be neglected due to the small Clebsch-Gordon coefficient between the levels $|J = 8, M_J = -8\rangle$ and $|J' = 9, M'_J = -7\rangle$ (*cf.* Fig. 3.6).

3.3 Lifetime and heating in a dipole trap at λ = 626 nm

The narrow transition at λ = 626 nm between $J = 8$ and $J = 9$ is used for the MOT and for the manipulation of the atomic spin (*cf.* chapter 1 and chapter 5). Since it is a transition relatively isolated from the rest of the excitation spectrum, the calculation of the atomic polarizability can be done by neglecting all other transitions. We then get:

$$\{\alpha_s, \alpha_v, \alpha_t\} = \frac{3\pi\epsilon_0 c^3}{\omega_0^3}\frac{\Gamma}{\Delta}\left\{\frac{9}{51}, \frac{152}{153}, -\frac{40}{153}\right\} \tag{3.11}$$

with ω_0 being the resonance frequency of the transition, Γ its linewidth and Δ the laser detuning from the resonance. The imaginary parts of the polarizability are proportional to the real parts, with: $\alpha_i' = \frac{\Gamma}{2\Delta}\alpha_i$ for $i = \{s, v, t\}$.
In contrast to the case λ = 1070 nm studied previously, the real part of the tensor polarizability is now negative. Then one should expect an opposite behaviour for the heating with respect to the laser field polarization. In other words, we expect to see minimal heating rate for a polarization parallel to the local magnetic field.

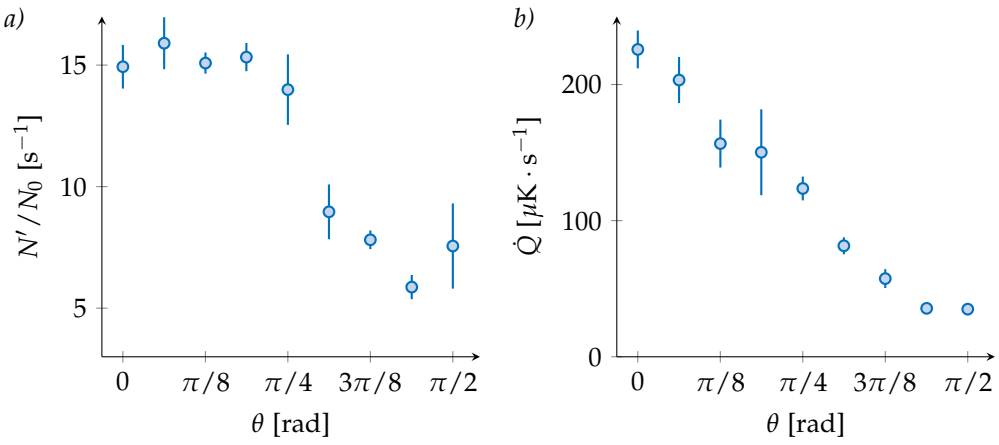

Figure 3.5 – *a) Atom loss rate as a function of the polarization. We normalize to the initial atom number before applying the red beam. b) Heating rate as a function of the polarization. θ denotes the angle between the polarization unit vector and the vertical axis.*

Experimentally, we measure the atom number decay and the heating of a cloud submitted to a red beam with different polarization. Experimental results (Fig. 3.5) show an opposite trend to the expected one. This is due to the fact that one should take into account also the heating due to the energy released after a dipolar relaxation; process

in which two atoms undergo a collision followed by a spin flip of one or both atoms (this process can be neglected for far detuned traps, treated previously, as it will be explained in the following). This dipolar relaxation interaction is studied in detail in the next section. In order to see effects due to dipolar relaxation, we need to have a spin mixture sample. This is possible due to Raman scattering, a two-photon process that changes the spin state of the atom. The Raman rate is proportional to the product of the Clebsch-Gordan coefficients linking the two spin states (given in Fig. 3.6 for the relevant states).

We can separate two cases:

- if the laser beam is linearly polarized parallel to the magnetic field, the atom can be excited to the state $\mid J' = 9,\ M_J = -8 \rangle$ and subsequently decay to the state $|J = 8, M_J = -7\rangle$ by spontaneous emission (scheme presented in red in Fig.3.6). The probability to find the atom in the state $M_J = -7$ is then $P_{\pi,-7} \propto (-0.333)^2\ (-0.943)^2 \simeq 0.1$.
- if the laser beam is linearly polarized, perpendicular to the magnetic field direction, then we can consider that we have a superposition between a σ^- light and a σ^+ light (blue scheme). For the σ^- light, the only possible transition is between $\mid J' = 9,\ M_J = -9 \rangle$ and $|J = 8, M_J = -8\rangle$, thus the sample remains spin-polarized. While for the σ^+ light, the probability to end up in $M_J = -7$ is: $P_{\sigma^+,-7} \propto 0.081^2\ 0.457^2 \simeq 0.001$.

We see that the probability to transfer atoms to the $M_J = -7$ spin state is a hundred time larger for a laser polarization parallel to the magnetic field direction in comparison with a polarization perpendicular to this latter. Also, we can compare the heating due to dipolar relaxation to the one expected from photon-scattering. The experiment was carried out at a magnetic field of 1 G amplitude. The energy due to the Zeeman splitting is: $\Delta E/k_B = g_J \mu_B B = 83\ \mu$K. This energy is comparable to the one gained by the atom due to Rayleigh photon-scattering during the experimental sequence. With our experimental parameters, we calculate the increase of the temperature during the 50 ms holding time, we get $\Delta T\,(\theta = \pi/2) = 86\ \mu$K and $\Delta T\,(\theta = 0) = 19\ \mu$K. Experimentally, we measure lower temperature increase ($\Delta T\,(\theta = \pi/2) = 11\ \mu$K and $\Delta T\,(\theta = 0) = 1.8\ \mu$K). In fact, there is another process that comes into play which is plain evaporation.

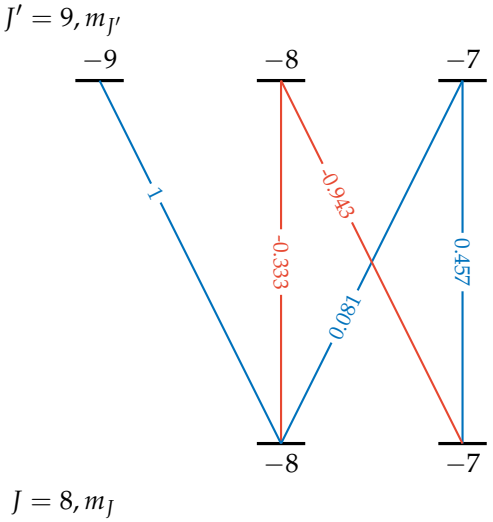

***Figure 3.6** – Clebsch Gordon coefficients for the $J = 8 \rightarrow J' = 9$ transition. Only $M_J < -7$ are presented.*

3.4 Dipolar relaxation

The dipolar relaxation is an exothermic process consisting in an inelastic collision in a non-zero magnetic field, followed by a spin flip of one or both atoms and an energy release corresponding to the Zeeman energy difference between the initial and final state. The released energy can be translated into atom losses if it exceeds the trap depth, otherwise it leads to a heating of the sample. This process limits the atomic density in a trap and can prevent reaching quantum degeneracy.

3.4.1 Theoretical derivation of the two-body loss rate and its dependence on the B-field

In this section, I will derive the expression of the two-body loss rate, following the model presented in ref. [110].

The dipolar interaction potential between two spin states $\hat{\mathbf{J}}_1$ and $\hat{\mathbf{J}}_2$ is given by:

$$U_{\mathrm{DDI}}(r) = \mu_0 (g_J \mu_B)^2 \frac{\left(\hat{\mathbf{J}}_1 \cdot \hat{\mathbf{J}}_2\right) - 3\left(\hat{\mathbf{J}}_1 \cdot \hat{\mathbf{r}}\right)\left(\hat{\mathbf{J}}_2 \cdot \hat{\mathbf{r}}\right)}{4\pi r^3} \tag{3.12}$$

with $r = |\mathbf{r}| = |\mathbf{r_2} - \mathbf{r_1}|$ the interatomic separation. The interaction potential U_{DDI} is invariant under a simultaneous rotation of the spin and the spatial coordinates with respect to a chosen axis, thus the total angular momentum is conserved. On the contrary, the projection of the spin momentum varies by $\Delta M_J = 0, \pm 1$ and the projection of the

orbital momentum by $\Delta l = 0, \pm 2$, which means that the spin flip is accompanied by a spinning of the atomic pair.

We consider two spin states oriented along the quantization axis **z**, we can then decompose the tensor part of eq. (3.12) in terms of $J_+ = \left(J_x + iJ_y\right)$ and $J_- = \left(J_x - iJ_y\right)$, the raising and lowering spin operators.

$$\begin{aligned}\hat{\mathbf{J}}_\mathbf{1} \cdot \hat{\mathbf{J}}_\mathbf{2} - 3\left(\hat{\mathbf{J}}_\mathbf{1} \cdot \hat{\mathbf{r}}\right)\left(\hat{\mathbf{J}}_\mathbf{2} \cdot \hat{\mathbf{r}}\right) = & J_{1z}J_{2z} \\ & + \frac{1}{2}\left(J_{1+}J_{2-} + J_{1-}J_{2+}\right) \\ & - \frac{3}{4}\left(2\bar{z}J_{1z} + \bar{r}_- J_{1+} + \bar{r}_+ J_{1-}\right) \times \left(2\bar{z}J_{2z} + \bar{r}_- J_{2+} + \bar{r}_+ J_{2-}\right)\end{aligned} \tag{3.13}$$

we define $\bar{z} = \frac{z}{r}$, $\bar{r}_+ = \frac{x+iy}{r}$ and $\bar{r}_- = \frac{x-iy}{r}$, with $\{x, y, z\}$ are the position operators. We can isolate three different contributions:

- the $J_{1z}J_{2z}$ and $\bar{z}J_{1z}\bar{z}J_{2z}$ terms describe elastic collisions that conserve the spin of each atom.

- the $\left(J_{1+}J_{2-} + J_{1-}J_{2+}\right)$ term describes a spin exchange between the pair but the total spin is conserved.

- the terms responsible for the dipolar relaxation are the following: $\bar{z}J_{1z} \cdot \bar{r}_+ J_{2-}$, $\bar{r}_+ J_{1-} \cdot \bar{z}J_{2z}$ for a single spin flip, and $\bar{r}_+ J_{1-} \cdot \bar{r}_+ J_{2-}$ for a double spin flip.

In the presence of an external magnetic field, the Zeeman sub-levels are splitted and the energy difference between two successive spin states is equal to $\Delta E = g_J \mu_B B$. Let us consider two colliding atoms with $|\mathbf{K_i}| = k_i$ and $|\mathbf{K_f}| = k_f$ the relative momenta corresponding to the initial and final states $|\mathbf{i}\rangle$ and $|\mathbf{f}\rangle$. The energy conservation condition sets:

$$\frac{\hbar^2 k_f^2}{2m_r} = \frac{\hbar^2 k_i^2}{2m_r} + \Delta M_J \times g_J \mu_B B \tag{3.14}$$

where $m_r = \frac{m}{2}$ is the reduced mass.

In order to understand the dependence of the dipolar relaxation on the magnetic field, we need to derive the collision cross-section σ that links the expected two-body loss rate

β_{dr} to experimental conditions (*e.g.* the temperature of the cloud, the magnetic field, *etc.*). β_{dr} can be accessed experimentally by measuring the decay rate for different **B**-field amplitudes.

The collision cross-section can be calculated using scattering theory. For relatively weak magnetic field, the dipole-dipole interaction can be treated using perturbation theory and one can apply the first order of the Born approximation (check ref. [111] for the detailed calculation). This approximation is valid if the following condition is fulfilled: $R_{\mathrm{dd}} k_i \ll 1$, with $R_{\mathrm{dd}} = \frac{m\mu_0 \left(g_J \mu_B\right)^2 J^2}{4\pi\hbar^2}$ being the characteristic length scale of the dipole-dipole interaction potential. In other words, this approximation is valid if the amplitude of the dipole-dipole interaction is weak with respect to other energy scales of the system or for a low energy system. R_{dd} is on the order of 20 nm for Dy in its ground state, which means that the temperature of the sample should be $\leq 5\ \mu$K to be in the regime where the approximation is valid. Otherwise, one should take into account molecular potentials while calculating the scattering cross-sections. In the Born approximation, the cross-section is given by:

$$\sigma = \left(\frac{m}{4\pi\hbar^2}\right)^2 \frac{1}{k_i k_f} \left[\int |\tilde{U}_{\mathrm{DDI}}\left(\mathbf{K_i} - \mathbf{K_f}\right)|^2 \delta\left(|\mathbf{K_f}| - k_f\right) \mathrm{d}\mathbf{K_f} \right. \\ \left. + \epsilon \int \tilde{U}_{\mathrm{DDI}}\left(\mathbf{K_i} - \mathbf{K_f}\right) \tilde{U}^{\star}_{\mathrm{DDI}}\left(-\mathbf{K_i} - \mathbf{K_f}\right) \delta\left(|\mathbf{K_f}| - k_f\right) \mathrm{d}\mathbf{K_f} \right. \quad (3.15)$$

where $\tilde{U}_{DDI}(\mathbf{K})$ is the Fourier-transform of the DDI potential, contracted between the initial state $|\mathbf{i}\rangle$ and final state $|\mathbf{f}\rangle$:

$$\tilde{U}_{DDI}(\mathbf{K}) = \int \langle \mathbf{i}|U_{DDI}(\mathbf{r})|\mathbf{f}\rangle e^{-i\mathbf{K}\cdot\mathbf{r}} d^3r = \mu_0 \left(g_J \mu_B\right)^2 J_1 J_2 \left(\cos^2\alpha - \frac{1}{3}\right) \quad (3.16)$$

with α being the angle between **K** and the magnetic field **B**. The ϵ factor is equal to +(-)1 if the two colliding particles are bosons (fermions) with identical spin states either in the incoming or outgoing channel, and 0 if the spin states are different in both incoming and outgoing channel.

In the context where the two colliding atoms are initially both in the maximally stretched

state $|J, M_J = +J\rangle$, solving eq. (3.15) gives:

$$\begin{aligned}
\sigma_0 &= \frac{16\pi}{45} J^4 \left(\frac{\mu_0 \left(g_J \mu_B\right)^2 m}{4\pi\hbar^2} \right)^2 \left[1 + \epsilon h(1)\right] \\
\sigma_1 &= \frac{8\pi}{15} J^3 \left(\frac{\mu_0 \left(g_J \mu_B\right)^2 m}{4\pi\hbar^2} \right)^2 \left[1 + \epsilon h(k_f/k_i)\right] \frac{k_f}{k_i} \\
\sigma_2 &= \frac{8\pi}{15} J^2 \left(\frac{\mu_0 \left(g_J \mu_B\right)^2 m}{4\pi\hbar^2} \right)^2 \left[1 + \epsilon h(k_f/k_i)\right] \frac{k_f}{k_i}
\end{aligned} \tag{3.17}$$

$\{\sigma_0, \sigma_1, \sigma_2\}$ are respectively the cross-sections for elastic collisions and 1,2 spin-flip inelastic collisions. The $h(x)$ function is defined as:

$$h(x) = -\frac{1}{2} - \frac{3}{8} \frac{\left(1 - x^2\right)^2}{x\left(1 + x^2\right)} \ln\left(\frac{(1-x)^2}{(1+x)^2} \right) \tag{3.18}$$

For a thermal cloud, the incoming momentum is given by $k_i = \frac{m v_{\text{rel}}}{2\hbar}$ and one has to average over all possible relative velocities v_{rel}. The thermal averaging of a function $f(v_{\text{rel}})$ can be calculated using:

$$\langle f(v_{\text{rel}}) \rangle_{th} = \left(\frac{m}{4\pi k_B T} \right)^{3/2} \int_0^\infty 4\pi v_{\text{rel}}^2 e^{-m v_{\text{rel}}^2/(4k_B T)} f(v_{\text{rel}}) \mathrm{d}v_{\text{rel}} \tag{3.19}$$

Fig. 3.7 shows the variation of the ratio $\langle k_f/k_i \rangle_{th}$ with the temperature of the sample for three different values of the applied magnetic field. The calculation is done for a single spin-flip ($\Delta M_J = 1$). The variation of the function $h(\langle k_f/k_i \rangle_{th})$ with the temperature is also presented.

In our case, we are rather in the situation where $M_J < J$. Then the cross-sections need to be adjusted with respect to the different cases. We suppose that we have only atoms in the two lowest spin states $|J = 8, M_J = -8\rangle$ and $|J = 8, M_J = -7\rangle$ (*cf.* experimental realization in the next section). The possible collisions that can take place are:

- **From a spin polarized to a spin mixture pair with 1 spin-flip:**
  $\mid M_{J_1} = -7,\ M_{J_2} = -7 \rangle \ \rightarrow \ \mid M'_{J_1} = -8,\ M'_{J_2} = -7 \rangle$. The corresponding cross-section is given by:

$$\sigma_{1,\epsilon=1}^{p \rightarrow m} = \sigma_1 (M_{J_1} - 1)^2 \left(J^2 + J - M_{J_1}^2 + M_{J_1}\right) / \left(2J^3\right) \tag{3.20}$$

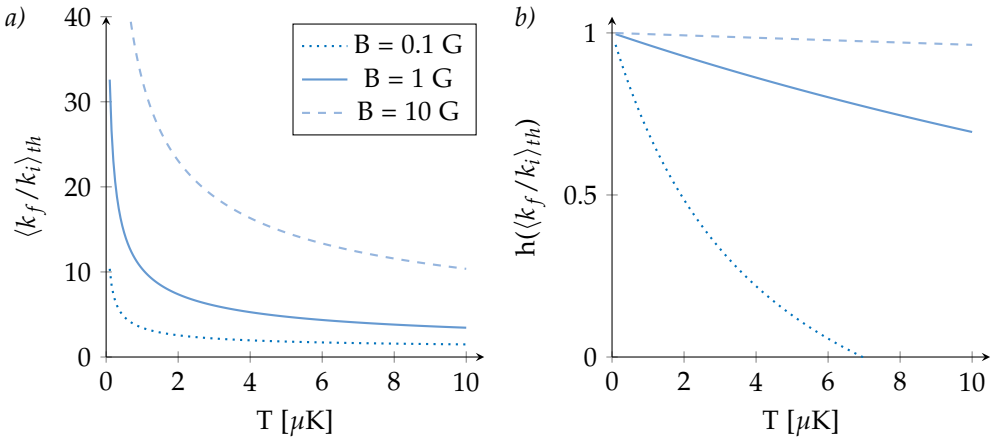

Figure 3.7 – *a) The variation of the ratio $\langle k_f/k_i\rangle_{th}$ with the temperature for different values of the magnetic field. The calculation is done for a single spin-flip, i.e. $\Delta M_j = 1$. b) The corresponding $h(\langle k_f/k_i\rangle_{th})$ function.*

- **From a spin polarized to a spin polarized pair with 2 spin-flips:**
  $\mid M_{J_1} = -7, M_{J_2} = -7 \rangle \rightarrow \mid M'_{J_1} = -8,\ M'_{J_2} = -8 \rangle$. The corresponding cross-section is given by:

$$\sigma^{p\to p}_{2,\epsilon=1} = \sigma_2 \left(J^2 + J - M^2_{J_1} + M_{J_1}\right)^2 / \left(4J^2\right) \tag{3.21}$$

- **From a spin mixture to a spin polarized pair with 1 spin-flip:**
  $\mid M_{J_1} = -7,\ M_{J_2} = -8 \rangle \rightarrow \mid M'_{J_1} = -8,\ M'_{J_2} = -8 \rangle$. The corresponding cross-section is given by:

$$\sigma^{m\to p}_{1,\epsilon=1} = \sigma_1 (M_{J_1})^2 \left(J^2 + J - M^2_{J_1} + M_{J_1}\right) / \left(2J^3\right) \tag{3.22}$$

$\sigma_{\{1,2\},\epsilon}$ are given by eq. (3.17). The notation $\sigma^{a_2\to a_3}_{a_1,\epsilon=1}$ corresponds to the cross section for $a_1 = \{1,2\}$ spin-flip with a gas initially in the state $a_2 = \{p,m\}$ that ends in the state $a_3 = \{p,m\}$ after the collision (p for a spin polarized state and m for a spin mixture). Now that we expressed cross-sections for the different cases, we can derive the 2-body loss coefficient β_{dr}.

- **For a spin polarized initial state (1^{st} and 2^{nd} cases):**

$$\beta^a_{dr} = \langle \left[\sigma^{p\to m}_{1,\epsilon=1} + \sigma^{p\to p}_{2,\epsilon=1}\right] v_{\mathrm{rel}} \rangle_{th} \tag{3.23}$$

- **For a spin mixture initial state (3^{rd} case):**

For a spin mixture sample with two different spin states a and b. One need to take into account contributions from collisions between $(a-a)$, $(b-b)$ and $(a-b)$ spin states. Loss rate coefficients β_{dr}^{a} and β_{dr}^{b} associated with $(a-a)$ and $(b-b)$ collisions can be obtained from eq. (3.23). The inter-species loss rate coefficient is given by:

$$\beta_{\mathrm{dr}}^{ab} = \beta_{\mathrm{dr}}^{ba} = \langle \left[\sigma_{1,\epsilon=1}^{m\to p} + \sigma_{1,\epsilon=0}^{m\to m} + \sigma_{2,\epsilon=0}^{m\to m} \right] v_{\mathrm{rel}} \rangle_{th} \tag{3.24}$$

In our experiment $\sigma_{1,\epsilon=0}^{m\to m} = \sigma_{2,\epsilon=0}^{m\to m} = 0$.

The $\langle\cdot\rangle_{th}$ braket denotes the thermal averaging.

3.4.2 Experimental investigation of the dipolar relaxation in a thermal gas

The experiment was carried out in the cross-dipole trap (*cf.* next chapter). We first perform an evaporation to 10% of the initial trap depth over 0.7 s in order to lower the temperature of the cloud, then we compress the trap to 50% of its initial value to suppress atom losses due to evaporation. This step is followed by a 450 ms waiting time to permit the system to reach an equilibrium state. At this point, we have a spin-polarized sample in the absolute ground state $|J=8, M_J=-8\rangle$. We then shine a red beam on the cloud to transfer a fraction of the population to higher M_J states. We use a laser beam linearly polarized parallel to the magnetic field direction, detuned by $\Delta = -2\pi\times 2$ GHz from the resonance. This beam couples the state $|J=8, M_J=-8\rangle$ to the state $|J'=9, M_{J'}=-8\rangle$, then by spontaneous emission, a fraction of the population can be transferred to the excited Zeeman sub-level $|J=8, M_J=-7\rangle$. In our experiment, we estimate the Raman scattering rate to be $\Gamma_{\mathrm{Raman}} \simeq 11.6\ s^{-1}$ between $|J=8, M_J=-8\rangle$ and $|J=8, M_J=-7\rangle$. We apply the red beam for a duration between 0 and 50 ms and we measure the atom number decay. The time evolution of the different states population is given by:

$$N_a'(t) = \Gamma_{\mathrm{Raman}} N_b(t) - \frac{1}{\tau} N_a(t) - \frac{\beta_a}{V_{\mathrm{mean}}} N_a^2(t) - \frac{\beta_{ab}}{V_{\mathrm{mean}}} N_a(t) N_b(t) \tag{3.25}$$

$$N_b'(t) = -\Gamma_{\mathrm{Raman}} N_b(t) - \frac{1}{\tau} N_b(t) - \frac{\beta_{ab}}{V_{\mathrm{mean}}} N_a(t) N_b(t) \tag{3.26}$$

where τ corresponds to the one-body lifetime fixed by collisions with the residual gas in the glass cell[a], V_{mean} is the average volume given by $V_{\mathrm{mean}} = \sqrt{8}\,(2\pi)^{3/2}\,\sigma_x\sigma_y\sigma_z$ with σ_i

[a] Its value is determined from independent measurements and estimated to $\tau = 21(4)$s.

being the $1/\sqrt{e}$ spatial width along the three axis $\{x, y, z\}$. We assume that the only state populated with $M_J > -8$ is $M_J = -7$ and we neglect population in higher M_J states. We define N_a to be the population of the state $|J = 8, M_J = -7\rangle$ and N_b the population in $|J = 8, M_J = -8\rangle$. Since b corresponds to the ground state $|J = 8, M_J = -8\rangle$, the two-body loss coefficient β_b is set to zero.

We solve the differential system numerically and we fit the solution to experimental

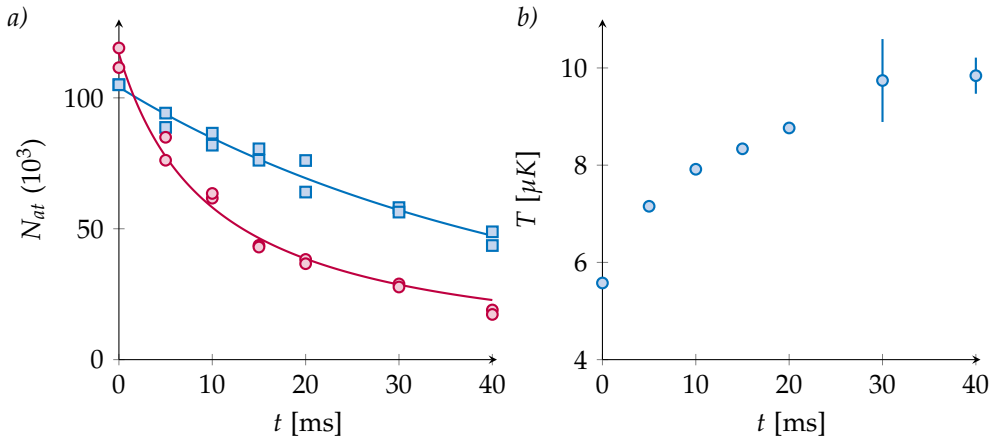

Figure 3.8 *– a)Example of decay curves for B = 1 G (square) and B = 10 G (circle). b) Temperature increase during a sequence*

data with four free parameters: initial atom number in each spin-state N_{a0} and N_{b0}, loss coefficient for collisions between two identical spins β_a and the inter-species loss rate β_{ab}. Results are presented in Fig. 3.9. The obtained values of the β_{ab} constant agree quite well with the theoretical description. The observed deviation between experimental values of the β_a and theoretical curves can be understood as follow: in our experiment, the population of the b state is much larger than the one in the a state ($N_a \sim 0.1 N_b$). As a consequence, the fitting of the β_a coefficient is less robust since the corresponding decay term is proportional to N_a^2.

The main uncertainty on the value of the loss coefficient β is related to the uncertainty on the volume. As one can see in Fig. 3.8, the temperature of the cloud increases during the time of the experiment, and so the average volume is not constant. For estimating error bars, we fit data for the lowest and highest temperature reached during the 50 ms evolution and we take the difference between the two obtained values.

The overall agreement between our experimental results and the theory is good. We should also note that our experimental conditions are at the limit of the validity of the Born approximation. In order to be totally rigorous, one should take into account

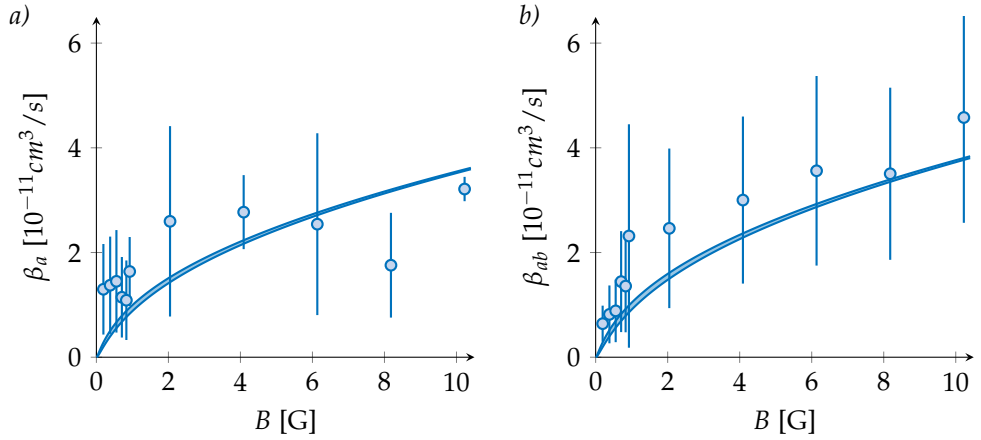

Figure 3.9 *– a) The β_a coefficient as a function of the B-field. b) The β_{ab} coefficient as a function of the B-field. The shaded areas give the calculated two-body loss coefficient for $T \in [5, 10]\ \mu K$.*

molecular potentials in the calculation of the two-body loss coefficient.

For large amplitudes of the magnetic field, the two-body loss coefficient is expected to vary as $\sqrt{B}$. We verify this dependence by plotting the fitted value of β as function of $\sqrt{B}$ (Fig. 3.10).

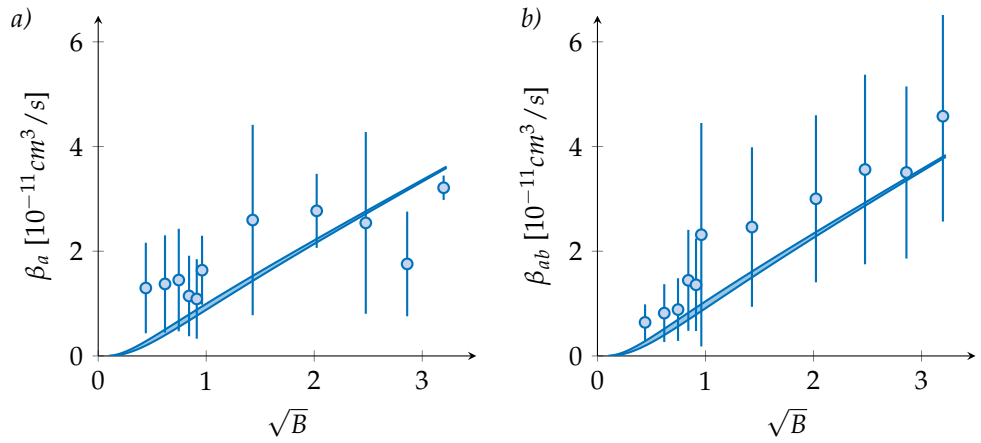

Figure 3.10 *– a) The β_a coefficient as a function of $\sqrt{B}$. b) The β_{ab} coefficient as a function of $\sqrt{B}$. The shaded areas give the calculated two-body loss coefficient for $T \in [5, 10]\ \mu K$.*

To conclude, those studies show how peculiar this atom is compared to alkali species and therefore the complexity it involves to cool towards quantum degeneracy. The understanding and characterization of these effects is essential for choosing optimal experimental parameters.

Chapter 4

Interactions between Dysprosium atoms and evaporative cooling

Forced evaporative cooling has proved to be an efficient technique allowing to reach quantum degeneracy [112, 113], ever since the first observation of a Bose-Einstein Condensate (BEC) in 1995 [5, 4]. The principle consists in reducing the depth of the trap holding the atomic cloud in a controlled manner such that highly energetic particles escape the trap; the thermalization of the remaining atoms leads to a narrower energy distribution, thus a colder cloud. I will expose in this chapter the study we performed on evaporative cooling in our Dy gas under different experimental conditions after transport from the MOT chamber to the science cell.

The chapter will be organized as it follows: in the first section, I will present the investigation of evaporative cooling in a single beam ODT and discuss the limits. The second part covers the loading and characterization of the crossed optical dipole trap (cODT). In the third section, I will set out the peculiarity of the anisotropy induced Feshbach spectrum in Dy that can be used to tune the nature and strength of interactions in the sample. Finally, I will report on the experimental investigation of evaporative cooling in the cODT.

4.1 Forced evaporation in a single far detuned optical beam

Let us start by recalling important parameters to consider for the cooling process. In a harmonic trap with a geometric mean trapping frequency $\bar{\omega} = (\omega_x \omega_y \omega_z)^{1/3}$, the

atomic peak density for a thermal gas is given by:

$$n_0 = N\bar{\omega}^3 \left(\frac{m}{2\pi k_B T}\right)^{3/2} \tag{4.1}$$

where N is the trapped atom number and T the temperature of the cloud. The efficiency of the evaporative cooling process depends on the elastic collision rate that ensures an efficient thermalization of the sample. The mean collision rate per atom is given by:

$$\Gamma_{el} = \frac{n_0}{\sqrt{8}}\sigma_{el} v \tag{4.2}$$

with $v = \sqrt{\frac{16 k_B T}{\pi m}}$ being the mean relative thermal velocity. For the elastic cross-section σ_{el}, one needs to take into account contributions from the short-range interactions mediated by the VdW potential and contributions from the long-range interactions due to DDI, as described in chapter 1 (section 2.3). Combining eqs. (4.1) and (4.2), we can rewrite the collisional rate as:

$$\Gamma_{el} = N\bar{\omega}^3 \frac{m}{2\pi^2 k_B T}(\sigma_D + \sigma_s) \tag{4.3}$$

As we can see the main reduction of the elastic collisions rate comes from lowering the ODT laser power since $\bar{\omega} \propto \sqrt{P}$. Hence the variation of the power profile over time has to be well chosen such that the temperature drop compensates for the trap depth reduction *i.e.* $\eta = U_0/k_B T$ remains constant, with U_0 denoting the trap depth. The goal of the evaporation is to increase the phase space density which is given by:

$$\text{PSD} = n_0 \Lambda_{dB}^3 = N\left(\frac{\hbar\bar{\omega}}{k_B T}\right)^3 \tag{4.4}$$

where Λ_{dB}^3 is the de Broglie wavelength. In a 3D harmonic trap, the BEC phase transition occurs at a value of the PSD $= \zeta(3) \simeq 1.2$.

Experimentally, we reach the glass cell with $\sim 1 \times 10^7$ atoms in the ODT at an initial temperature $T_{\text{initial}} \simeq 119\ \mu$K, which set $\Gamma_{\text{el, initial}} \simeq 450\ \text{s}^{-1}$ and $\text{PSD}_{\text{initial}} \simeq 2.1 \times 10^{-5}$. We need then to proceed with an evaporation sequence with a well chosen laser power profile in order to increase the PSD. It was shown in ref. [114] that for a harmonic trap, if the evaporation occurs with a constant[a] parameter $\eta = U/k_B T$, the optimal ramp for the

[a] this is not rigorously true during the evaporation sequence but it consists in a good starting point to understand the dynamics.

laser power that maximizes the PSD has the following form:

$$P(t) = P_0 \left(1 + \frac{t}{\tau_{\text{evap}}}\right)^{\xi} \tag{4.5}$$

with P_0 the initial laser power. We define $r = P_\text{f}/P_\text{i}$ the ratio between initial power and the reached power at the end of the evaporation. We define the characteristic time of the evaporation ramp as:

$$\tau_{\text{evap}} = t_{\text{evap}} \left(r^{1/\xi} - 1\right)^{-1} \tag{4.6}$$

where t_{evap} is the total duration of the ramp. We performed two sets of measurements to optimize the evaporation ramp. First, we set $r = 0.1$, $t_{\text{evap}} = 5$ s and we scan the power law exponent ξ (results presented on the left hand side in Fig. 4.1). Secondly, we keep the same ratio $r = 0.1$, we set $\xi = 1$ (τ_{evap} is negative in this case) and we scan the total duration of the ramp t_{evap} (results presented in Fig. 4.1, right panels). In Fig. 4.1, we introduce the evaporation's efficiency γ defined as:

$$\gamma = -\frac{\ln[\text{PSD}_{\text{final}}/\text{PSD}_{\text{initial}}]}{\ln[N_{\text{final}}/N_{\text{initial}}]} \tag{4.7}$$

We see that the optimal PSD that we can reach is 4 orders of magnitude lower than the condensation threshold. In fact we notice that the elastic collision rate is reduced by a factor ~ 10 with respect to its initial value. The thermalization becomes extremely slow, which is limited by the finite lifetime in the trap. The evaporation is almost stagnant, as lowering the trap depth results only in atom losses. The problem with a single beam trap is that the confinement along the axial direction is weak, hence the atomic cloud is quite elongated along this direction which results in a lower atomic density. To overcome this limitation one solution consists in increasing the atomic density by increasing the confinement of the trap. This can be done by intersecting the first ODT with a second one, and atoms will be trapped in the crossed region.

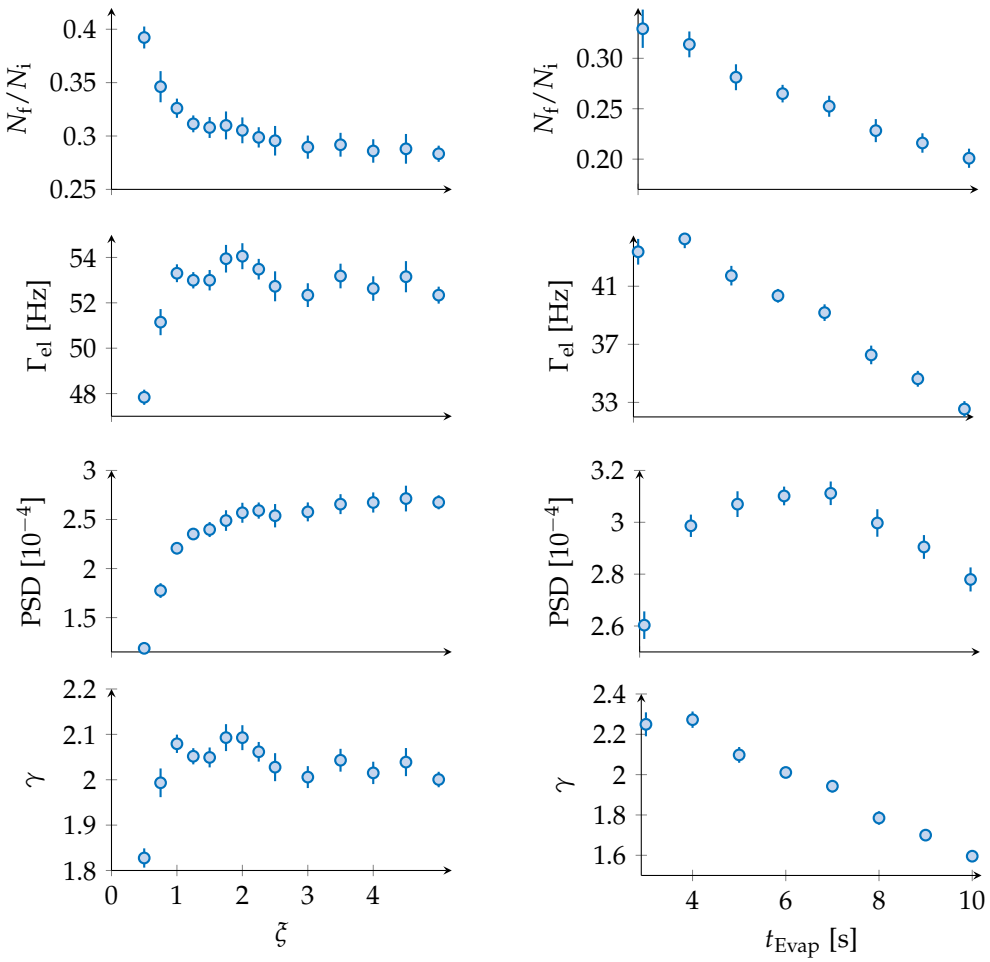

Figure 4.1 *– Evaporation in a single beam: the measured remaining atomic fraction, collisional rate, PSD and evaporation's efficiency (from top to bottom) as a function of the power law exponent ξ (left) and the evaporation total duration t_{evap} (right). For both sets of measurement the laser power is ramped down to 10% of its initial value. The data on the left were taking with $t_{evap} = 5$ s, and ξ was fixed to 1 for the data on the right.*

4.2 Crossed dipole trap

4.2.1 Characterization of the crossed dipole trap

We transfer the atoms from the transport beam to a crossed optical dipole trap (cODT) formed by two intersecting far detuned optical beams with a relative angle $\theta \simeq 90°$ (*cf.* Fig. 4.2). Both lasers[a] are single mode and operate at a wavelength $\lambda = 1064$ nm. Both optical beams have an elliptic shape $\{w_{x1}, w_{y1}\} = \{44.8, 28.3\}$ μm and $\{w_{x2}, w_{y2}\} = \{63.1, 40.9\}$ μm (here, y defines the vertical direction) and reach a maximum power on the atoms of 5 W and 9 W, respectively. In the crossed region, the overall trap depth is

[a] ALS-IR-10-1064-SF, Azur Light System

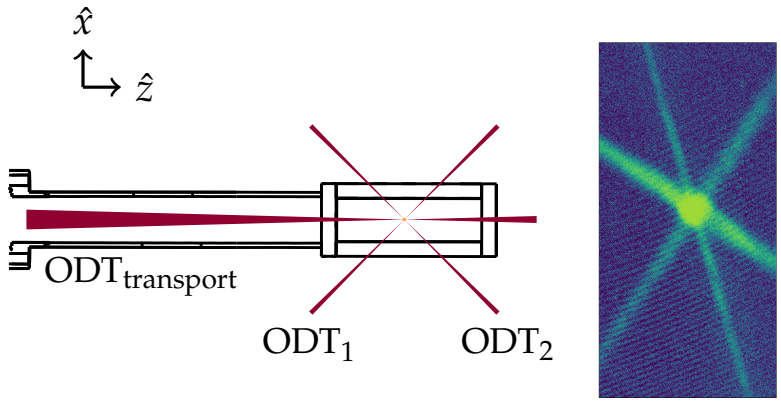

Figure 4.2 *– Left: top view of a schematic of the three ODTs crossing in the glass cell. Right: absorption imaging of the three ODTs.*

simply given by $U_{\text{cross}} = U_1 + U_2$, with U_1 (U_2) the trap depth of ODT$_1$ (ODT$_2$) alone. The effective waists of the crossed region can be obtained by:

$$w_{\text{eff,i}} = \left(\left(\frac{U_1}{U_{\text{cross}}} \frac{1}{w_{i1}^2} \right) + \left(\frac{U_2}{U_{\text{cross}}} \frac{1}{w_{i2}^2} \right) \right)^{-1/2} \tag{4.8}$$

where i denotes the horizontal and vertical directions $\{x, y\}$. The trapping frequency of the crossed region is equal to the quadratic sum of the two trapping frequencies for each beam $\omega_{\text{cross}} = \sqrt{\omega_1^2 + \omega_2^2}$ for the three axis $\{x, y, z\}$. For a gaussian beam, ω scales as $\sqrt{P}$ with P the total power. During the evaporation, the laser power is reduced and effects of gravity start to play a role. We are interested in the trap shape deformation along the vertical direction when taking into account the gravity $\mathbf{g} = g\hat{\mathbf{y}}$; we restrict the discussion to the potential along the $\hat{\mathbf{y}}$ axis only:

$$U(x = 0, y, z = 0) = -U_0 \exp\left(\frac{-2y^2}{w_{y0}^2} \right) - mgy \tag{4.9}$$

The potential shape can be characterized by the dimension less parameter $\alpha = \frac{mgw_{y0}}{U_0}$. If α is larger than a critical value $\alpha_c = 2/\sqrt{e} \simeq 1.213$ then the potential does not feature a minimum and atoms are lost. In the opposite case, the minimum exists and we denote $y = y^*$ its position. Nevertheless, the trap depth and as a consequence the trapping frequency are reduced. In Fig. 4.3, we plot the variation with α of the minimum position y^*, the trap depth U^* and the trapping frequency ω^*.

For $P = P_{\text{max}}$ we measure $\omega_{x0} = 2\pi \times 379$ Hz and $\omega_{y0} = 2\pi \times 792$ Hz. We measure also trapping frequencies of the crossed region for different powers along the vertical

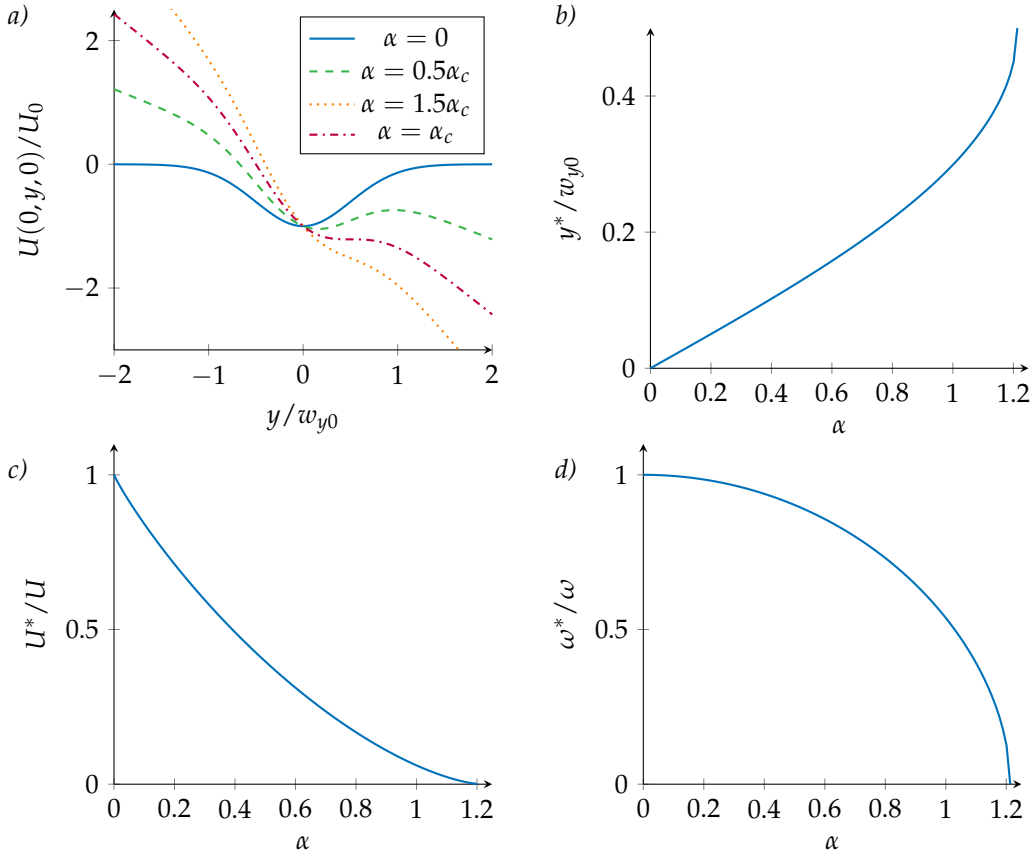

***Figure 4.3** – Gravity effects: a) deformation of the trap shape for different values of α. b) variation of the trap minimum position as a function of α. c) and d) reduction of the trap depth and trapping frequency with α, respectively.*

and horizontal directions. Results are reported in Fig. 4.4. For the horizontal direction (Fig. 4.4.*b*) the solid line corresponds to a frequency reduction given by $\omega_x(r) = \omega_{x0}\sqrt{r}$ with $r = P_f/P_i$. The measured values are well represented by this curve. For the vertical direction (Fig. 4.4.*a*) the square-root behaviour is plotted in dashed line. We see that the measured frequencies are well below the expected values from the ideal case. The solid line is a fit to the experimental data taking into account effects of gravity with one free parameter being the initial trap depth. We get $U_0/k_B = 148(5)$ μK, to be compared with the expected value for an ideal case which is $U_0/k_B = 195$ μK (the observed discrepancy can be due to the fact that the laser beams do not have ideal gaussian profiles). From now on, we use the result of the fit to determine the vertical trapping frequency as a function of the power.

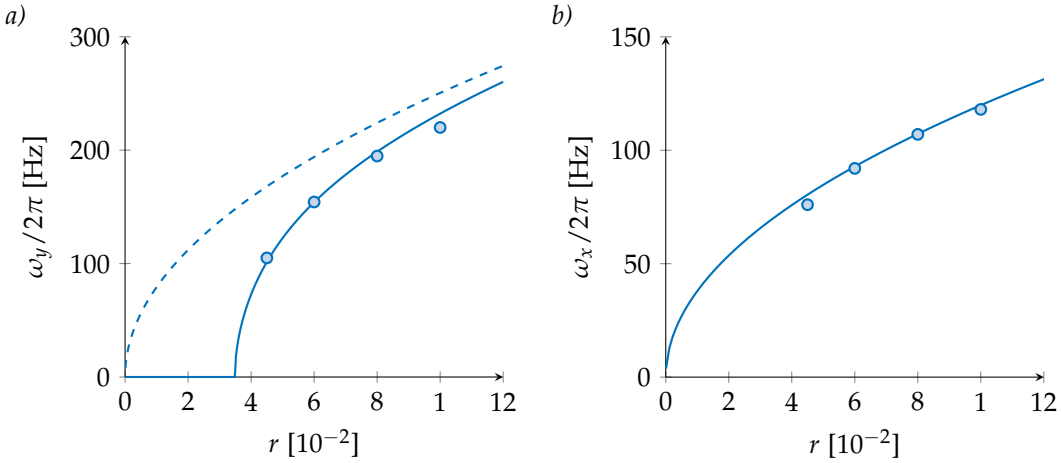

***Figure 4.4** – a) Vertical trapping frequency of the cODT as a function of $r = P_f/P_i$. In dashed line is the expected behaviour in the absence of gravity ($\omega = \omega_{max}\sqrt{r}$), and in solid line is the one with gravity effects. b) Horizontal trapping frequency as a function of r. The solid line presents the expected square-root behaviour.*

4.2.2 Optimizing the loading into the cross dipole trap

We start optimizing the loading of the cODT by adjusting the spatial overlap between the transport beam (IPG laser) and the cODT position. We measure the transferred atom number in the intersection region as a function of the final position of the IPG focal point (Fig. 4.5). We observe two local maxima separated by $\simeq 3$ mm that corresponds to the IPG Rayleigh length. Indeed the loading efficiency is higher out of focus since the effective volume of the transport beam becomes larger and coincides better with the effective volume of the cODT[a]. For $|z| > z_R$ the spatial overlap is too weak and the loading efficiency drops. This behaviour was observed also when loading the IPG beam from the MOT (chapter 2).

In order to have an efficient transfer from one trap to the other, the trap depths should be similar. In our case the IPG trap has a depth of $\simeq 1$ mK while the cODT depth is approximatively 7 times lower. Hence a first step of evaporation on the IPG alone is required. We performed two sets of measurement to optimize this evaporation ramp. The first sequence consists in optimizing the transferred atom number into the cODT as a function of the evaporation ratio $r = P_{\mathrm{IPG,f}}/P_{\mathrm{IPG,i}}$. We use a power profile for the IPG laser given by eq. (4.5) with $\xi = 1.75$ and $t_{\mathrm{evap}} = 2.5$ s. We plot in Fig. 4.6 the loaded atom number in the cODT (squares) as well as the atom number in IPG (without the

[a]The effective radial waist of the crossed region is on the order of 50 μm while the IPG waist is 34.5 μm.

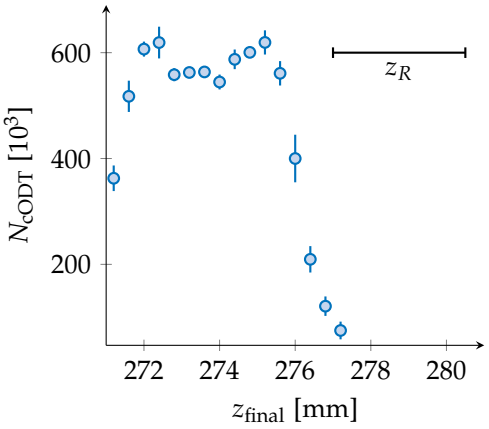

Figure 4.5 *– Loaded atom number in the cODT as a function of the final position of the transport beam focal point. z_R denotes the Rayleigh length of the transport beam. For this measurement, the depth of the transport beam was reduced to 15% of its initial value.*

cODT) as a function of r. The maximum is reached for $r = 0.15$ where we have a loading efficiency of $\sim 37\%$.

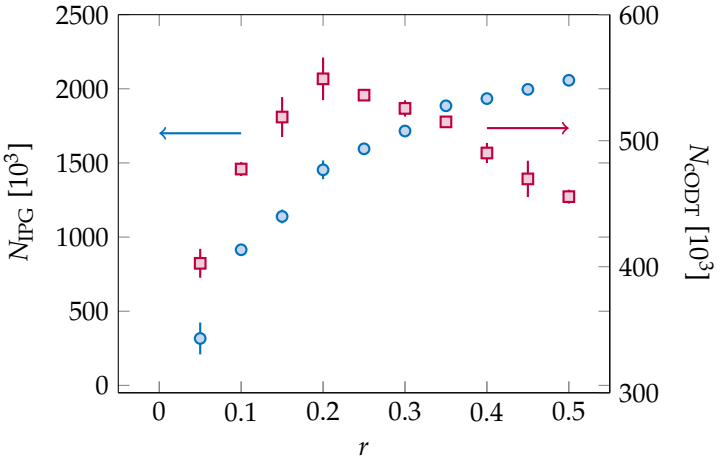

Figure 4.6 *– The transferred atom number from the IPG to the cODT (squares) and the remaining atom number in the transport beam in the absence of the cODT (circles) as a function of the IPG evaporation ratio r.*

To make sure that these parameters give the optimal starting condition for the evaporation sequence that will follow, we measure the PSD in the cODT after an evaporation ramp where the depth of this latter is reduced to 5% from its initial value. We scan both r and t_{evap} of the IPG evaporation step. Results are reported in Fig. 4.7. We fix $r = 0.15$ and $t_{\mathrm{evap}} = 3$ s.

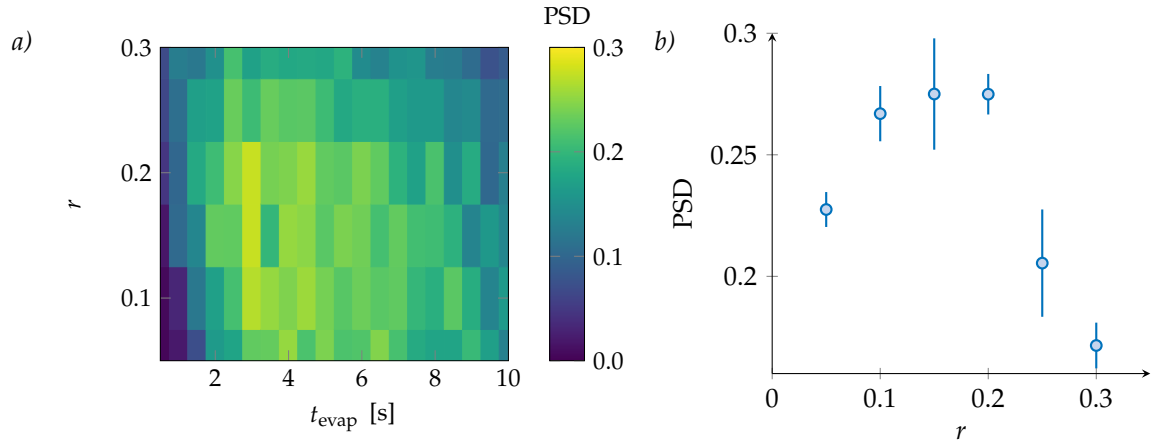

Figure 4.7 *– a) Measured PSD in the cODT as a function of starting conditions. We scan the IPG evaporation ratio r and duration t_{evap}. After the loading of the cODT, the IPG is turned off and we proceed with an evaporation sequence over the cODT depth down to 5% of its initial value. The PSD is measured at the end of this step. b) The measured PSD as a function of r for $t_{evap} = 3$ s.*

4.3 Controlling the interactions via Feshbach resonances

Feshbach resonances have emerged as an essential tool for tailoring interactions in cold atoms experiments [115]. For two colliding particles, a resonance appears when the energy of the entrance channel matches the energy of a bound state of a molecular potential, as described in Fig. 4.8.*a*. The energy of the closed potential V_{Closed} can be tuned thanks to the Zeeman effect by means of an external magnetic field. This is usually referred to as *magnetic Feshbach resonance*. It is also possible to use an external electric field [116] or an optical field to induce a Feshbach resonance [117, 118]. The use of magnetic fields is commonly implemented because of its ease and it will be the focus of this section.

In the presence of a Feshbach resonance, the phase shift is modified during a binary collision which results in field-dependent expression for the scattering length a (Fig. 4.8.*b*):

$$a(B) = a_{\text{bg}}\left(1 - \frac{\Delta}{B - B_0}\right) \tag{4.10}$$

with a_{bg} being the background scattering length, B_0 the pole of the resonance and Δ its width[a]. In a classical picture, the scattering length a can be seen as the radius of an effective hard sphere potential during a contact interaction. The elastic cross-section is thus proportional to a^2. As a result, one can tune the strength of the contact interaction by tuning the value of a. For dipolar gases, this experimental knob is very appealing as one can adjust the interplay between long-range DDI and the short-range contact interaction, *i.e.* by adjusting the ratio $\epsilon_{dd} = a_D/a$ (*cf.* chapter 1 section 2). This feature was exploited to reach the strongly dipolar regime that lead to the observation of a large span of dipolar effects such as magnetostriction [34], BEC collapse in a d-wave [119] or more recently the realization of quantum droplets in a Dy BEC [38]. It can be used also to stabilize the BEC and prevent its collapse due to DDI.

To detect the Feshbach spectrum, one technique consists in observing atom losses as

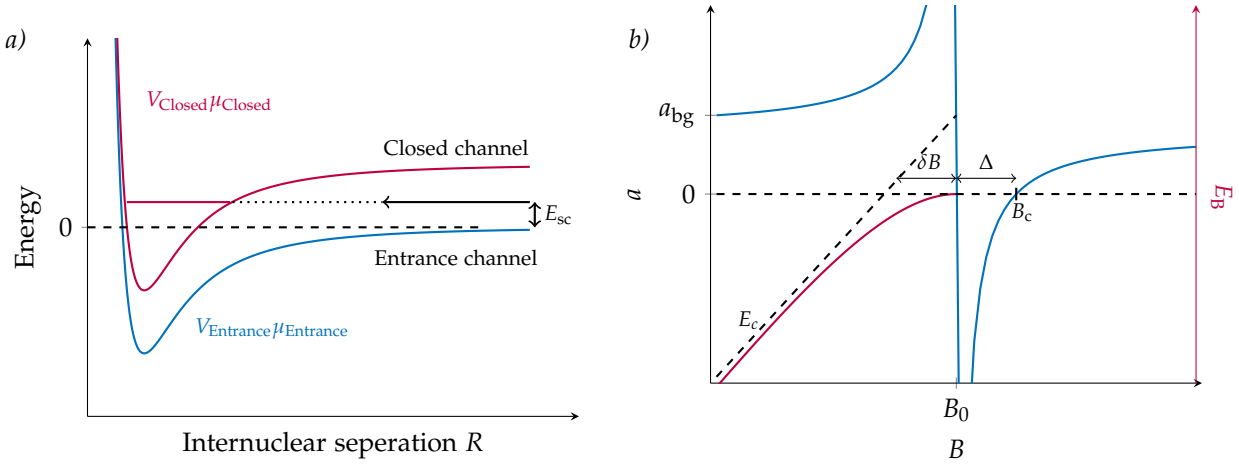

Figure 4.8 *– a) Schematic of molecular potentials during a binary collision. E_{sc} is the scattering energy at the entrance channel. A Freshbach resonance occurs if E_{sc} matches the energy of a bound-state of the closed channel. $\mu_{entrance}$ and μ_{closed} are the magnetic moments of the entrance and closed channels respectively. b) Schematic of the scattering length's variation with the magnetic field B (blue curve). The red curve presents the variation of the binding-energy with magnetic field (see text). B_0 denotes the resonance pole position, Δ is the resonance width, B_c is the zero crossing and δB is the zero binding-energy shift with respect to an open channel.*

a function of the applied magnetic field. Close to a resonance, losses driven by 3-body recombination are enhanced. A resonance pole position can be approximatively located as the magnetic field for which the atom loss is maximum. An example of a loss spectrum is presented in Fig. 4.9. The characterization of a resonance can for example be done by

[a]Defined as the magnetic field difference between the pole and the field corresponding to a null scattering length.

measuring the bound state energy versus magnetic field using a standard technique of molecular association by magnetic field modulation [120].

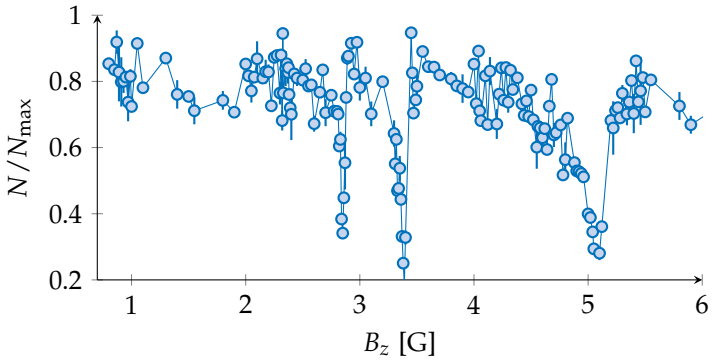

Figure 4.9 – *Measured loss spectrum for a magnetic field ranging from 1 to 6 G. The maximum loss positions correspond to Feshbach resonances poles. The measurement was done at $T = 1.5$ μK. N_{max} is the measured atom number far from resonances. We have $N_{max} \simeq 1 \times 10^4$.*

The experimental investigation of the Feshbach spectrum was performed for the three bosonic isotopes in their ground state [121, 120] over a large span of magnetic field while the Feshbach spectrum of fermionic isotopes is less treated (only one measurment for the isotope ^{161}Dy at low field). Few theoretical studies exist as well [122]. The first striking feature of the studied spectra is the high density of Feshbach resonances, a behaviour completely different from what has been observed in alkali-metal cold gases. We see in average between 3 and 5 resonances per Gauss.

This behaviour results from:

- the large number of Zeeman sub-levels leading to numerous closed channels,
- the various types of anisotropic interactions (DDI, anisotropic dispersion interaction) allow to couple together many different channels.

Experimental measurements report resonances at high and low fields (down to ∼0.2 G), with some broad resonances above a dense background of narrow ones. A sensitive dependence of the resonance density on the temperature of the sample was observed even in the nK regime [121]. As a matter of fact, the observed density exceeds the one predicted by theory assuming a zero temperature regime. This dependence on temperature signals the dominant role of higher partial waves in Dy.

4.3.1 Nature of Dy Feshbach spectrum

In alkali atom systems, Feshbach resonances occur due to couplings between hyperfine states that are absent for a Dy bosonic isotope. In fact, Feshbach resonances can only be induced by a coupling to rotating bound states in a Dy gas. Numerical calculations using coupled-channel technique [68, 122] show that anisotropy effects due to the DDI and the anisotropic dispersion interaction affect significantly the Feshbach spectrum.
Dy has a complex web of molecular potentials. For two atoms in their ground state $|J = 8, M_J = -8\rangle$, there is precisely one channel with zero relative orbital angular momentum l. Hence Feshbach resonances occur only via anisotropic coupling to bound states with $l \neq 0$, in opposition to alkali atoms in their lowest hyperfine level where multiple $l = 0$ (s-wave) channels are present. From a theoretical point of view, the hamiltonian describing the system has the following form:

$$H = \underbrace{-\frac{\hbar^2}{2m_r}\frac{\mathrm{d}^2}{\mathrm{d}R^2} + \frac{l^2}{2m_r R^2}}_{\text{radial and rotational energies}} + \underbrace{H_z}_{\text{Zeeman term}} + \underbrace{V(R,\chi)}_{\text{electronic term}} \tag{4.11}$$

where the electronic term $V(R,\chi)$ includes nuclear repulsion and anisotropic effects, it goes to zero for an inter-nuclear separation $R \to \infty$. χ takes into account all electronic variables (the nuclear spin $I = 0$ for Dy bosonic isotopes, but need to be taking into account for the fermionic case). The Zeeman term is given by:

$$H_z = g_J \mu_\mathrm{B} (J_{1z} + J_{2z})\mathrm{B} \tag{4.12}$$

with J_{1z} (J_{2z}) the spin operator along the quantization axis of atom 1 (2). In the basis $|J = J_1 + J_2, M_J, l, m_l\rangle = Y_l^{m_l}(\theta,\phi)|J, M_J\rangle$ the Zeeman and rotational hamiltonians are diagonal with an energy:

$$E = g_J \mu_\mathrm{B} M_J \mathrm{B} + \frac{\hbar^2 l(l+1)}{2m_r R^2}$$

The coupling between the basis vectors is mediated by the electronic term $V(R,\chi)$. The hamiltonian H conserves the projection of the total angular momentum $M_J = M_{J1} + M_{J2} + m_l$ and is invariant under the parity operation, thus only even (odd) l are coupled. For homo-nuclear collisions there are only coupling between states with even values of $J + l$.

As for the electronic hamiltonian $V(R,\chi)$, it conserves the projection Ω of J along the inter-nuclear axis but it does not conserve J. Under the Born-Oppenheimer approximation, it is possible to calculate the eigenenergies of $V(R,\chi)$ at each inter-nuclear separation R. It results in a total of 153 potentials divided in 81 and 72 potential curves with a gerade (superposition of even J states) and ungerade (superposition of odd J states) symmetries respectively. Since these potentials depend on the electronic structure of the atom, Feshbach resonances positions differ for different isotopes. We observe this behaviour experimentally in the measured loss spectra for ^{164}Dy and ^{162}Dy at low field that are shown in Fig. 4.10. In addition, fermionic isotopes exhibit even denser Feshbach spectrum due to the presence of a hyperfine structure [121].

On the one hand, if R is large enough such that the two atomic electronic clouds do not overlap, then $V(R,\chi)$ is the sum of the DDI potential and the VdW potential (the quadrupole-quadrupole potential can be neglected as it was demonstrated that its contribution is much smaller than the other two). On the other hand, for short range distances the coupling is more complex. It can be simplified when considering only coupling between electrons from the isotropic 6s shell. This approximation can be justified by the fact that the 4f shell is located deep within the electronic cloud and does not overlap significantly with the electronic cloud of a neighbouring atom.

The numerical calculations of the Feshbach spectrum using the described above model have two main results. First, several partial-waves contribute to a single resonance. As a consequence the usual labelling of Feshbach resonances based on the partial-wave that induces it (s-wave, p-wave, *etc*) does not apply in this case. Secondly, the positions and widths of the resonances converge only if a high number of partial-waves is included in the calculation.

Another feature of lanthanide atoms Feshbach spectrum is the chaotic character observed in the distribution of spacings between two successive resonances. This behaviour was observed in both Dy and Er systems [123, 124].

4.3.2 Characterization of a Feshbach resonance

We are interested in particular in a relatively broad resonance around 7 G, for the bosonic isotope ^{164}Dy, that we will use later during the evaporation sequence. First we start by calibrating the magnetic field using a radio-frequency (RF) spectroscopy technique. We have initially a trapped gas in the ground state $|J=8, M_J=-8\rangle$ in the

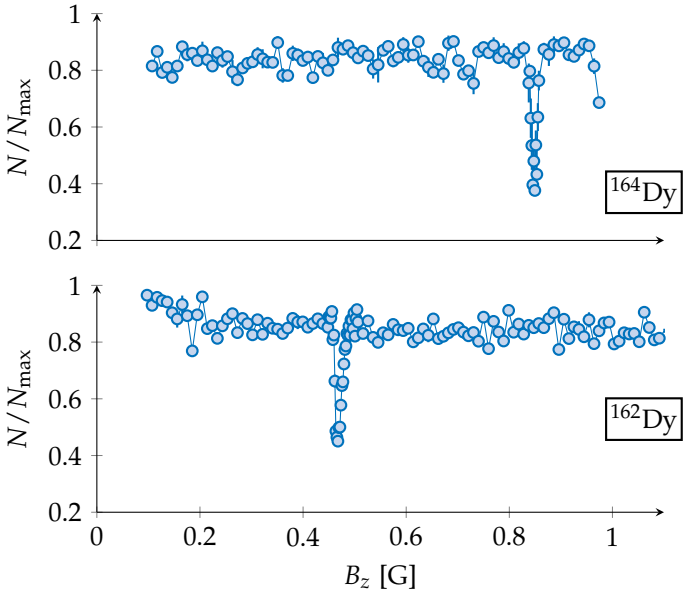

Figure 4.10 – *Measured loss spectrum with ^{164}Dy (top) and ^{162}Dy (bottom).*

presence of a large magnetic field $\mathbf{B} = B\hat{\mathbf{z}}$ such that higher Zeeman sub-levels can not be thermally populated. The Zeeman splitting between successive levels is given by:

$$\hbar\Delta_Z = g_J \mu_B B \tag{4.13}$$

$$\Delta_Z / B \simeq 2\pi \times 1.74\text{MHz/G} \tag{4.14}$$

We drive the system with a RF field $\mathbf{B}_{\text{mod}} = B_{\text{mod}} \cos\omega_{\text{mod}} t\hat{\mathbf{u}}$. In the weak excitation limit, only the first excited state $|J = 8, M_J = -7\rangle$ is populated. The excitation is monitored through atom losses induced by dipolar relaxation; we observe also an increase of the temperature close to the resonance (Fig. 4.11.*a* and *b*). We measure atom losses and the variation of the temperature for various values of the magnetic field and we fit the data with a Lorentzian curve to extract the resonance position. Results are reported in Fig. 4.11.*c*. The Feshbach resonance is identified as follows: we reduce the temperature to $T \simeq 1.5\mu$K (cODT evaporation to 10% of its initial power) at a low field $B \sim 0.5$ G, far from any resonance. We then ramp up the magnetic field to a target value in 100 ms. We hold the system for 2 s and we image the cloud after 5 ms time-of-flight (ToF) thanks to an absorption imaging technique. The magnetic field scan is done with 4 mG resolution and we average over six points. Results are presented in Fig. 4.12. We observe the presence of a double structure feature both in the atom loss and temperature spectra; we believe that they correspond to two different Feshbach resonances. In the following, we consider only

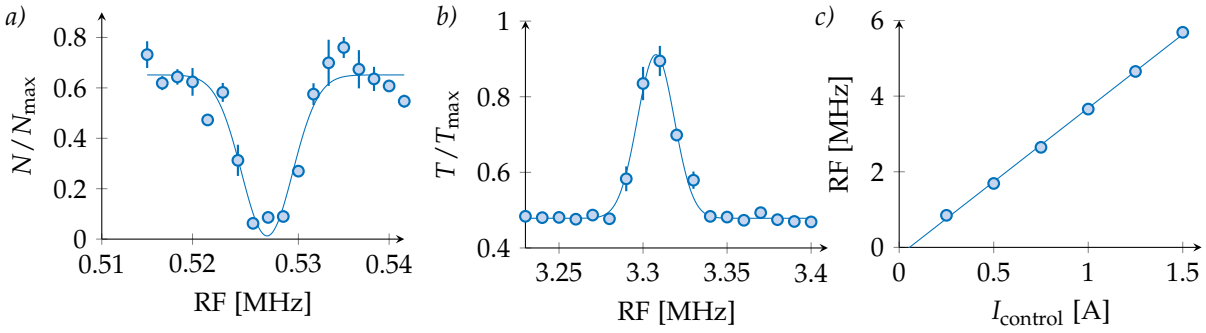

Figure 4.11 *– Rf spectroscopy: a) Normalized atom number as a function of the RF frequency for an applied magnetic field B≃ 0.5 G. The resonance position corresponds to the Zeeman splitting frequency between the levels $|J = 8, M_J = -8\rangle$ and $|J = 8, M_J = -7\rangle$. The observed atomic loss is due to dipolar relaxation. b) Temperature increase around the resonance. c) Calibration of the magnetic field: resonance frequency as a function of the applied current.*

the large peaks (*cf.* Fig. 4.12). We fit the atom loss data to extract the pole position. We recover $B_0 = 7.179(7)$ G. We determine the resonance width by fitting the temperature data. The width of a Feshbach resonance Δ is defined as the difference between the pole position B_0 and the zero-crossing of the scattering length B_c (*cf.* Fig. 4.8.*b*). When the scattering length a vanishes, the elastic cross-section reaches a minimum value (only contribution from the DDI) which leads to a reduction of the thermalisation efficiency resulting in an increase of the temperature. We measure $\Delta = 27(8)$ mG. We compare these values to the one reported by the Pfau group [1]. They give $B_0 = 7.117(3)$ G and $\Delta = 50(15)$ mG. The observed large difference on the width value can be due to different experimental conditions (different temperature for example). As it was explained above, the temperature affects drastically the Feshbach spectrum of Dy. The broadening of the resonance suggests contributions from higher order partial-waves to the collisional process. In addition, the presence of the double structure can lead to an uncertainty on the position and width of the resonance.

4.4 Forced evaporation in the cross dipole trap

At the end of the cODT loading step, the IPG laser is turned off and our starting conditions for the forced evaporative cooling ramp are reported in Tab.4.1

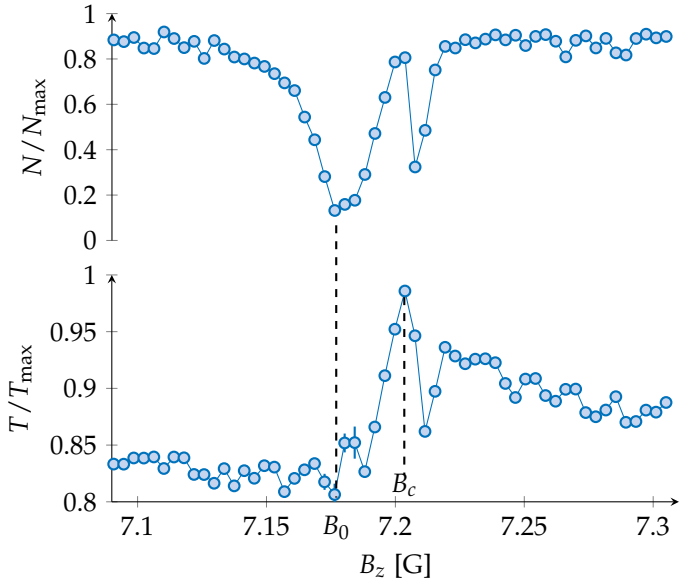

Figure 4.12 *– Feshbach resonance around B = 7 G. Top: loss spectrum around the Feshbach resonance. N_{max} is the atom number far from any resonance. Bottom: variation of the cloud temperature close to the resonance, normalized to the maximum reached value.*

N_{inital}	T_{inital} [μK]	Peak density [cm^{-3}]	$\Gamma_{\text{el, initial}}[2\pi \times \text{Hz}]$	$\text{PSD}_{\text{initial}}$
5.5×10^5	16	6.6×10^{12}	106	1.6×10^{-3}

Table 4.1 *– Initial conditions in the cODT*

We choose a ramp decomposed in n linear step for the cODT power profile. At each step the trap depth is reduced by a factor r, such that the trap depth at the end of the evaporation is given by:

$$U_{\text{final}} = r^n U_{\text{initial}} \tag{4.15}$$

The duration of each step is optimized by maximizing the final PSD (*i.e.* for $U = U_{\text{final}}$). We studied the forced evaporative cooling efficiency under different experimental circumstances.

4.4.1 Evaporation model

In the following, we describe a simple model, based on refs. [125, 126], that allows to calculate different physical quantities like the atom number or temperature of the cloud

during the evaporative cooling process.
For a potential with a maximal trap depth U_0, we define the truncation parameter $\eta = \frac{U_0}{k_B T}$ where T is the temperature of the sample. In the harmonic approximation, the potential seen by the atoms is given by:

$$U(r,t) = \begin{cases} -U_0(t) + \frac{1}{2}m\bar{\omega}^2 r^2 \ \text{ for } \ r < \sqrt{\frac{2U_0}{m\bar{\omega}^2}} \\ 0 \ \text{ otherwise} \end{cases}$$

The energy of the atomic sample can be obtained from:

$$E = \int \mathrm{d}\epsilon \rho(\epsilon)\epsilon f(\epsilon) \tag{4.16}$$

with $\rho(\epsilon)$ being the density of states and $f(\epsilon)$ the partition function. For a harmonic trap, we get:

$$E = 3\frac{N}{\beta}\frac{P(4,\eta)}{P(3,\eta)} \tag{4.17}$$

where N is the atom number and we define $\beta = 1/k_B T$. $P(n,\eta)$ is the regularized incomplete gamma function[a]. We can differentiate eq. (4.17) to obtain:

$$\frac{\dot{E}}{E} = \frac{\dot{N}}{N} + (1 - F(\eta))\frac{\dot{T}}{T} + F(\eta)\frac{\dot{U}_0}{U_0} \tag{4.18}$$

where we define the function $F(\eta) = 1 + 3\frac{P(4,\eta)}{P(3,\eta)} - 4\frac{P(5,\eta)}{P(4,\eta)}$.
A second information can be obtained from the different atom and energy loss processes:

$$\frac{\dot{N}}{N} = -\Gamma_{\mathrm{ev}} - k_1 - k_2\langle n\rangle - k_3\langle n^2\rangle \tag{4.19}$$

$$\frac{\dot{E}}{E} = -\Gamma_{\mathrm{ev}}^{(E)} - k_1 - k_2^{(E)} - k_3^{(E)} \tag{4.20}$$

In this general model, we define Γ_{ev} as the evaporation rate induced by atomic collisions and $\Gamma_{\mathrm{ev}}^{(E)}$ is the corresponding energy loss rate. k_1, k_2 and k_3 are 1, 2 and 3-body loss rates, respectively. Their corresponding energy loss rates are denoted with (E). Finally, n denotes the atomic density. For the following measurements, we neglect the 2 and 3-body losses. This approximation is valid for the following reasons:

[a] $P(n,\eta) = \frac{\int_0^\eta \mathrm{d}u u^{n-1}e^{-n}}{\int_0^\infty \mathrm{d}u u^{n-1}e^{-n}} \to 1$ for $\eta \to \infty$

- we are initially spin polarized in the absolute ground state, then 2-body losses mediated by the dipolar relaxation are prohibited;
- the atomic density is quite low thus 3-body losses are negligible.

The evaporation rate is proportional to the collisional rate Γ_{el} (eq. (4.2)). The correction due to the finite trap depth is given by:

$$\Gamma_{\text{ev}} = \Gamma_{\text{el}} \ e^{-\eta} \left(\eta - 4 \frac{P(4,\eta)}{P(3,\eta)} \right) \tag{4.21}$$

and the corresponding energy loss rate is:

$$\Gamma_{\text{ev}}^{(E)} = \Gamma_{\text{el}} \ e^{-\eta} \left[\eta(\eta+1) \frac{P(3,\eta)}{3P(4,\eta)} - \frac{4(\eta+1)}{3} - \frac{P(5,\eta)}{3P(4,\eta)} \right] \tag{4.22}$$

Eqs. (4.18), (4.19) and (4.20) form a differential equation system that describes the system evolution. We use this model to estimate our trap depth and the one-body loss rate.
We measured the lifetime and temperature evolution in the cODT for different maximum trap depths. For these measurements, we start by an evaporation phase where the trap depth is reduced by a ratio r. Then we re-compress the trap to its initial value, hence varying η. We solve the differential equations system numerically and we fit the result to our experimental data with two free parameters: the one-body lifetime $\tau = 1/k_1$ and the initial trap depth U_0. For the collisional rate, we use $a = 92\ a_0$ for the value of the elastic scattering length [127]. Fig. 4.13 shows an example of our results. The solid line on the temperature graph is the result of the numerical solution using for U_0 and τ the fitted values. The agreement between the model and the experimental data is quite good. The extracted values of U_0 and τ from all the experimental measurements are:

$$U_0 = 218(50)\mu\text{K}$$
$$\tau = 19.2(1.6)\ \text{s}$$

The large error bar on U_0 can be understood as we neglect different sources of heating, mainly technical heating proportional to the laser power. This effect will be studied in the last section of this chapter. The obtained 1-body loss rate agrees with the lifetime set by the vacuum in the science cell.

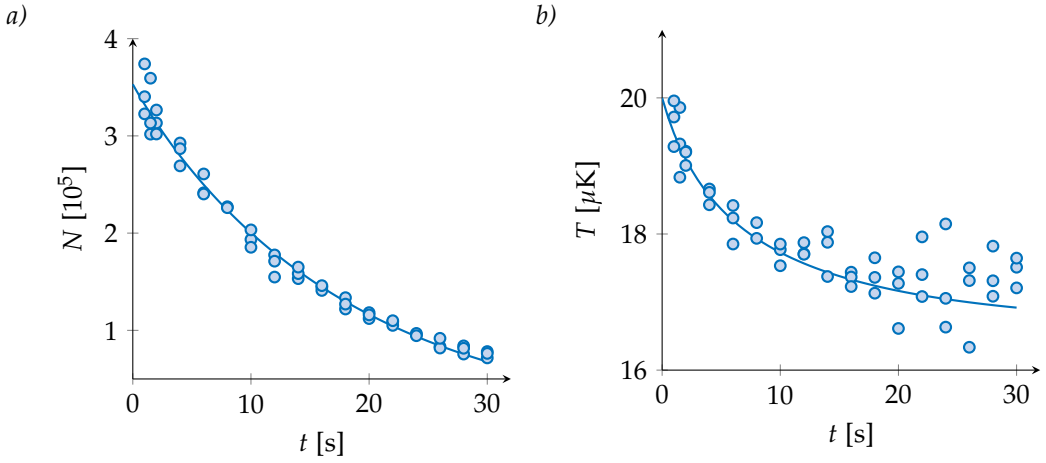

Figure 4.13 *– Variation of the atom number (a) and temperature (b) of the atomic cloud over time. The data were taken after a first evaporation step where the trap depth was reduced by a factor 2 then re-compressed to full power. The solid line is obtained by fitting the atom number decay using the evaporation model described in the text, with two free parameters: the initial trap depth U_0 and the one-body lifetime τ. The solid line on the temperature graph is the result of the theoretical model with U_0 and τ the fitted values.*

4.4.2 Gravity effects on the evaporation efficiency

In the second section of this chapter, we showed that gravity plays an important role when the trap depth is reduced. We study in this section the effects of gravity on the evaporation efficiency in three different situations:

- $\mathbf{g_{eff} = 0}$**:** we compensate the shift due to gravity by applying a magnetic field gradient.
- $\mathbf{g_{eff} = g}$**:** no compensation is applied.
- $\mathbf{g_{eff} = 2\ g}$**:** we add a magnetic field gradient to effectively double the effect of gravity.

For the three sets of measurement, the reached trap depth at the end of the evaporation ramp is 8.5% of its initial value, taking into account deformations due to gravity.
Fig. 4.14 shows the evolution of different physical quantities (atom number, temperature, PSD, *etc*) during the evaporation ramp for the three situations discussed above. At first sight, we do not observe an important difference between the three cases. In order to have a better estimation of the evaporation efficiency, we extract the efficiency coefficient

γ that we define here as:

$$\gamma = -\frac{\mathrm{d}\ln(\mathrm{PSD})}{\mathrm{d}\ln(N)} \tag{4.23}$$

Results are plotted in Fig. 4.15. We observe two different behaviours at large and low atom number. For the three sets of measurements the evaporation efficiency is higher at the beginning (for $N > 10^5$). The fitted values of γ in this regime are $\{2.22, 2.39, 2.54\}$ for $g_{\mathrm{eff}} = \{0, 1, 2\}$ g, respectively. For the final steps of the evaporation ramp, we get $\gamma = \{0.88, 1.23, 0.85\}$ for $g_{\mathrm{eff}} = \{0, 1, 2\}$ g, respectively.
To summarize, gravity tends to enhance the evaporation efficiency (can be seen as a 1D evaporation along the vertical direction). Nevertheless, the gain remains relatively small. In the case of the doubled gravity measurement, the trap is significantly deformed at the end of the evaporation ramp and does not have a gaussian shape any more.

4.4.3 Interaction effects on the evaporation efficiency

A possible origin of the observed efficiency reduction at the end of the evaporation ramp is the decrease of the collisional rate. Experimentally, we can tune it by working close to a Feshbach resonance. The following studies were performed close to the 7 G Feshbach resonance described in the previous section. For a reminder, the pole of the resonance is at $B_0 = 7.179(3)$ G and its width is $\Delta = 27(5)$ mG. We carry out a set of measurements where we vary the value of the applied bias field during the whole evaporation ramp. The trap depth is reduced to 6% of its initial value. The reached values at the end of the evaporation (atom number and temperature) are reported in Tab. 4.2. We compare these values to the one obtained far from a Feshbach resonance at $B \simeq 0.5$ G (also presented in Tab. 4.2). We see that we can achieve lower temperatures when approaching the resonance pole *i.e.* when increasing the scattering length a. We plot in Fig. 4.16 the attained PSD as a function of the applied magnetic field. The maximum value is obtained for $a \simeq 330\ a_0$ where we gain approximatively a factor of 4 with respect to the PSD value far from the resonance. Closer to the resonance pole, atom losses are increased hence the PSD decreases.

To conclude, we observe an enhancement of the evaporation efficiency when increasing the collisional rate. However, working close to a Feshbach resonance comes with the

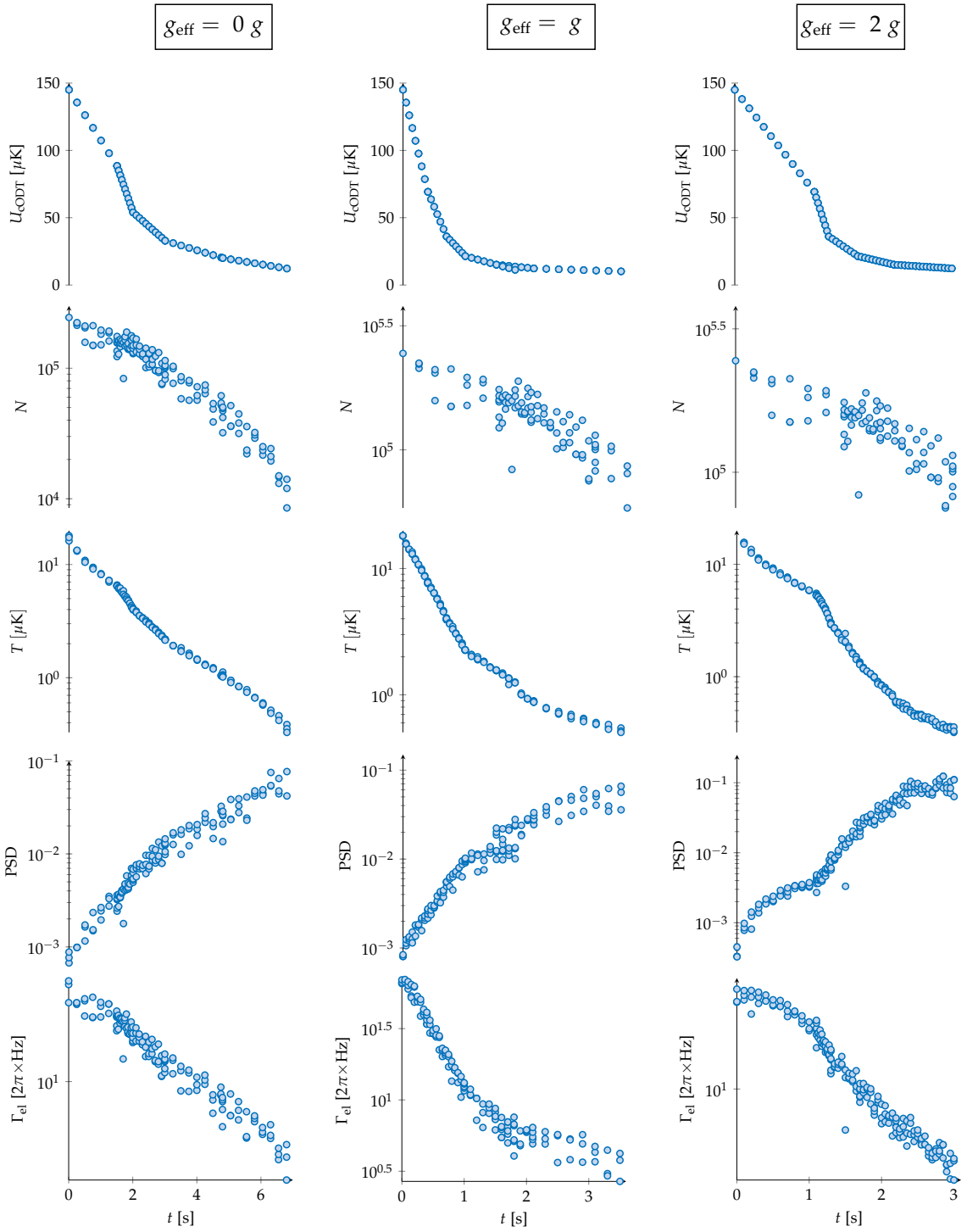

Figure 4.14 *– Gravity effects on the evaporation efficiency: evolution of the trap depth, atom number, temperature, PSD and collisional rate (from left to right) during the evaporation ramp. We compare the cases with a the gravity fully compensated, in the absence of compensation and with doubling the effects of gravity (from top to bottom).*

drawback of enhanced 3-body loss which scales as a^4 and therefore is extremely sensitive to field fluctuations. Possible solutions can be:

- increasing the collisional rate by rising the trapping frequencies (by changing the

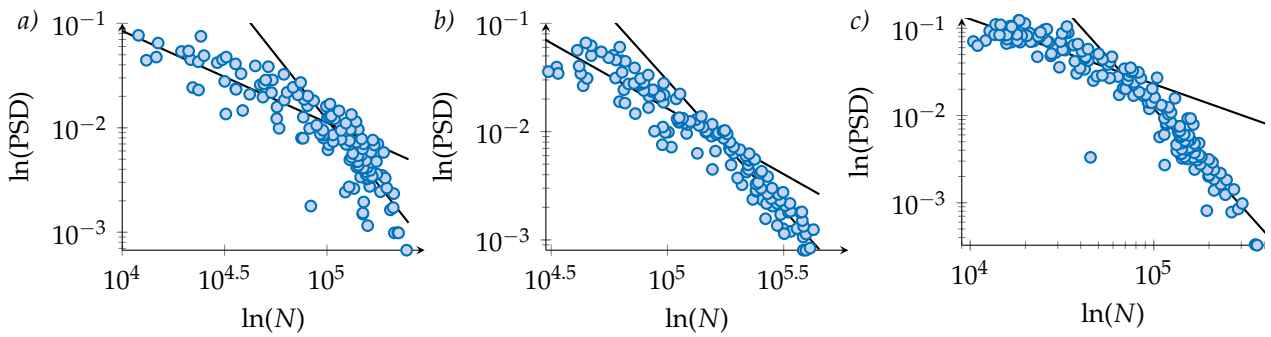

Figure 4.15 *– Gravity effects on the evaporation efficiency for $g_{eff} = 0\,g$ (a), $g_{eff} = 1\,g$ (b) and $g_{eff} = 2\,g$ (c).*

waist of the laser beams).

- working close to a Feshbach resonance only at the first steps of the evaporation ramp where the atomic density is still relatively small to avoid 3-body losses.

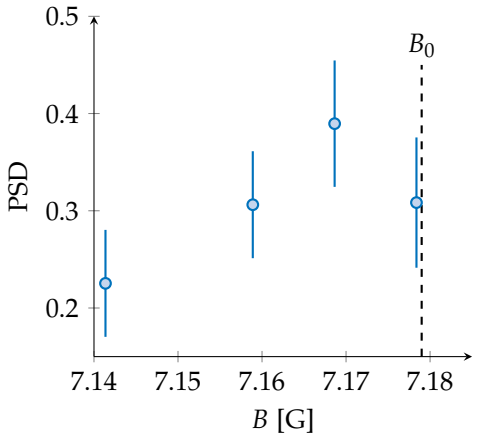

Figure 4.16 *– Achieved PSD at the end of the evaporation ramp for different applied magnetic fields close to a Feshbach resonance. The dashed line shows the resonance pole position.*

B_z [G]	a [a_0]	N_{final}	T_{final} [nK]
0.487	$\simeq 92$	$1.4(2) \times 10^4$	198(3)
7.141	$\simeq 158$	$1.4(4) \times 10^4$	180(10)
7.159	$\simeq 215$	$1.6(3) \times 10^4$	172(4)
7.168	$\simeq 332$	$1.7(3) \times 10^4$	160(3)
7.178	$\simeq 4098$	1.2×10^4	154(3)

Table 4.2 – *Atom number and temperature that we reach at the end of the evaporation ramp for different scattering length a.*

4.5 Heating in the cODT

The measured evaporation efficiency is lower than the reported values in other groups ($\gamma \simeq 3$ for the Pfau group). Experimentally we observe some heating proportional to the laser power. It is quite difficult to disentangle two competing effects: the technical heating related to the stability of the laser and the cooling due to evaporation. We proceed as follows to estimate the heating rate:

- we evaporate the sample to a ratio r_{evap} then we re-compress the trap to a ratio r_{comp} in order to avoid plain evaporation.
- we hold the sample at r_{comp} and we measure the temperature increase over time.
- for each value of r_{comp} we extract the heating rates obtained with different values of r_{evap} and we extrapolate to $r_{\text{evap}} = 0$.

Fig. 4.17 shows an example of the atom number and temperature evolution over time for $r_{\text{evap}} = \{0.05, 0.125, 0.25, 0.5\}$ (brown, red, blue and orange respectively) and $r_{\text{comp}} = 1$. The extracted heating rate as a function of the compression ratio ($P_{\text{final}} = r_{\text{comp}} P_{\text{initial}}$) are presented in Fig. 4.18. We observe a linear increase of the heating rate as a function of r_{comp}, reaching a maximum value of 600 nK/s at full power. At the beginning of the evaporation ramp the technical heating can be neglected as the initial temperature is relatively high. However, the sample is more sensitive to this heating at the end of the evaporation ($\dot{Q} \simeq 40$ nK/s at $r_{\text{comp}} = 0.06$) where the reached temperature is on the order of 100 nK.

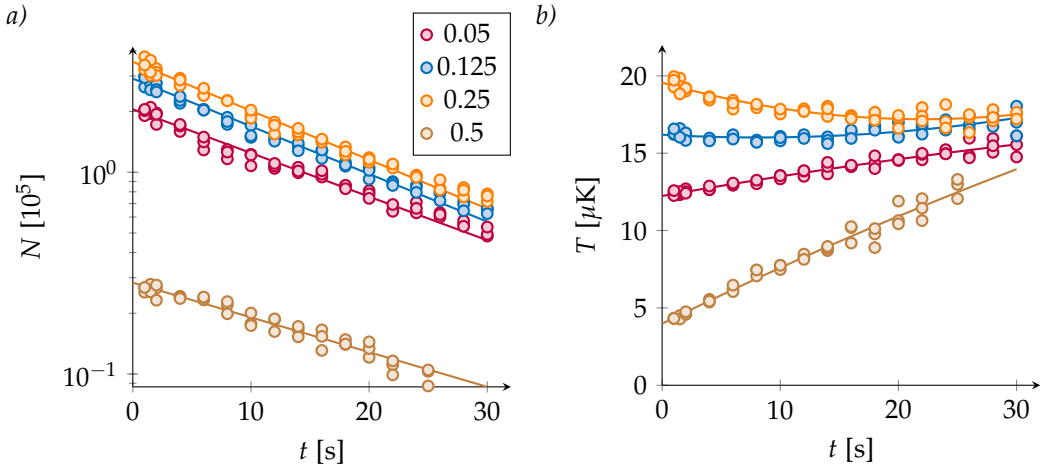

Figure 4.17 *– Evolution of the atom number (a) and temperature (b) as a function of the holding time for* $r_{evap} = \{0.05, 0.125, 0.25, 0.5\}$ *(from bottom to top) and* $r_{comp} = 1$ *(cf. text).*

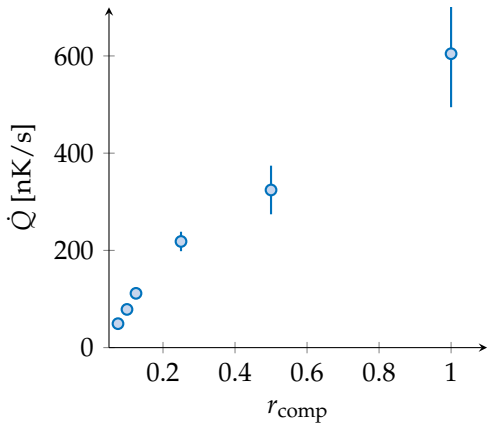

Figure 4.18 *– Extracted heating rate in the cODT as a function of the laser power* ($P_{final} = r_{comp} P_{initial}$).

To summarize, we studied the evaporative cooling process under different experimental conditions. The maximum achieved PSD is on the order of 0.5, corresponding to a gain of a factor 300 with respect to the cloud arriving in the science cell. We need to gain another factor of 5 to cross the BEC transition. Different parameters are limiting the PSD at the end of the evaporation ramp, from which we can name the initial low atom number in the cODT (we are able to reach temperatures on the order of 30 nK but with a low atom number not allowing the formation of a BEC). Secondly, we saw that the technical heating cannot be neglected at the end of the evaporation ramp and can prevent the formation of a BEC.

In order to solve these problems, we made some updates on the experimental setup:

- we exchanged one arm of the cODT (the 5 W laser) with a 50 W laser beam, allowing to increase the initial atom number in the cODT.
- we implemented a scheme allowing to artificially enlarge the beam size by modulating its position to enhance the cODT loading efficiency.
- we implemented a Doppler cooling scheme in the ODT to increase the initial PSD.

Chapter 5

Manipulating the atomic spin with light

Ultracold quantum gases provide an interesting platform for studying complex many-body phenomena thanks to the ability to precisely control their different degrees of freedom (both external and internal). There are several theoretical and experimental investigations on tailoring the atomic state using external electric or magnetic fields [128, 129, 59]. In this chapter, I will present a first test of spin-dependent interactions in our system using an off-resonant laser beam working close to the 626 nm transition. We take advantage of the spin-dependent vector and tensor parts of the light-shift operator to tune the splitting between different Zeeman sub-levels of the ground state, which is equivalent to applying an external magnetic field.

5.1 Spin-dependent light-shift

The general expression of the light-shift operator is given by eq. (3.1) (chapter 3). The benefit of working close to the 626 nm transition comes from the fact that we can create a strong spin-light coupling with a reduced heating thanks to the narrow linewidth of this electronic transition. In the following, we will mainly consider a right circularly polarized (σ^-) laser beam. We recall the potential shift and photon scattering rate formulas for this

polarization:

$$\left\langle \hat{V} \right\rangle_{|J,M_J\rangle} = -\frac{I(r)}{2\epsilon_0 c}\left(\alpha_s(\omega) + \alpha_v(\omega)\frac{M_J}{2J} - \alpha_t(\omega)\frac{3M_J^2 - J(J+1)}{2J(2J-1)}\right) \tag{5.1}$$

$$\left\langle \hat{\Gamma}_{\mathrm{sc}} \right\rangle_{|J,M_J\rangle} = \frac{I(r)}{\hbar\epsilon_0 c}\left(\alpha'_s(\omega) + \alpha'_v(\omega)\frac{M_J}{2J} - \alpha'_t(\omega)\frac{3M_J^2 - J(J+1)}{2J(2J-1)}\right) \tag{5.2}$$

For the red transition the scalar, vector and tensor parts of the dynamical polarizability are given by eq. (3.11). One can draw the analogy between the vector and tensor parts of the light shift operator and the linear and quadratic Zeeman shifts, respectively.
The Rayleigh heating rate is given by:

$$\dot{Q} = \frac{\hbar^2 k^2}{2m}\left\langle \hat{\Gamma}_{\mathrm{sc}} \right\rangle_{|J,M_J\rangle}. \tag{5.3}$$

As an example, we plot in Fig. 5.1 the variation of the ground state energy shift and the corresponding Rayleigh heating rate as a function of the laser beam wavelength. We calculate these quantities for a focused gaussian beam, circularly polarized σ^-, with $w_x = 60$ μm and $w_y = 30$ μm being the horizontal and vertical waists respectively and a total power of 1 W (typical values that we use experimentally). The dashed line sets the resonance position. We see that the heating rate becomes negligible for large detunings while the energy shift remains significant since the former scales as $1/\Delta^2$ and the latter scales as $1/\Delta$ (Δ is the laser detuning with respect to the atomic resonance).

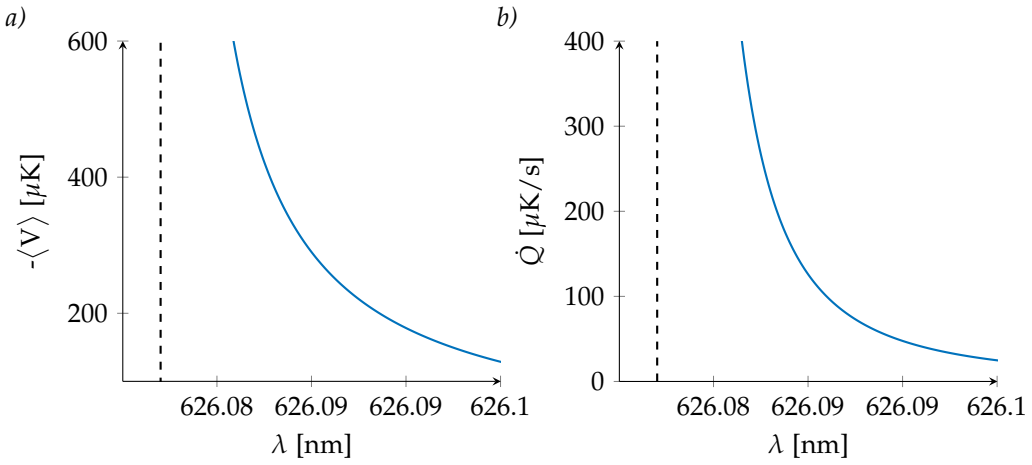

***Figure 5.1** – a) Variation of the ground state energy shift with respect to the laser beam wavelength. b) Variation of the Rayleigh heating rate as a function of the laser beam wavelength. The simulation is done for a laser power $P = 1$ W. The dashed line denotes the atomic resonance position.*

Experimentally, we can scan the laser detuning on a range of few hundreds of GHz. Fig. 5.2 shows the energy shift and heating rate for the different Zeeman sub-levels of the $J = 8$ manifold as a function of the laser power (we use the same beam parameters as above). The calculation is done for a detuning $\Delta = -2\pi \times 100$ GHz.

For a laser power of 1 W, the potential shift seen by the atoms in the ground state $|J = 8, M_J = -8\rangle$ is equivalent to the shift induced by an external magnetic field with $B \simeq 400$ mG. Moreover, a σ^- polarization tends to reduce the energy of the ground state for an increasing laser power (high-field seeker state) while a σ^+ polarization has an opposite behaviour. This is due to the sign of the vector term; for $M_J = -8$ this contribution is negative for a σ^- polarization and positive for σ^+. Finally, we see that the Rayleigh heating rate is quite small (to be rigorous one should take into account the heating induced by dipolar relaxation, *c.f.* chapter 3)

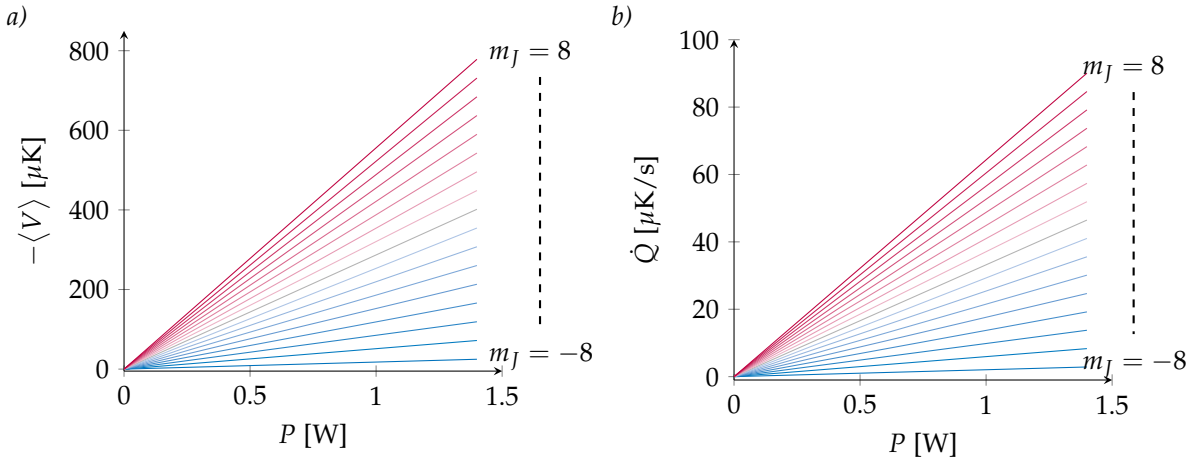

***Figure 5.2** – a) Calculated potential shift as a function of the laser power for the 17 Zeeman sub-levels of the $J = 8$ manifold. b) The corresponding Rayleigh heating rate as a function of the laser power. The detuning is set to $\Delta = -2\pi \times 100$ GHz.*

5.2 Calibration of the coupling strength

We calibrated the coupling strength using a Rabi oscillation experiment. We apply a focused red laser beam, detuned by $\Delta = -2\pi \times 3$ GHz, on the atomic cloud for variable durations. We have initially a spin-polarized sample in the absolute ground state at a temperature $T \simeq 2$ μK. We probe the populations of the different Zeeman sub-levels thanks to a projective measurement along the vertical direction with a Stern-Gerlach

experiment. We define the magnetization as:

$$m_z = \langle \hat{J}_z \rangle \tag{5.4}$$

Fig. 5.3 gives an example of the evolution of the magnetization over time. The observed

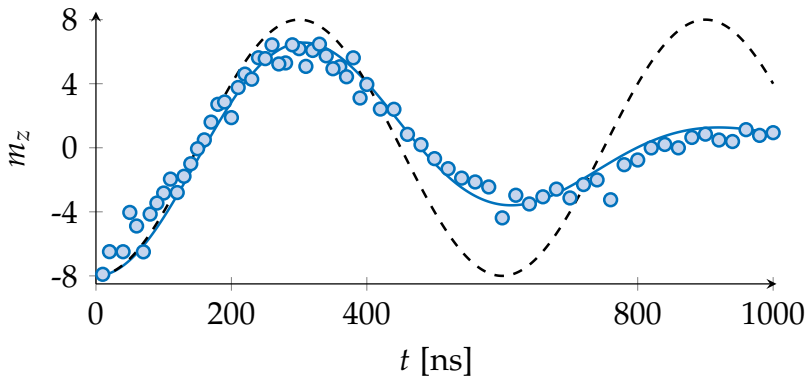

Figure 5.3 *– Evolution of the magnetization as a function of the applied laser pulse duration. The measurement was performed with a detuning $\Delta = -2\pi \times 3$ GHz and a power $P \simeq 0.2$ W. The dashed line corresponds to expected evolution of the spin state when not including the non-linear term $\hat{J}_y^2/306$ of eq. (5.5). The solid line is a fit to the experimental data (see text for the used expression).*

damping of the oscillation can be understood when taking into consideration effects from the non-linear term $\hat{J}_y^2$. In fact, eq. (3.1) can be simplified by projecting the light polarization vector along the eigen-axis of the polarization ellipse. For a circular polarization along the axis $\frac{\hat{\mathbf{z}}-i\hat{\mathbf{x}}}{\sqrt{2}}$, one gets:

$$\hat{V} = V_0 \left(\frac{1}{17}\hat{\mathbb{1}} + \frac{19}{306}\hat{J}_y + \frac{1}{306}\hat{J}_y^2 \right) \tag{5.5}$$

where V_0 is defined as:

$$V_0 = \frac{3\pi c^2 \Gamma}{2\omega_0^3} \frac{I(r)}{\Delta} \tag{5.6}$$

with Γ and ω_0 the linewidth and the resonance frequency of the atomic level, respectively; I is the intensity of the laser beam and Δ its detuning.

Let us consider a sample initially spin-polarized in the absolute ground state $|\ J =$

8, $M_J = -8\rangle_z$. In the y basis, this state can be written as:

$$|J, M_J = -J\rangle = \frac{1}{2^J} \sum_{m=-J}^{J} (-1)^m \sqrt{\binom{2J}{J+m}} |m\rangle_y \tag{5.7}$$

If we consider only the quadratic term (it is the only term responsible for the variation of the spin projection M_J, hence the variation of the magnetization), the evolution of the spin state can then be expressed as:

$$|\psi(t)\rangle = \frac{1}{2^J} \sum_{m=-J}^{J} (-1)^m \sqrt{\binom{2J}{J+m}} e^{-im^2 \frac{\omega_c}{19} t} |m\rangle_y \tag{5.8}$$

where we define the Rabi frequency ω_c as $\hbar\omega_c = \frac{19}{306} V_0$. This non-linear coupling leads to a relative dephasing between the different $m^2\omega_c$ terms. We can then show that the evolution of the magnetization can be obtained analytically and has the following form [130]:

$$m_z(t) = -J \cos(\omega_c t) \left[\cos(\frac{\omega_c t}{19})\right]^{2J-1} \tag{5.9}$$

The dashed line in Fig. 5.3 corresponds to the theoretical expected oscillation without including the non-linear term. The solid line is a fit to the data using eq.(5.9) with ω_c being a free parameter.

Few remarks can be made at this point:

- the simple model described by eq. (5.5) does not account for Zeeman shift due to external magnetic field (for these calibration measurement, we use a vertical field with $B \simeq 20$ mG to set the quantization axis). This can explain the observed mismatch between experimental data and the theoretical expectations (for the example shown in Fig.5.3, we measure a frequency $\omega_c = 2\pi \times 1.56(14)$ MHz and the expected value is $\omega_c = 2\pi \times 3.3$ MHz). Also, one needs to take into account experimental imperfections like magnetic field fluctuations or coupling inhomogeneities due to the comparable sizes of the atomic cloud and the red laser beam.
- The dynamics induced by the quadratic term only is quite interesting to study. One expect to see a collapse of the magnetization caused by the dephasing explained

above, but we also expect to witness a revival of m_z at specific times (the evolution is periodic and at half of the period the magnetization is flipped, *i.e.* only the state $|J = 8, M_J = +8\rangle$ is populated). This coupling can be used to create non-classical states obtained by coherent superposition of the states $|J = 8, M_J = -8\rangle$ and $|J = 8, M_J = 8\rangle$. Experimentally, it is possible to realize such coupling using a linear polarization of the light field perpendicular to the quantization axis. In this case the vector contribution to the light-shift operator vanishes.

Finally, we repeat the Rabi oscillation measurements for different laser powers. The extracted coupling frequencies from the fit are presented in Fig. 5.4. We measure a frequency shift of 15.39(19) MHz/W, to be compared with the expected value: $\delta\omega = 2\pi \times 16.8$ MHz/W.

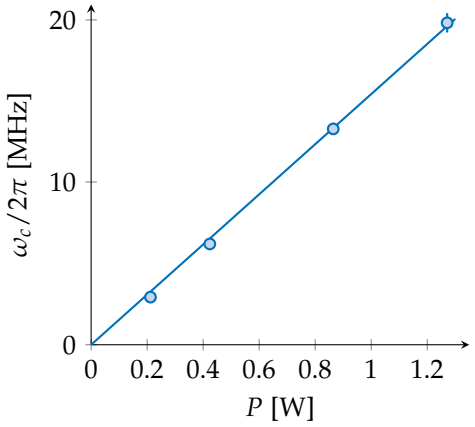

***Figure 5.4** – Measured Rabi frequencies as a function of the laser power for a fixed detuning $\Delta = -2\pi \times 3$ GHz.*

5.3 Effective magnetic field

In this section, the detuning is set to $\Delta = -2\pi \times 100$ GHz to minimize incoherent scattering. The presence of a laser beam can be seen as an effective magnetic field. We observe a shift in a Feshbach resonance position induced by light. Fig. 5.5 compares the resonance pole in the absence of the red beam (black curve) with its position when we apply the laser beam. The blue and red curves correspond to a σ^- and σ^+ polarizations, respectively. This measurement was done with a laser power $P = 0.38$ W.

Two points to be noticed here: first we observe that the resonance pole is shifted to a higher (lower) field for a σ^- (σ^+) polarization; this behaviour is expected as the splitting between two successive Zeeman sub-levels is increased (decreased) in the presence of

laser with a σ^- (σ^+) polarization, hence it is necessary to rise (lower) the magnetic field in order to compensate for this shift and fulfil the resonance condition. Secondly, we notice a broadening of the atom loss resonance. In fact, one should take into consideration losses due to dipolar relaxation that are enhanced close to a Feshbach resonance and incoherent light scattering. Furthermore, we observe that the broadening is larger for a σ^+ polarization, which is not surprising as we expect to have a stronger heating rate for this polarization (*cf.* chapter 3).

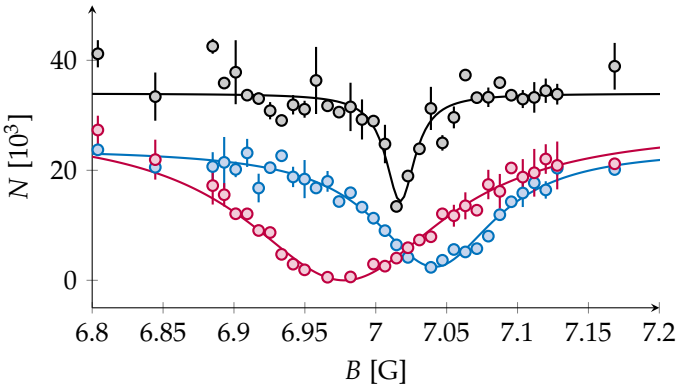

Figure 5.5 *– Position shift of the Feshbach resonance pole under the effect of the light-shift operator. We compare the measured atom loss spectrum in the absence of the laser field (black) with the ones in the presence of a light field which has a circular polarization σ^- (blue) and σ^+ (red). For this experiment the laser detuning is set to $\Delta = -2\pi \times 100$ GHz and the power to $P = 0.38$ W. We measure a position shift of $\delta B \simeq \pm 32$ mG.*

We performed a second set of measurements to verify that the resonance pole is linearly shifted with the applied laser power. For these experiments, the polarization is fixed to σ^-. Results are shown in Fig. 5.6. We observe indeed a linear dependence as a function of the light power with a fitted slope, b_{exp} equal to 51(5) mG/W. We expect to a have a larger shift on the order of 82 mG/W from our calibration. A possible origin of this disagreement can come from the uncertainty that we have on the resonance position caused by the broadening of the resonance peak.

Finally we use the above calibrations to choose the experimental parameters allowing us to induce the Feshbach resonance by scanning the light intensity rather than the magnetic field. We fix the value of the external field to $B = 7.031(4)$ G and we scan the red beam power up to 1.42 W (*c.f.* Fig. 5.7). As it was mentioned above, the presence of the red light results in the promotion of a fraction of the atomic population to higher spin states due to Raman scattering. This mixing of the population leads to atom losses

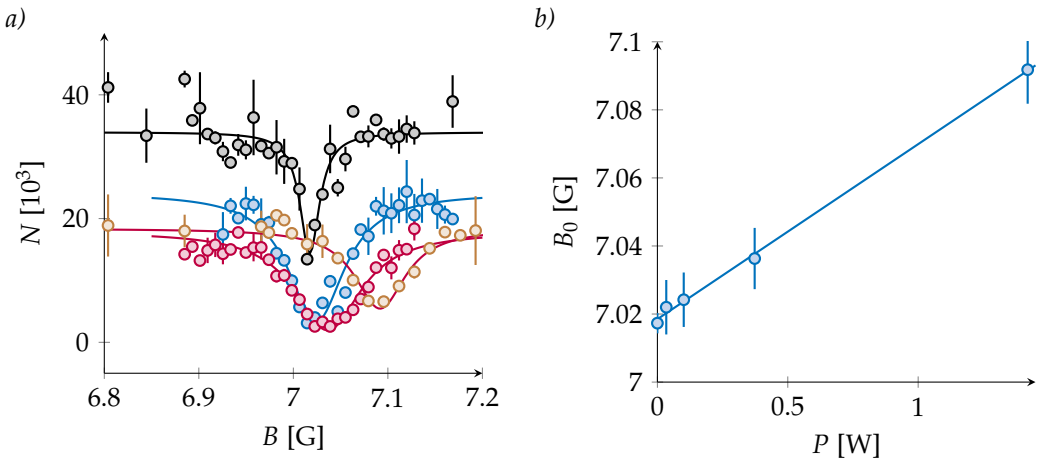

Figure 5.6 – *Position shift of the Feshbach resonance pole B_0 as a function of the laser power. The laser is circularly polarized σ^- and has a detuning $\Delta = -2\pi \times 100$ GHz. We observe a linear shift with the laser power. The fitted slope is $b = 51(5)$ mG/W.*

through dipolar relaxation, and we thus rescale the measured atom number with respect to a measurement performed far from the Feshbach resonance position (square data in Fig. 5.7).

The characterization of this resonance (*i.e.* a precise determination of its pole position and its width) is quite challenging as multiple effects are entangled. On the one hand, the temperature increase, due to the energy released after a dipolar relaxation process, can modify the collision dynamics by allowing contributions from higher-order partial waves (*c.f.* chapter 4, section 3). On the other hand, the determination of the resonance width, defined as the magnetic field difference between the value of B_0 that maximizes 3-body losses and the value of B_c that maximizes the temperature, is not necessarily correct since different processes take part during the collisional dynamics.

To conclude, the experiments exposed in this chapter are a proof of principle study on the possibility of creating a light-induced spin-dependent coupling. As we have seen in the previous chapter, it is possible to tune the interactions by means of a Feshbach resonance. The obtained results pave the way for selective applied interactions. For example, one can imagine to have a tightly focused laser beam on a BEC such that one can tune the scattering length locally [131, 132]. Also, since the coupling is generated by light, it is possible to turn it on and off much faster that what can be done with a magnetic field (we can generate experimentally light pulses of few tens of nano-seconds). As a consequence, it is possible to have a fast modulation of the scattering length in the sample [133]. Nevertheless more theoretical and experimental investigations are required

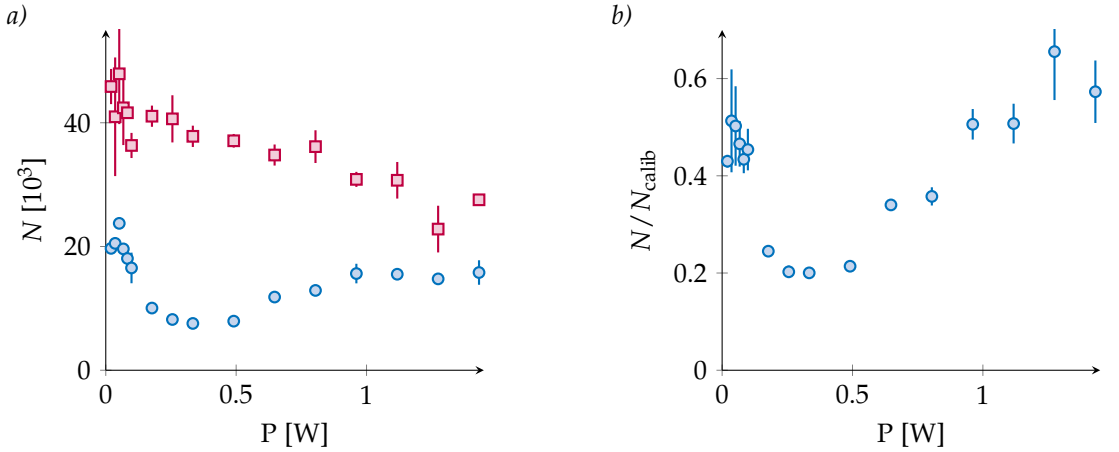

Figure 5.7 *– Light induced Feshbach resonance: the measured atom loss spectrum as a function of the applied laser power. We use a measurement of the atom number as a function of the laser power far from the Feshbach resonance (red square) to rescale the atom number around the resonance (blue circle).*

to fully understand the dynamics close to the Feshbach resonance.

Conclusion and perspectives

Summary

In the framework of this thesis, I was interested in the investigation and characterization of a variety of interactions between highly magnetic Dysprosium atoms. The richness of the scope of applications offered by this atomic specie arises from its intrinsic physical properties, mainly the large permanent magnetic dipole moment and a multitude of narrow-linewidth optical transitions. I showed all along this manuscript that these features have a strong influence on the dynamics of the atomic cloud starting from the early stage of the experimental sequence, the MOT. I explained how the competition between the radiative force and gravity can lead to a spontaneous polarisation of the atomic sample. I was interested also in light-assisted collisions in the MOT within the large $J = 8$ manifold, and its dependency on experimental parameters such as the laser detuning with respect to the optical transition resonance and the light intensity and I showed that we reach a minimal two-body loss rate in the spin-polarised regime.
The anisotropy of interactions in a Dy gas comes forth at different levels through the dynamical polarizability, the dipole-dipole interaction and the anisotropic Van der Waals interaction. A detailed study on different aspects of this anisotropy was realized.
After the MOT stage, the atoms are loaded in a far detuned optical beam. In contrast with alkali species, for which such a trapping is independent of the internal atomic state, the anisotropy of Dy atomic polarizability affects drastically the trapping and heating in optical dipole traps. An experimental investigation of the latter as a function of the light polarisation was performed, both in the presence of a far and close detuned optical beams. As for the dipole-dipole interaction, its effects were highlighted through the observation of atom losses in an optical dipole trap, mediated by the dipolar relaxation. The anisotropy of the C_6 dispersion interaction coefficient, along with the large spin of Dy,

have a substantial impact on the Feshbach spectrum. I gave an overview on the specificity of this spectrum (large resonance density, tight dependence on the temperature, *etc*) and explained its physical origin. A focus was set on a relatively broad resonance around 7 G that we use to tune the interaction between atoms during the evaporative cooling process. This latter was investigated in detail as well. I compared the evaporation efficiency under different experimental conditions with a particular attention given to the effects of gravity and the elastic scattering length. The technical limitations that prevent us from crossing the condensation threshold were discussed as well. In the last section of this manuscript, I developed a study exploiting the spin-dependent character of the atomic polarizability in order to create an effective magnetic field. The effects of the latter were revealed by recovering a Feshbach resonance by scanning the intensity of the optical field instead of a magnetic field.

Perspectives

The theoretical prediction of topological insulators [134, 135], followed by their experimental realization, both in a 2D [136] and 3D geometry [137], revived the interest in studying systems with non-trivial topological order. A topological insulator is a system with a bulk band gap, similar to an ordinary insulator, but exhibits conducting states on its edges (in 2D) or surface (in 3D). Due to their topological character, these states are robust against disorder or perturbations. The seek of novel states of matter, emergent from unconventional topological phases, is motivated, from one side, by the fundamental interest in understanding such systems, and from the other side, by the potential that they offer from a quantum technology perspective (the so-called topological quantum computation and quantum memory). The implementation of these systems with ultracold atoms should benefit from the developed techniques in this field which provide high degrees of control and tunability of the different parameters of the studied subject. For our future projects, we are interested in the realization of a topological superfluid in a degenerate Fermi gas of the isotope ^{161}Dy. I will give in the following a brief introduction of this unconventional superfluid and present different experimental schemes which could allow one to observe it.

The Kitaev model

In 1937, Landau developed a theory of phase transitions in attempt to describe superconductivity [138]. This theory can be used to make a classification of physical systems in different phases. These latters are charcterized by an order parameter, a physical quantity that can be used to probe a phase transition. If the transition occurs between two phases with different topology, some gapless modes emerge, which are topologically protected, (more details on the classification of topological systems can be found in refs. [139, 140]).

In 2001, Kitaev introduced a toy model describing the physics of a 1D spinless p-wave superconducting (superfluid) chain [141]. Such a system carries gapless modes at its boundaries that have quite interesting properties. They can be seen as one fermion splitted between the edges of the 1D chain. These exotic modes are called *Majorana fermions*, in analogy to those predicted in 1937 by Ettore Majorana, which have quite intriguing properties as they are identical to their own antiparticle, have a non-Abelian statistics and a non-locality character. These features make them an appealing candidate for quantum qubit implementation as they are protected against decoherence.

Let us consider a chain with $N \gg 1$ sites and each site can be either empty or occupied by a particle (with a fixed spin direction). The hamiltonian describing this system can be expressed in the following way:

$$H_{\text{Kitaev}} = \sum_i \underbrace{-\mu\left(\hat{c}_i^\dagger \hat{c}_i - 1/2\right)}_{h_1} \underbrace{-\omega\left(\hat{c}_i^\dagger \hat{c}_{i+1} + h.c\right)}_{h_2} \underbrace{+\Delta\left(\hat{c}_i^\dagger \hat{c}_{i+1}^\dagger + h.c\right)}_{h_3} \tag{5.10}$$

where $\hat{c}_i^\dagger$ ($\hat{c}_i$) is the creation (annihilation) operator of a fermion in the site i. This hamiltonian comprises three different contributions:

- h_1: this term describes the on-site energy, with μ being the chemical potential,
- h_2: it consists in a hopping term between two neighbouring sites, with a tunneling amplitude ω,
- h_3: this last term describes the induced superfluid gap of a value Δ.

Kitaev showed that a key ingredient for the emergence of a non-trivial topological phase in this quantum wire is to have a superconductor with a p-wave pairing (in contrast with the usual isotropic s-wave pairing in conventional superconductors). This toy model is very interesting as its formulation is quite simple, although it sets forth quite intriguing

phenomena.

BCS pairing in a single-component dipolar Fermi gas

The BCS theory [142] describes the particles of a superconductor (or superfluid) as weakly bounded pairs. At low temperature in a two-component Fermi gas, this pairing has an *s*-wave symmetry. In a single-component Fermi gas, such pairing cannot occur as the interaction through the short-range *s*-wave channel (or any angular momentum with an even value) is forbidden by the Pauli principle, and for higher (odd) angular momenta, the interaction cross-section vanishes when the wavevector $k \to 0$. Nevertheless, particles pairing in dipolar gases, at sufficiently low temperatures, can take place due to the partial attractiveness of the DDI [143]. One can convince oneself by writing the angular contribution of the DDI:

$$\langle L = 1, M_L = 0 | 1 - 3\cos^2\theta | L = 1, M_L = 0 \rangle = -\frac{4\pi}{5}, \tag{5.11}$$

therefore leading to an attractive interaction. For projections of the angular momentum on the quantization axis, $M_L = \pm 1$, the DDI contribution has a positive sign (repulsive interaction). We neglect higher order angular momenta contributions since at low temperature the *p*-wave contribution is the dominant one.
Here one may wonder, is it possible to observe a topological superfluid in a dipolar Fermi gas with realistic experimental parameters? What are the important quantities to consider [144]?

The critical temperature of the superfluid phase transition

A phase transition between a normal Fermi gas and a superfluid phase occurs at a critical temperature T_c determined by the system parameters (density, geometry, interactions, *etc*). Usually, T_c is much lower than the Fermi temperature T_F that sets the boundary to the degenerate Fermi gas phase transition. The critical temperature T_c was derived for a homogeneous[a] singlet-component dipolar Fermi gas in the dilute regime [144], and it is given by:

$$T_c \approx 1.44\epsilon_F \exp\left[-\frac{\pi\epsilon_F}{12nd^2}\right] \tag{5.12}$$

[a] Corrections due to the trapping potential were calculated also in ref. [143].

with ϵ_F the Fermi energy ($\epsilon_F = \mu$, the chemical potential, for a degenerate Fermi gas), n the atomic density and d the dipole moment of the particle[a]. In theory, it is possible to create a p-wave superfluid if the condition $T < T_c$ is fulfilled. In practice, it is difficult to achieve this condition as the Fermi energy is usually much larger than the dipolar interaction energy which results in a very small critical temperature T_c, difficult to attain with available cooling techniques. For simplicity, we re-write eq. (5.12) as follows:

$$T_c \approx 1.44 T_F \exp\left[-\frac{\pi\hbar}{2\sqrt{2mk_{\mathrm{B}}T_f}a_d}\right] \tag{5.13}$$

where we define the effective scattering length as $a_d = \frac{2md^2}{\pi^2\hbar^2}$. The implementation of this scheme is well adopted for ultracold polar molecules. The recent advances in this field [145, 146] are very promising as these systems possess dipolar moments larger than those of highly magnetic atoms by one or two orders of magnitude. For example, the fermionic polar molecule ^{40}K^{87}Rb has been cooled down to $T/T_F = 1.4$ [145]. This molecule has a dipole moment of $d = 0.57$ D which correspond to an effective scattering length $D \simeq 14$ nm. The actual limitation comes from technical difficulties to reach dense samples due to the complexity of the quantum ultracold chemistry.

On the other hand, highly magnetic atoms such as Dy or Er, were successfully brought to degeneracy. However, one needs to reach atomic densities on the order of 10^{15} cm^{-3} to be able to observe the superfluid transition. For example, if we consider the fermionic isotope ^{161}Dy, we obtain a critical temperature $T_c = 100$ nK for a Fermi temperature $T_F \simeq 9$ μK, or equivalently an atomic density $n \simeq 8 \times 10^{15}$ cm^{-3} that are almost impossible to acheive experimentally (to be compared with the experimental achieved Fermi temperature $T_F = 300$ nK for this isotope [63]).

Another direction that can be explored to create a topological superfluid is to work in the vicinity of a p-wave Feshbach resonance. The observation of these types of resonance in fermionic gases of ^{6}Li [147] and ^{40}K [148] paved the way for investigating the p-wave pairing in such systems. It was shown experimentally that it is possible to create Feshbach molecules with resonances having a p-wave symmetry [149, 150], though their lifetime was very short due to inelastic processes, mainly dipolar relaxation. Nevertheless, longer lifetimes are expected to be achievable in a system for which a p-wave resonance occurs

[a] For particles with a magnetic moment μ, d can be linked to this latter through $d = \sqrt{\frac{\mu_0\mu^2}{4\pi}}$.

at low magnetic field where dipolar relaxation rates is quite suppressed or in the lowest Zeeman sublevel where dipolar relaxation is prohibited. Hence, Dy presents a great to potential to feature such resonances. As we saw in chapter 4, Dy has a rich Feshbach spectrum and resonances exist even at low field. It is not impossible that some resonances have a p-wave symmetry. Thus further theoretical and experimental investigations are required.

Emergence of a topological superfluid in systems with light dressing of the spin-states

Several theoretical studies propose to use atom-light couplings in order to induce effectively a p-wave superfluid. I will concentrate on the proposal made in ref. [151] and discuss their implementation in a Dy degenerate Fermi gas.
The idea, based on the original proposal by Kitaev, consists in having a trapped 1D fermionic system in the vicinity of a BEC of Feshbach molecules that serves as a reservoir of Cooper pairs. A carefully designed coupling between the two systems can effectively induce the emergence of a superfluid gap in the 1D system with an effective p-wave pairing.

Use of a synthetic spin-orbit coupling

In the past few years, successful experimental realizations of a synthetic spin-orbit coupling (SOC) in both bosonic [128] and fermionic [61, 152, 56] systems by means of Raman coupling, opened the door towards the creation of topological gauge fields. The SOC plays a key role in condensed matter systems as it is responsible for multiple phenomena such as the spin Hall effect. In ultracold atom systems, 2-photon Raman transitions are used to couple an internal atomic state to the momentum of the particle. Fig. 5.8 shows the dispersion relation (right hand side) in the presence of the Raman coupling between two spin states denoted $|\uparrow\rangle$ and $|\downarrow\rangle$ (left hand side). For weak coupling strength, the dispersion relation is the one of a free particle of a momentum $p \pm k$ with k being the wavevector of the Raman beams and p the particle momentum (plotted in dashed line). Increasing the coupling strength results in an avoided crossing at $p = 0$ and a gap opens. One can see that the obtained lowest band presents a smooth transition between the two spin states. More details on SOC can be found in ref. [153]. Zoller *et al.* propose to use this coupling to induce a superfluid gap in the 1D fermionic

quantum wire [151].

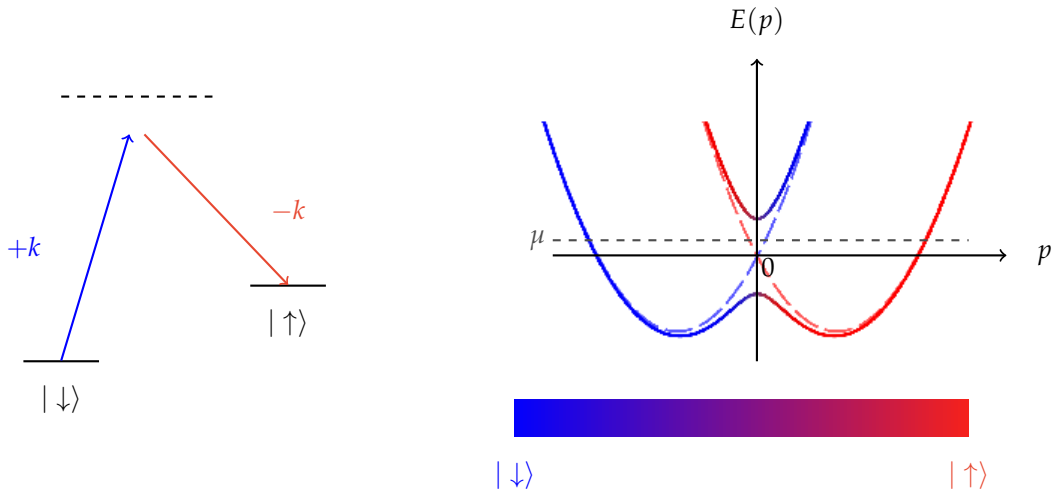

Figure 5.8 *– Left hand side: schematic of the Raman coupling between two spin states $|\uparrow\rangle$ and $|\downarrow\rangle$. Right hand side: The dispersion relation in the presence of the SOC that results in a gap opening. The dashed line corresponds to the dispersion relation of free particles, for a weak coupling.*

To summarize, the needed ingredients for creating a topological superfluid are:

1. a 1D trapped fermionic system,
2. a molecular BEC (s-wave pairing),
3. SOC allowing for spin-momentum locking,
4. and an RF field to drive interactions between fermions in the 1D system and the Feshbach molecules in the BEC.

Experimental realization

The main limitation today preventing the realisation of such a system is the large heating rate accompanying Raman coupling for alkali atoms [152] due to the small fine structure splitting of the P electronic levels compared to the transition linewidth. This heating reduces the lifetime of the system. Instead of using alkali species, lanthanide atoms turn out to be a good candidate for implementing a Raman scheme taking advantage of relatively narrow optical transitions. For example, one can use the transition at $\lambda = 741$ nm for Dy, which is quite isolated from the rest of the electronic spectrum and has a linewidth of $\Gamma/2\pi = 1.78$ kHz. A first experimental realization [56] confirmed that the lifetime is enhanced in a spin-orbit coupled degenerate Fermi gas of ^{161}Dy, which motivates the pursuit of this direction to create a topological superfluid.

To conclude, I showed all along this manuscript that we have a good understanding of our system. The reported studies of the Feshbach spectrum and the atom-light interaction pave the way towards the implementation of the discussed above proposal.

Appendix A

Design of the transport acceleration profile

The optical transport of atoms from the MOT chamber to the science cell was studied in chapter 2. The spatial displacement of the optical beam focal point is done by means of a motorized translation stage. The main technical features of the latter are:

- **Stage model:** ANT 130-160-L-PLUS-25DU-MP
- **Maximum travel distance:** 160 mm
- **Maximum speed:** 200 mm/s
- **Maximum acceleration:** 10 m/s^2

As it was discussed before, the oscillation of the atomic cloud center of mass at the end of the movement is reduced for some specific transport durations. However, an arbitrary choice of this time is not possible due to the translation stage maximum speed. This limitation can be overcome by changing the acceleration profile. Fig. A.1 shows few examples of acceleration and velocity profiles that can be realized with our translation stage. The large acceleration and deceleration phases permits to reduce the total duration of the transport. We calculated the resulting velocity of a particle trapped in a gaussian optical beam (we use the parameters of the transport beam) to which we apply the acceleration profiles presented in Fig. A.1. Results are plotted in Fig. A.2. We see that the particle gains kinetic energy when the acceleration is increased, which is in agreement with the experimental observation reported in chapter2.

We measured the temperature increase as a function of the transport duration (Fig. A.3). We observe a drop of the temperature for $T_{\text{Transport}}$ between 0.8 s and 1 s that can be

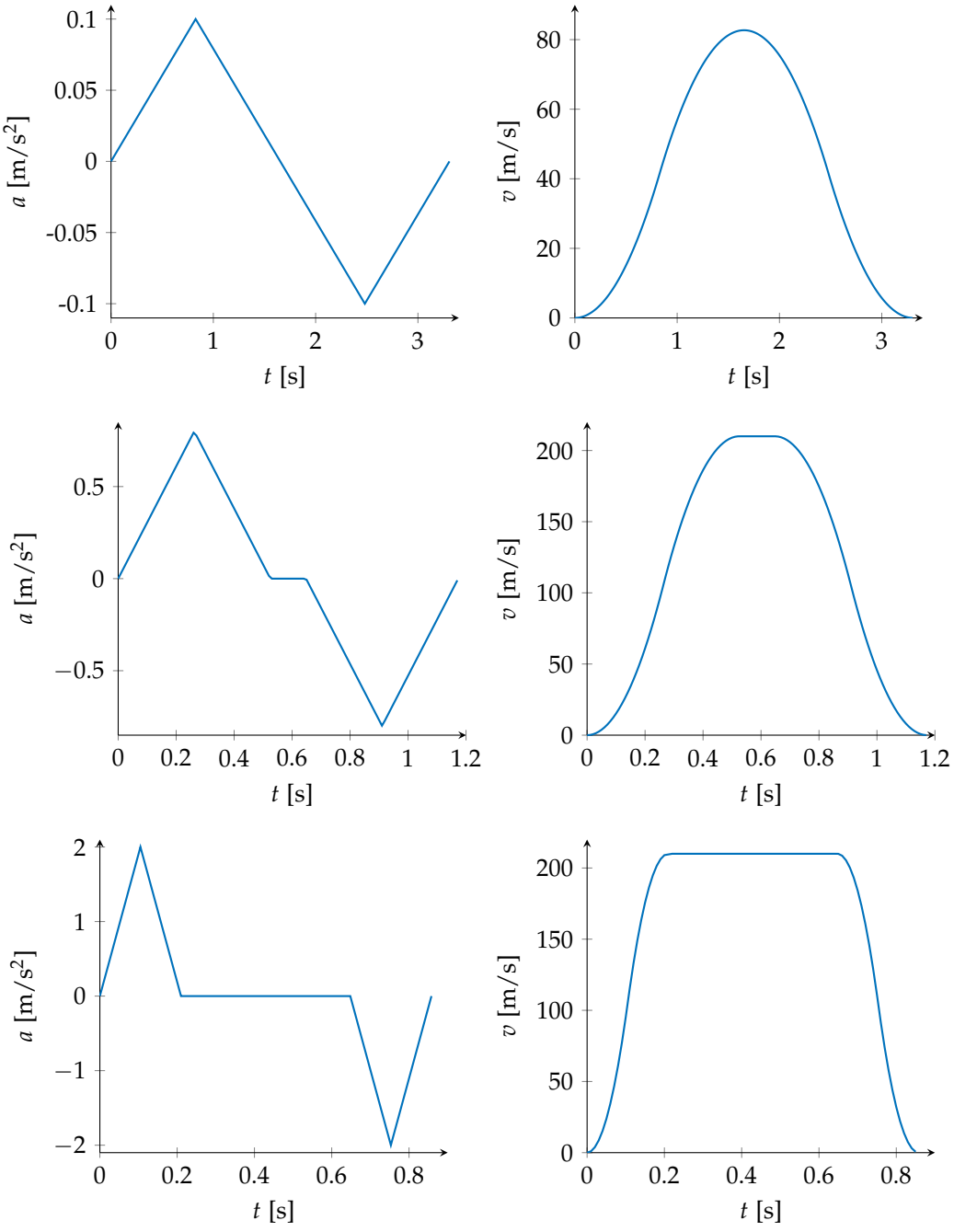

Figure A.1 *– Example of different acceleration profiles applied to the translation stage (left hand side) and the corresponding velocity profiles (right hand side).*

explained by an evaporation driven by the tilting of the trap due to the large acceleration (*cf.* chapter 2). For even shorter durations, the observed heating results from the competition between the evaporation process and the energy gain due to the large centre of mass oscillation amplitudes.

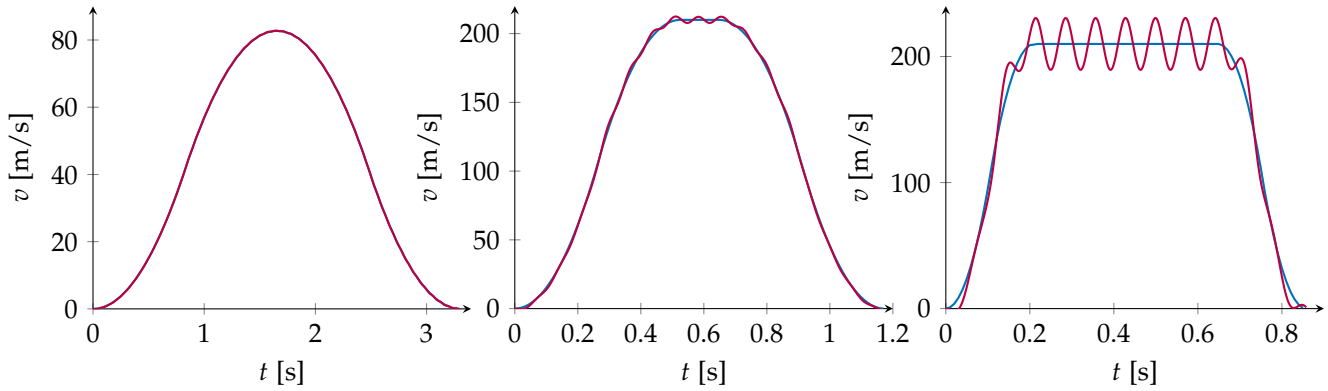

Figure A.2 *– Calculated velocity profiles of a particle trapped in the transport dipole trap during the displacement (purple) for the acceleration profiles shown in Fig. A.1 (to be compared with the velocity profile of the translation stage (blue)).*

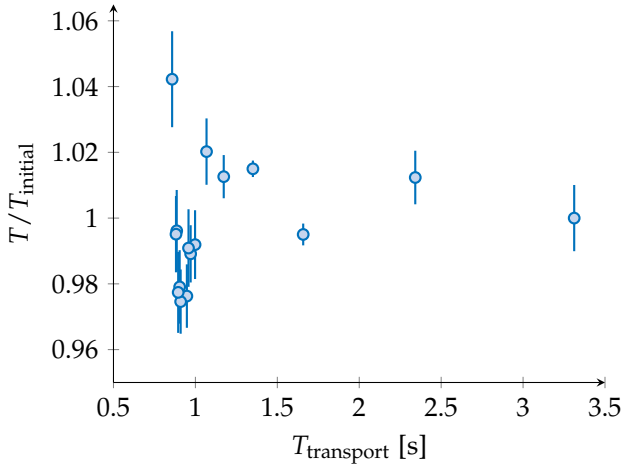

Figure A.3 *– The temperature of the atomic cloud at the end of the transport normalized to the initial temperature as a function of the transport duration.*

Appendix B

Article: Optical cooling and trapping of highly magnetic atoms: the benefits of a spontaneous spin polarization

OPEN ACCESS
IOP Publishing
Journal of Physics B: Atomic, Molecular and Optical Physics
J. Phys. B: At. Mol. Opt. Phys. **50** (2017) 065005 (12pp)
https://doi.org/10.1088/1361-6455/aa5db5

Optical cooling and trapping of highly magnetic atoms: the benefits of a spontaneous spin polarization

Davide Dreon, Leonid A Sidorenkov, Chayma Bouazza, Wilfried Maineult, Jean Dalibard and Sylvain Nascimbene

Laboratoire Kastler Brossel, Collège de France, CNRS, ENS-PSL Research University, UPMC-Sorbonne Universités, 11 place Marcelin Berthelot, F-75005 Paris, France

E-mail: sylvain.nascimbene@lkb.ens.fr

Received 30 December 2016, revised 23 January 2017
Accepted for publication 2 February 2017
Published 7 March 2017

Abstract

From the study of long-range-interacting systems to the simulation of gauge fields, open-shell lanthanide atoms with their large magnetic moment and narrow optical transitions open novel directions in the field of ultracold quantum gases. As for other atomic species, the magneto-optical trap (MOT) is the working horse of experiments but its operation is challenging, due to the large electronic spin of the atoms. Here we present an experimental study of narrow-line dysprosium MOTs. We show that the combination of radiation pressure and gravitational forces leads to a spontaneous polarization of the electronic spin. The spin composition is measured using a Stern–Gerlach separation of spin levels, revealing that the gas becomes almost fully spin-polarized for large laser frequency detunings. In this regime, we reach the optimal operation of the MOT, with samples of typically 3×10^8 atoms at a temperature of 15 μK. The spin polarization reduces the complexity of the radiative cooling description, which allows for a simple model accounting for our measurements. We also measure the rate of density-dependent atom losses, finding good agreement with a model based on light-induced Van der Waals forces. A minimal two-body loss rate $\beta \sim 2 \times 10^{-11}$ cm^3 s^{-1} is reached in the spin-polarized regime. Our results constitute a benchmark for the experimental study of ultracold gases of magnetic lanthanide atoms.

Keywords: laser cooling, ultracold dysprosium, ultracold atoms

(Some figures may appear in colour only in the online journal)

1. Introduction

Open-shell lanthanide atoms bring up new perspectives in the field of ultracold quantum gases, based on their unique physical properties. Their giant magnetic moment allows exploring the behavior of long-range interacting dipolar systems beyond previously accessible regimes [1–7]. The large electronic spin also leads to complex low-energy scattering between atoms, exhibiting chaotic behavior [8, 9]. The atomic spectrum, which includes narrow optical transitions, further permits the efficient production of artificial gauge fields [10–12].

This exciting panorama triggered the implementation of laser cooling techniques for magnetic lanthanide atoms, including dysprosium [13–15], holmium [16, 17], erbium [16, 18–20] and thulium [16, 21]. Among these techniques, magneto-optical trapping using a narrow optical transition (linewidth $\Gamma \sim 2\pi \times 100$ kHz) provides an efficient method to prepare atomic samples of typically 10^8 lanthanide atoms in the 10 μK temperature range [15, 20], in analogy with the trapping of Sr and Yb atoms using the intercombination line [22, 23].

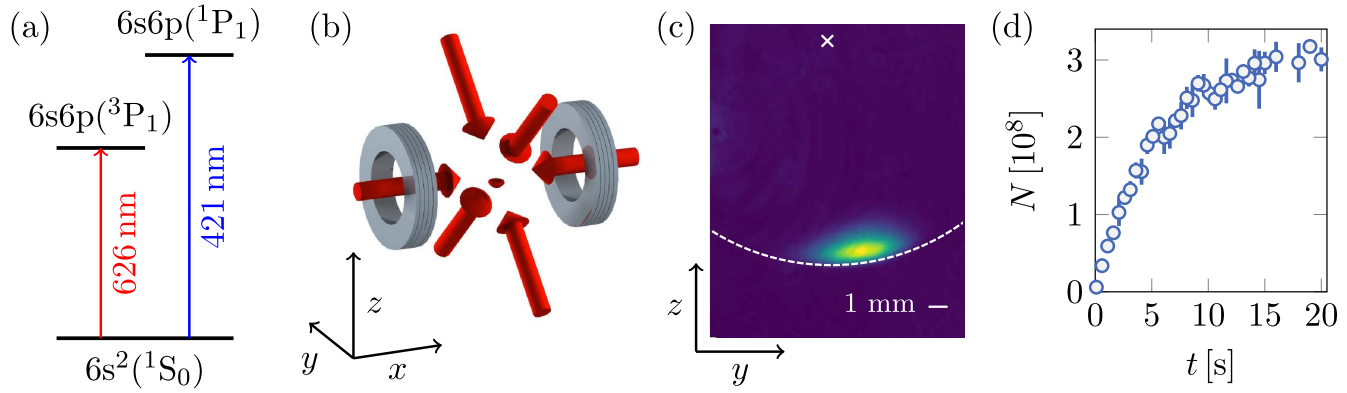

Figure 1. (a) Scheme of the optical transitions involved in our laser cooling setup, coupling the electronic ground state $4f^{10}(^5I_8)6s^2(^1S_0)$ $(J = 8)$ to the excited states $4f^{10}(^5I_8)6s6p(^1P_1)(8,1)_9$ $(J' = 9)$ and $4f^{10}(^5I_8)6s6p(^3P_1)(8,1)_9$ $(J' = 9)$. (b) Scheme of the magneto-optical trap arrangement, with the six MOT beams (red arrows) and the pair of coils in anti-Helmoltz configuration. Gravity is oriented along $-z$. (c) Typical *in situ* absorption image of an atomic sample held in the 'compressed' magneto-optical trap. The cross indicates the location of the quadrupole center. The cloud is shifted by $\sim$1 cm below the zero due to gravity. We attribute the cloud asymmetry with respect to the z axis to the effect of an ambient magnetic field gradient. (d) Atom number N captured in the magneto-optical trap as a function of the loading time t (see text for the MOT parameters).

For two-electron atoms like Ca, Sr and Yb [22–24], the absence of electronic spin simplifies the operation and theoretical understanding of the MOT. On the contrary, the large value of the electron spin for lanthanide atoms greatly complicates the atom dynamics, the modeling of which *a priori* requires accounting for optical pumping effects between numerous spin levels. Previous works on narrow-line MOTs with lanthanide atoms mentioned a spontaneous spin polarization of the atomic sample [1, 2, 19], but its quantitative analysis was not explicitely described.

In this article, we present a study of Dy magneto-optical traps (MOTs) operated on the 626 nm optical transition (linewidth $\Gamma = 2\pi \times 136$ kHz [25]) [15]. We measure the spin populations using a Stern–Gerlach separation of the spin levels. We observe that, for large and negative laser detunings (laser frequency on the red of the optical transition), the atomic sample becomes spin-polarized in the absolute ground state $|J = 8, m_J = -8\rangle$. This spontaneous polarization occurs due to the effect of gravity, which pushes the atoms to a region with a relatively large magnetic field (on the order of 1G), leading to efficient optical pumping [1, 2, 19]. In the spin-polarized regime, the system can be simply described with a two-level atom model, in close relation with previous works on Sr MOTs [26] and narrow-line MOTs of magnetic lanthanides [1, 2, 19].

We show that the spin-polarized regime corresponds to optimal operating parameters for the MOT, leading to samples with up to $N \simeq 3 \times 10^8$ atoms and temperatures down to $T \simeq 15$ μK. This observation is supported by a study of density-dependent atom losses triggered by light-induced Van der Waals interactions between atoms. We observe that minimal loss rates are reached in the spin-polarized regime, as predicted by a simple model of atom dynamics in attractive molecular states.

2. Preparation of magneto-optically trapped dysprosium gases

The electronic states of dysprosium involved in our study are represented in figure 1(a), together with a schematics of the MOT in figure 1(b). An atomic beam is emitted by an effusion cell oven, heated up to 1100 °C. The ^{164}Dy atoms are decelerated in a Zeeman slower, which is built in a spin-flip configuration and operates on the broad optical transition at 421 nm (linewidth $2\pi \times 32$ MHz [27]). The flux of atoms along the Zeeman slower axis is enhanced using transverse Doppler cooling at the entrance of the Zeeman slower, also performed on the 421 nm resonance [28].

The MOT, loaded in the center of a steel chamber, uses a quadrupole magnetic field of gradient $G = 1.71$ G cm^{-1} along the strong horizontal axis x. The MOT beams, oriented as pictured in figure 1(b), operate at a frequency on the red of the optical transition at 626 nm [15], the detuning from resonance being denoted Δ hereafter. This transition connects the electronic ground state $4f^{10}6s^2(^5I_8)$, of angular momentum $J = 8$ and Landé factor $g_J \simeq 1.24$, to the electronic state $4f^{10}(^5I_8)6s6p(^3P_1)(8,1)_9$, of angular momentum $J' = 9$ and Landé factor $g_{J'} \simeq 1.29$. Its linewidth $\Gamma = 2\pi \times 136$ kHz, corresponding to a saturation intensity $I_{\rm sat} = 72$ μW cm^{-2}, allows in principle for Doppler cooling down to the temperature $T_{\rm D} = \hbar\Gamma/(2k_B) \simeq 3.3$ μK. Each MOT beam is prepared with a waist $w \simeq 20$ mm and an intensity $I = 3.7$ mW cm^{-2} on the beam axis, corresponding to a saturation parameter $s \equiv I/I_{\rm sat} \simeq 50$.

The atom loading rate is increased by artificially broadening the MOT beam frequency: the laser frequency is sinusoidally modulated at 135 kHz, over a total frequency range of 6 MHz, and with a mean laser detuning $\Delta = -2\pi \times 4.2$ MHz. From a typical atom loading curve (see figure 1(d)) one obtains a loading rate of $6(1) \times 10^7$ atoms s^{-1} at short times and a maximum atom number $N = 3.1(5) \times 10^8$. The atom number is determined up to a

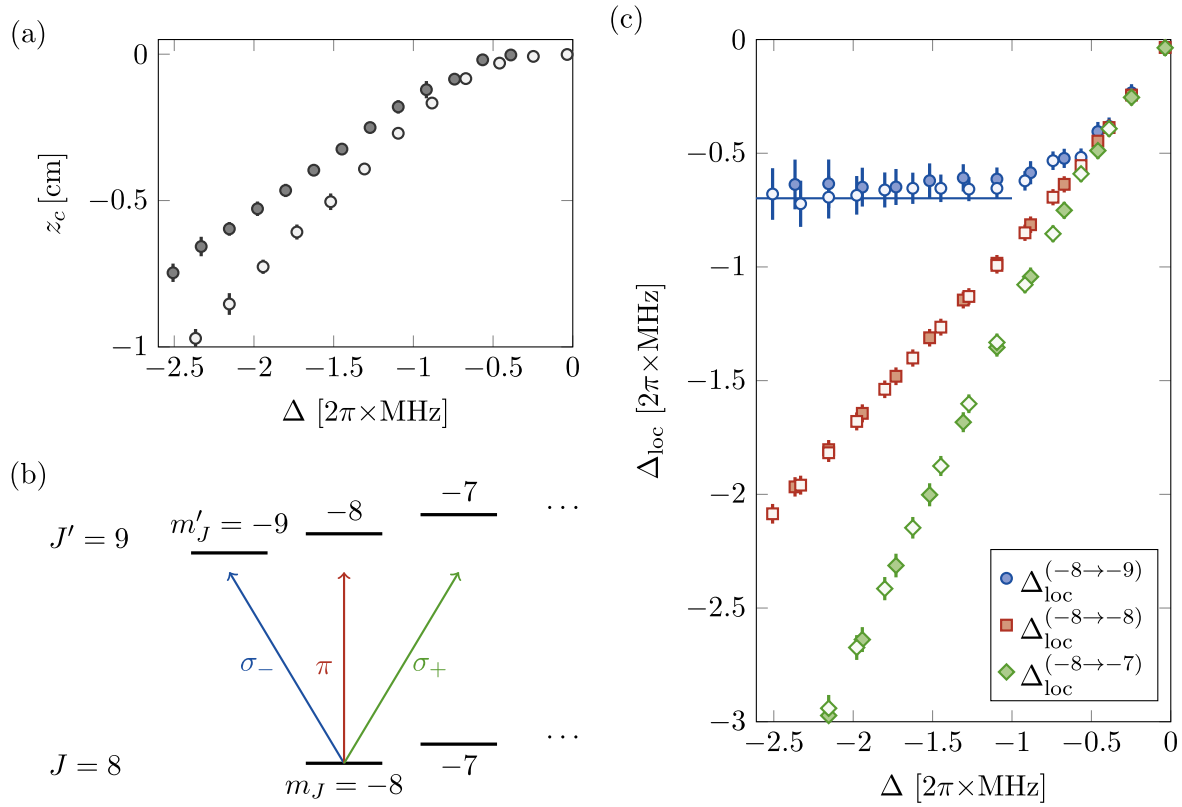

Figure 2. (a) Vertical position z_c of the MOT center of mass as a function of the laser detuning Δ, measured for two values of the magnetic field gradient, $G = 1.71$ G cm^{-1} (open symbols) and $G = 2.26$ G cm^{-1} (filled symbols) and a saturation parameter $s = 0.65$. (b) Scheme of the optical transitions starting from the absolute ground state $|J = 8, m_J = -8\rangle$. As the MOT position deviates from the magnetic field zero position, optical transitions of polarization σ_- become more resonant than π and σ_+ transitions, leading to optical pumping into the absolute ground state. (c) Local detunings for the three optical transitions involving the absolute ground state, inferred from the laser detuning and the Zeeman shifts at the MOT position. We take into account an ambient magnetic field gradient along z, $\delta G = -0.094(2)$ G cm^{-1}, measured independently. The local detuning of the σ_- transition (circles) saturates to a fixed value for large detunings, showing that the MOT position adapts to keep the local detuning fixed. The π and σ_+ transitions (square and diamonds, respectively) do not exhibit this saturation.

20% systematic error using absorption imaging with resonant light on the broad optical transition, taking into account the variation of scattering cross-sections among the spin manifold expected for our imaging setup.

After a loading duration of ∼6 s, we switch off the magnetic field of the Zeeman slower, as well as the slowing laser. We then compress the MOT by ramping down the frequency modulation, followed by decreasing the saturation parameter s and the laser detuning Δ over a total duration of 430 ms. At the same time, the magnetic field gradient is ramped to its final value. For most of the MOT configurations used for this study, we do not observe significant atomic loss during the compression. A typical absorption image of the atomic sample after compression is shown in figure 1(c). The curved shape of the gas and its mean position (about 1 cm below the magnetic field zero) reveal the role of gravity in the magneto-optical trapping [19, 23, 26].

3. Spin composition

An immediate striking difference of narrow-line MOTs with respect to alkali-metal ones is the strong dependence of the MOT center position on detuning [26]. As shown in figure 2(a), we indeed observe a drop of the MOT position when increasing the laser detuning, the amplitude of which largely exceeds the cloud size (see figure 1(c)). This behavior can be explained by considering the MOT equilibrium condition, which requires mean radiative forces to compensate for gravity. When the laser detuning is increased, the MOT position adapts so as to keep the mean amplitude of radiative forces constant.

This picture is supported by the calculation of the *local* detunings $\Delta_{\rm loc}^{(m_J\to m'_J)}$ of optical transitions $|J = 8, m_J\rangle \to |J' = 9, m'_J\rangle$ at the MOT position. We compare in figure 2(c) these detuning values for the σ_-, π and σ_+ transitions starting from the ground state $|J = 8, m_J = -8\rangle$. We observe that, when increasing the detuning Δ, the π and σ_+ transitions become off-resonant, while the local detuning of the σ_- transition tends to a finite value. The detuning of the latter transition is denoted in the following as $\Delta_{\rm loc} \equiv \Delta_{\rm loc}^{(-8\to-9)}$.

This predominance of the σ_- transition leads to optical pumping of the electronic spin towards the absolute ground state, as confirmed by a direct measurement of the spin composition of the atomic sample with a Stern–Gerlach separation of spin levels. To achieve this, we release the atoms from the MOT, apply a vertical magnetic field gradient of about 30 G cm^{-1} during ∼4 ms, and let the atoms expand

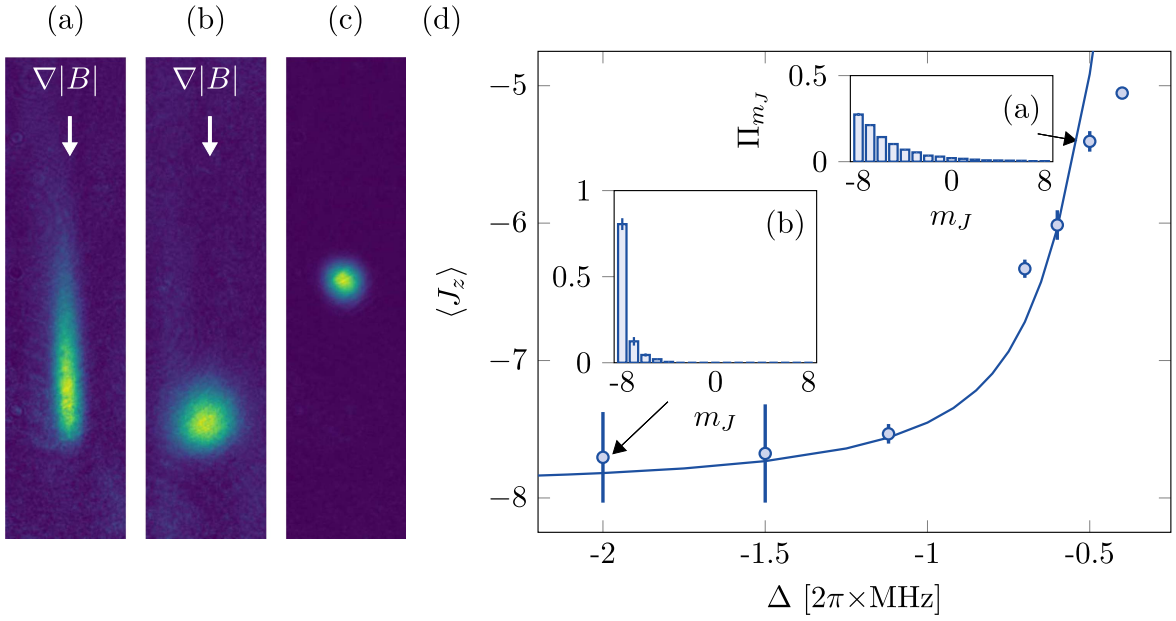

Figure 3. (a), (b) Typical absorption images of the atomic samples taken in our Stern–Gerlach experiment (see text). The populations of individual spin levels can be resolved using a multiple gaussian fit of the atom density. Image (c) serves as a reference image taken in the absence of gradient. (d) Variation of the mean spin projection $\langle J_z \rangle$ with the laser detuning Δ, showing the almost full polarization in the absolute ground state, i.e. $\langle J_z \rangle \simeq -8$, for large detunings ($\Delta \lesssim -2\pi \times 1$ MHz). The solid line corresponds to the prediction of an optical pumping model (see text). Insets show the measured spin population distributions Π_{m_J} for the detunings $\Delta/(2\pi) = -0.5$ MHz and -2 MHz, corresponding to images (a) and (b), respectively. The saturation parameter is $s = 0.65$ and the MOT gradient is $G = 1.71$ G cm^{-1}.

for 20 ms before taking an absorption picture (see figures 3(a)–(c)). We measure the spin composition for several detuning values Δ, and we show two examples of spin population distributions in the insets of figure 3(d). The mean spin projection $\langle J_z \rangle$ inferred from these data is plotted as a function of the detuning Δ in figure 3(d). It reveals an almost full polarization for large detunings $\Delta \lesssim -2\pi \times 1$ MHz, which is the first main result of our study.

In the spin-polarized regime, the theoretical description of the magneto-optical trap can be simplified. As the atomic gas is spin-polarized and the σ_- component of the MOT light dominates over other polarizations, the atom electronic states can be restricted to a two-level system, with a ground state $|J = 8, m_J = -8\rangle$ and an excited state $|J' = 9, m'_J = -9\rangle$ [26]. The radiative force is then calculated by summing the contributions of the six MOT beams, projected on the σ_- polarization. For the sake of simplicity we restrict here the discussion to the motion on the z axis, but extending the model to describe motion along x and y directions is straightforward (see appendix B). The motion along z is governed by the radiative forces induced by the four MOT beams propagating in the plane $x = 0$ (see figure 1(b)). Taking only the σ_- component of these beams into account and neglecting interference effect between the beams, the total force for an atom at rest on the z axis is obtained by summing the radiation pressure forces from the four beams in the $x = 0$ plane. It takes the simple form

$$\mathbf{F}_{\mathrm{rad}} = \frac{\hbar k \Gamma}{2} \frac{s}{1 + 2s + 4\Delta_{\mathrm{loc}}^2/\Gamma^2} \mathbf{e}_z$$

at the MOT position [29][1]. The MOT equilibrium position corresponds to the condition of the radiative force compensating gravity $\mathbf{F}_{\mathrm{rad}} + m\mathbf{g} = \mathbf{0}$, leading to

$$\frac{s}{1 + 2s + 4\Delta_{\mathrm{loc}}^2/\Gamma^2} = \frac{1}{\eta}, \quad \eta = \frac{\hbar k \Gamma}{2mg}, \tag{1}$$

where $\eta \simeq 168$ for the considered optical transition. The local detuning Δ_{loc} thus only depends on the laser intensity s and not on the bare detuning Δ, as

$$\Delta_{\mathrm{loc}} = -\frac{\Gamma}{2}\sqrt{(\eta - 2)s - 1}\,. \tag{2}$$

This expression accounts well for the experimental data presented in figure 2(c): the saturation of the local detuning Δ_{loc} for large detunings corresponds to the spin-polarized regime, where equation (2) applies. For simplicity we do not take into account magnetic forces associated with the magnetic field gradient, as it leads to $\sim$10% corrections on the local detuning Δ_{loc}, which is below our experimental error bars.

To go further this simple approach, we also developed a model taking into account the populations in all Zeeman sublevels. The Zeeman populations in the ground and excited states are calculated as the stationary state of optical pumping rate equations, including the Zeeman shifts corresponding to a given position. We then calculate the radiative force by summing the contributions of all optical transitions, which allows determining the MOT position z_c from the requirement

[1] For a different MOT beam geometrical configuration, with propagation directions along $\pm\mathbf{e}_x$, $\pm\mathbf{e}_y$ and $\pm\mathbf{e}_z$, we would obtain the same expressions for the radiative force, as well as the optical pumping rates described in the following.

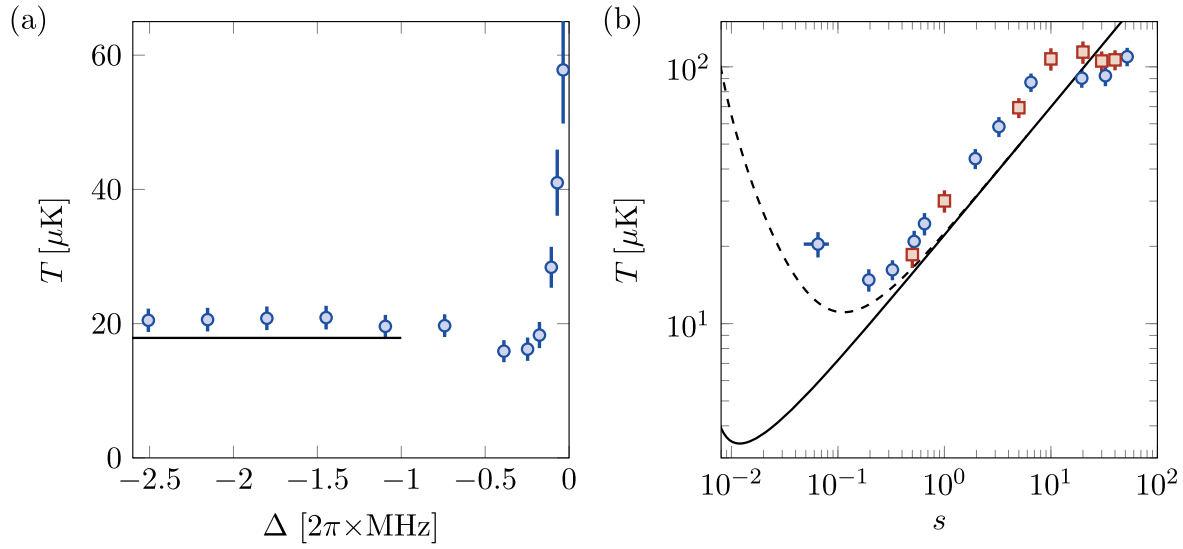

Figure 4. (a) Temperature T of the atomic gas as a function of the laser detuning Δ, for a saturation parameter $s = 0.65$ and a gradient value $G = 1.71$ G cm^{-1}. (b) Temperature T as a function of the saturation parameter s, measured for a gradient $G = 1.71$ G cm^{-1} and laser detunings $\Delta = -2\pi \times 1.84$ MHz (blue dots) and $\Delta = -2\pi \times 2.54$ MHz (red squares). The solid lines in (a) and (b) correspond to the temperature expected in the spin-polarized regime according to equation (4). The dashed line includes the temperature increase expected from the measured intensity noise of the cooling laser beams (see appendix C).

of compensation of the radiative force and gravity. As shown in figure 3(d), this model accounts well for the measured population distributions.

4. Equilibrium temperature

The main interest in using narrow optical transitions for magneto-optical trapping lies in the low equilibrium temperatures, typically in the 20 μK range. In order to investigate the effect of the spin composition of the gas on its equilibrium temperature, we investigated the variation of the temperature T—measured after time-of-flight[2]—with the laser detuning Δ (see figure 4). Far from resonance, we observe that the temperature does not depend on Δ, in agreement with the picture of the spin-polarized regime discussed above (see figure 4(a)). The temperature slightly decreases for -1 MHz $< \Delta/(2\pi) < -0.3$ MHz, i.e. when leaving the spin-polarized regime, before significantly raising closer to resonance.

We also investigated the influence of the laser intensity, by probing the temperature variation with the saturation parameter s (see figure 4(b)). The observed temperature raise upon increasing s can be intuitively understood from equation (2): the local detuning from resonance increases when raising s; we then expect a temperature increase according to the Doppler cooling theory (in the regime $|\Delta_{\rm loc}| > \Gamma/2$ considered here).

A more quantitative understanding requires adapting the theory of Doppler cooling to the experiment geometry. Here we restrict the discussion to the atom dynamics along z, in the spin-polarized regime (see appendix B for a generalization to 3D). The radiative force produced by the four MOT beams in the $x = 0$ plane can be calculated for an atom of velocity v along z, leading to the damping force for small velocities

$$F_{\rm rad} = -m\alpha v, \quad \alpha = -3\frac{\hbar k^2}{m}\frac{s\,\Delta_{\rm loc}/\Gamma}{[1+2s+4(\Delta_{\rm loc}/\Gamma)^2]^2}, \tag{3}$$

which coincides with the usual damping force formula for Doppler cooling for a pair of counter-propagating laser beams of saturation parameter s and detuning $\Delta_{\rm loc}$, up to numerical factors related to the geometry of our laser configuration. In appendix A, we discuss additional experiments on temperature equilibration dynamics, which can be explained qualitatively using the damping rate value (3).

The momentum diffusion coefficient along z, denoted as D_{zz}, is calculated taking into account the contribution of the six cooling laser beams [30], as

$$D_{zz} = \frac{31}{80}\hbar^2 k^2 \Gamma\, \Pi',$$

where $\Pi' = 1/\eta$ is the population in the excited state. The temperature T is then obtained as the ratio $k_B T = D_{zz}/(m\alpha)$, leading to the expression

$$T = \frac{31}{120}\frac{\eta s}{\sqrt{s(\eta-2)-1}}\frac{\hbar\Gamma}{k_B}. \tag{4}$$

Extending this analysis of the atom dynamics to the two other spatial directions x and y leads to slightly different equilibrium temperatures along these axes, but the expected difference is less than 10%, which is below our experimental resolution (see appendix B). According to equation (4), the

[2] The magnetic field gradient is kept on during expansion in order to avoid eddy current effects. We checked that magnetic forces play a negligible role in the expansion dynamics for the flight durations used for this measurement.

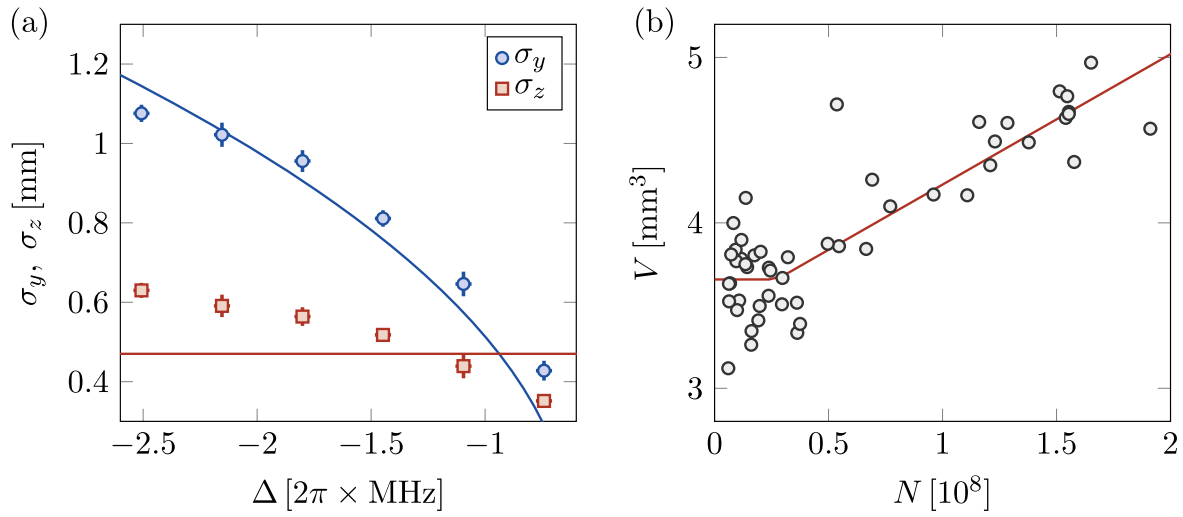

Figure 5. (a) Rms cloud sizes σ_y and σ_z (blue dots and red squares, respectively), measured using absorption images taken *in situ* for $s = 0.65$, $G = 1.71$ G cm^{-1} and $N \sim 2 \times 10^7$. The solid lines correspond to the theoretical values expected in the spin-polarized regime, equations (5) and (7). (b) Volume V of the atomic gas as a function of the atom number N, for $s = 0.65$, $\Delta = -2\pi \times 1.84$ MHz and $G = 1.71$ G cm^{-1}. The solid line is a piecewise linear fit to the experimental data (see equation (9)), consistent with a maximum density reachable in our MOT $n_{\max} = 7(1) \times 10^{10}$ cm^{-3}.

MOT temperature is minimized down to

$$T_{\min} = \frac{31}{60}\frac{\eta}{(\eta-2)}\frac{\hbar\Gamma}{k_B} \simeq 3.4\ \mu\text{K}$$

for $s = 2/(\eta - 2)$, which corresponds to a local detuning $\Delta_{\text{loc}} = \Gamma/2$ according to equation (2). As $\eta \gg 1$, this value is very close to the standard Doppler limit $T_{\text{D}} = \hbar\Gamma/(2k_B)$.

We investigated this behavior by measuring the gas temperature as a function of the saturation parameter s for large laser detunings. As shown in figure 4(b), the measured temperatures are reasonably well reproduced by equation (4) for $0.3 \leqslant s \leqslant 10$. The measured temperatures deviate from theory for small saturation parameter values $s \lesssim 0.1$, which can be explained by the shaking of the atomic sample due to the noise of the cooling laser intensity. We calculate in appendix C the temperature increase expected from the measured intensity noise spectrum (corresponding to rms fluctuations of the saturation parameter s of 5×10^{-3}). We obtain the dashed curve in figure 4(b), which qualitatively reproduces the temperature raise observed for small saturation parameters. A minimal temperature of 15(1) μK is measured for $s = 0.2$. For large saturation parameters $s \gtrsim 10$, the gas does not remain spin-polarized, and the temperature is no longer accounted for by equation (4).

We also observe a raise of the MOT temperature when increasing the atom number, similarly to previous studies on alkali and alkaline-earth atoms [23, 31–33]. We discuss this effect in the appendix A.

5. Cloud sizes and atom density

The atom density in the MOT is an important parameter to consider for efficiently loading the atoms into an optical dipole trap. In this section we characterize the cloud sizes and atom densities achieved in our setup. We measured the horizontal and vertical rms sizes σ_y and σ_z, respectively, using a gaussian fit of the optical density—the absorption image being taken *in situ* (see figure 5(a)). We observe that, in the spin-polarized regime, the vertical size σ_z weakly varies upon an increase of the laser detuning Δ, while the horizontal size σ_y increases over a larger range.

We now explain how one can account for this behavior within the simple model developed above. In the spin-polarized regime, the analytic form of the radiative force allows expressing the equilibrium shape of the atomic sample in a simple manner. Close to the equilibrium position, the radiative force can be expanded linearly as $\mathbf{F}_{\text{rad}} = -\kappa_x x\ \mathbf{e}_x - \kappa_y y\ \mathbf{e}_y - \kappa_z z\ \mathbf{e}_z$, where the spring constants are given by

$$\kappa_x = \frac{2mg}{|z_c|}, \tag{5}$$

$$\kappa_y = \kappa_x/2, \tag{6}$$

$$\kappa_z = \frac{4mg\ \delta\mu G|\Delta_{\text{loc}}|}{s\ \eta\ \hbar\ \Gamma^2}, \tag{7}$$

where $\delta\mu = \mu' - \mu$ is the difference between the magnetic moments in the excited and ground electronic states, denoted as μ' and μ, respectively. Note the simple expression (5) for κ_x, in which the influence of the detuning Δ and saturation parameter s only occurs via the equilibrium position z_c. We remind that the magnetic field gradient is twice larger along x than along y, which explains the relation (6) between the spring constants κ_x and κ_y. The rms cloud sizes σ_u ($u = x, y, z$) are then determined using the thermodynamic relations

$$k_B T = \kappa_u \sigma_u^2. \tag{8}$$

As both the temperature T and local detuning Δ_{loc} are constant in the spin-polarized regime, equations (7) and (8)

predict a constant rms size σ_z, consistent with the weak variation observed experimentally. The variation of the size σ_y is also well captured by this model. A more precise analysis would require taking into account trap anharmonicities, which cannot be completely neglected given the non-gaussian cloud shape (see figure 1(c)).

We also observe a variation of the cloud size when increasing the atom number N with fixed MOT parameters (see figure 5(b)). Such an effect is expected from the repulsive interaction between atoms being dressed by the MOT light, due to the radiation pressure of fluorescence light they exert on each other [34]. We plotted in figure 5(b) the cloud volume V as a function of the atom number N. The volume V is defined as $V = (2\pi)^{3/2}\sigma_x\sigma_y\sigma_z$, so that $n_{\text{peak}} = N/V$ represent the atom density at the trap center. In order to calculate the volume V, we use equation (6) to deduce σ_x from the measured σ_y value. The measurements are consistent with a volume V independent of N for low atom numbers ('temperature-limited' regime) and linearly varying with N for large atom numbers ('density-limited' regime) [34, 35]. The data is fitted with the empirical formula

$$V = V_{\text{single atom}} + \alpha(N - N_c)\Theta(N - N_c), \tag{9}$$

where Θ is the Heaviside function. For the MOT parameters corresponding to figure 5(b), we obtain $V_{\text{single atom}} = 3.7(1)$ mm^3, $N_c = 3(1)\,10^7$ and $\alpha = 8(1) \times 10^{-9}$ mm^3.

Far in the density-limited regime ($N \gg N_c$), we expect the atoms to organize as an ellipsoid of uniform atom density n_{max} corresponding to the maximum atom density that can be reached in the MOT [34, 35]. In such a picture, the volume determined from the rms sizes varies linearly with the atom number, with $\alpha = 0.52\, n_{\text{max}}^{-1}$ (taking into account the non-gaussian atom distribution in this regime). From the fit (9) of our data, we infer for large atom numbers a maximum atom density $n_{\text{max}} = 7(1)\,10^{10}$ cm^{-3}, a value comparable to the ones typically reached with alkali atoms [35].

6. Atom losses due to light-assisted collisions

The variation of the cloud sizes shown in figure 5 indicates that the atom density could be maximized by setting the cooling laser light close to the optical resonance, so as to achieve the smallest cloud volume. However, we observe an increased rate of atom losses near resonance, eventually leading to a reduced atom density. In order to understand this behavior, we present in this section an experimental study of atom losses in the magneto-optical trap, and we interpret the measurements with a simple model based on molecular dynamics resulting from light-induced Van der Waals interactions [36–39].

The loss of atoms is quantitatively characterized by measuring the variation of the atom number N with the time t spent in the magneto-optical trap, in the absence of Zeeman slowing light (see figure 6(a)). The atom decay is fitted with the solution of an atom loss model taking into account one-body atom losses due to collisions with the residual gas and two-body losses, described by the equation

$$\dot{N} = -\frac{N}{\tau_1} - \beta\,\bar{n}N. \tag{10}$$

In this equation, $\tau_1 = 12(2)$s is the one-body lifetime due to collisions with background atoms (background pressure $\simeq 4 \times 10^{-10}$ mbar), β is the two-body loss coefficient and $\bar{n} = n_{\text{peak}}/(2\sqrt{2}) = N/(2\sqrt{2}\,V)$ is the average atom density in the trap. An example of fit of the atom number decay is presented in figure 6(a)[3].

The figure 6(b) shows the variation of the loss coefficient β with the detuning Δ. We observe that the loss coefficient stays almost constant in the spin-polarized regime, with $\beta = 2.6(5) \times 10^{-11}$ cm^3 s^{-1}, and it increases by a factor $\sim$20 when approaching resonance. We can also compare our measurements to the loss coefficient $\beta = 3.7(4) \times 10^{-11}$ cm^3 s^{-1} reported in [15]. As shown in figure 6(b), the two measurements are in good agreement after renormalizing the laser detuning to account for the different saturation parameters used in the two studies, so as to compare atom samples with identical spin composition[4].

We now interpret our loss coefficient measurements using a simple theoretical model in which atom losses originate from light-induced resonant Van der Waals interactions. As shown in figure 7, when an atom is brought to an excited electronic state by absorbing one photon, it experiences strong Van der Waals forces from nearby atoms. For red-detuned laser light, an atom pair is preferentially promoted to attractive molecular potentials. Once excited in such a potential the pair rapidly shrinks and each atom may gain a large amount of kinetic energy. When the molecule spontaneously emits a photon, both atoms return to the electronic ground state with an additional kinetic energy that can be large enough for the atoms to escape the MOT.

We model this phenomenon using a simple description of molecular dynamics, inspired from [36, 39, 40]. The large electron spin of dysprosium leads to an intricate structure of $2(2J + 1)(2J' + 1) = 646$ molecular potential curves that we calculated numerically. The complete description of this complex system is out of the scope of this paper. Fortunately, the main physical effects occurring in the experiment can be captured by a simplified model corresponding to a single effective molecular potential $V_{\text{mol}}(r) = -\lambda\hbar\Gamma/(kr)^3$, with a $1/e$ molecule lifetime $(\mu\Gamma)^{-1}$, where λ and μ are dimensionless numbers. The mean values of these parameters averaged over the 323 attractive molecular potentials are $\bar{\lambda} \simeq 0.68$ and $\bar{\mu} \simeq 1.05$.

The calculation of the two-body loss rate within this model is detailed in appendix D. We show that the laser excitation of atoms from the spin level $|J, m_J\rangle$ to $|J', m_J + q\rangle$

[3] Before fitting the measured atom decay data with equation (10), we fit the measured volume variation with the atom number using the piecewise linear function (9), as discussed in section 5.

[4] Close to the spin-polarized regime, we expect the atom fraction in excited spin levels to scale as s/Δ^2. In order to compare loss coefficients taken for a detuning Δ and saturation parameter s' to data of saturation parameter s with comparable spin composition, we thus renormalize the detuning as $\Delta \to \Delta\sqrt{s/s'}$.

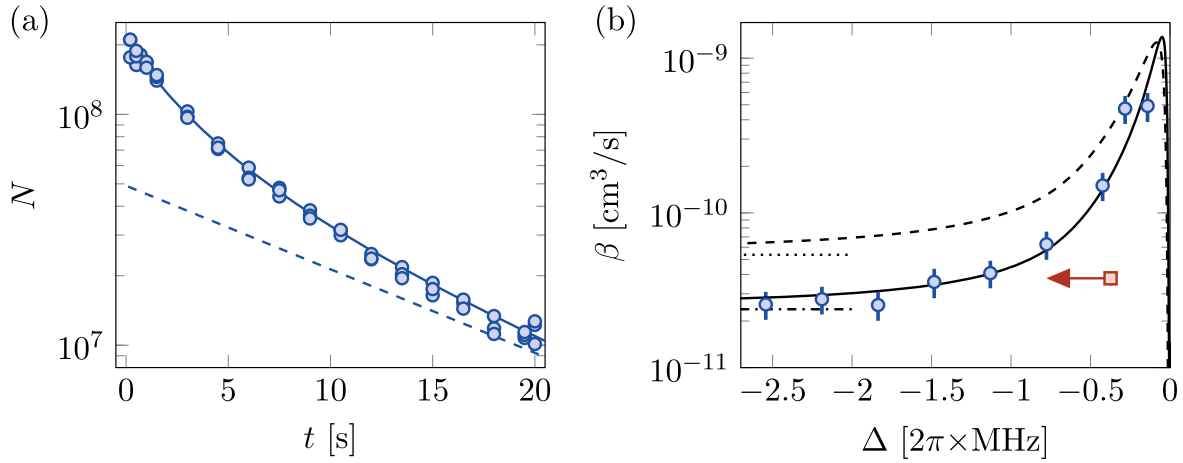

Figure 6. (a) Decay of the atom number with time for a laser detuning $\Delta = -2\pi \times 2.54$ MHz, a saturation parameter $s = 0.65$ and a gradient $G = 1.71$ G cm^{-1}. The data is fitted with a solution of the decay model (10) (solid line), leading to a two-body loss coefficient $\beta = 2.3(5) \times 10^{-11}$ cm^3 s^{-1}. The dashed line corresponds to the exponential asymptote associated with one-body atom losses ($1/e$ time constant $\tau_1 = 12$ s). (b) Variation of the loss coefficient β with the detuning Δ, compared with the predictions of the molecular dynamics model. The dashed line corresponds to molecular parameters $\lambda = \bar{\lambda}$ and $\mu = \bar{\mu}$, while the solid line is a fit with λ and μ being free parameters. The dotted and dashed–dotted lines stand for the corresponding asymptotic expression (12). The red square corresponds to the decay coefficient measured in [15], with the arrow indicating the required detuning renormalization (see text).

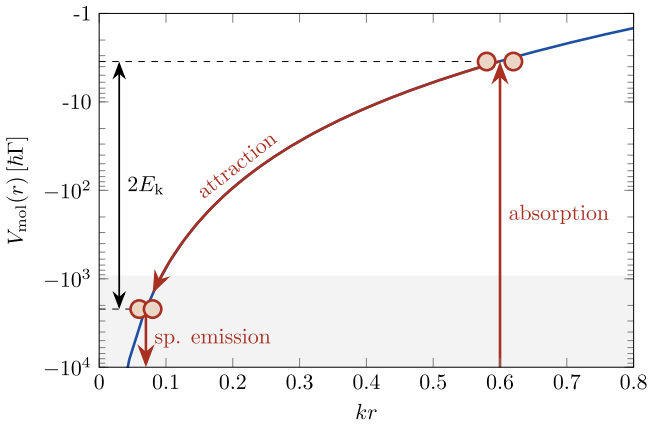

Figure 7. Scheme of the light-induced inelastic collisions. For red-detuned laser light, atom pairs are preferentially excited to an attractive molecular potential (blue line). For the duration τ spent in the excited state, the atoms attract each other, and acquire each a kinetic energy $E_{\rm k}$ before returning to the electronic ground state. The atoms are lost as soon as their kinetic energy exceeds a threshold energy E^*, which is typically much larger than other involved energy scales (see appendix D). The condition for atom losses is represented as a light gray area, corresponding to $2\,E^* = 1000\,\hbar\Gamma$.

($q = -1$, 0 or 1) contributes to the loss coefficient as

$$\beta_{m_J,q} = \Pi_{m_J}\frac{2\pi^2\lambda^2\mu}{3}\,|\langle J', m_J+q|J, m_J; 1, q\rangle|^2 \times\left(\frac{\Gamma}{\Delta_{\rm loc}^{(m_J\to m_J+q)}}\right)^2\frac{s\,\Gamma}{k^3} \times\exp\left[-C\left|\frac{\Gamma}{\Delta_{\rm loc}^{(m_J\to m_J+q)}}\right|^{5/6}\sqrt{\frac{\hbar\Gamma}{E_{\rm r}}}\right],$$

$$C = \sqrt{\frac{\pi}{2}}\,\frac{\Gamma_{\rm E}(5/6)}{6\,\Gamma_{\rm E}(4/3)}\lambda^{1/3}\mu \simeq 0.264\,\lambda^{1/3}\mu, \qquad (11)$$

where $\Gamma_{\rm E}$ is the Euler Gamma function. We remind that Π_{m_J} is the atom fraction in the state $|J, m_J\rangle$ and $\Delta_{\rm loc}^{(m_J\to m_J+q)}$ is the local detuning for the considered optical transition at the MOT position. The exponential factor corresponds to the probability that a molecular association event leads to the loss of the atom pair. The total loss coefficient β is then obtained by summing the contributions $\beta_{m_J,q}$ of all optical transitions.

From equation (11), we see that the atom losses associated with this mechanism are exponentially suppressed when considering broad optical transitions. This suppression plays a large role for alkalis, for which other loss mechanisms dominate, e.g. fine-structure-changing collisions [36]. In the case considered here, the exponential factor has a moderate effect: for the data shown in figure 6(b), it takes the value $\simeq$0.6 for the transition $|J, m_J = -J\rangle \to |J', m_J' = -J'\rangle$ in the spin-polarized regime, assuming $\lambda = \bar{\lambda}$ and $\mu = \bar{\mu}$.

In the spin-polarized regime, the predominance of the transition $|J, m_J = -J\rangle \to |J', m_J' = -J'\rangle$ leads to a simpler expression for the loss coefficient

$$\beta = \beta_{-8,-1} = \frac{2\pi^2\lambda^2\mu}{3}\left(\frac{\Gamma}{\Delta_{\rm loc}}\right)^2 \times\exp\left[-C\left|\frac{\Gamma}{\Delta_{\rm loc}}\right|^{5/6}\sqrt{\frac{\hbar\Gamma}{E_{\rm r}}}\right]\frac{s\,\Gamma}{k^3}. \qquad (12)$$

As the local detuning $\Delta_{\rm loc}$ does not vary with Δ in this regime, we expect a constant loss coefficient β, as observed for the data presented in figure 6(b) for $\Delta \lesssim -2\pi \times 1$ MHz.

In figure 6(b) we show the prediction of the full model for two sets of values for the parameters λ and μ. Using the mean values $\bar{\lambda}$ and $\bar{\mu}$ only provides a qualitative description of the measured loss coefficients. A better agreement is obtained using $\lambda = 0.75$ and $\mu = 0.5$, possibly indicating the important role played by subradiant molecular states, which correspond to $\mu < 1$.

7. Conclusions and perspectives

We presented a detailed experimental study of narrow-line magneto-optical trapping of dysprosium, together with theoretical models supporting our measurements. We showed that the optimal operation of the MOT is obtained for large laser detunings, leading to a spontaneous spin polarization of the atomic sample and to minimal two-body atom losses.

This understanding allows us to prepare gases in ideal conditions for transferring them into an optical dipole trap. In such a non-dissipative trap, it is crucial to produce atomic samples polarized in the electronic ground state in order to avoid dipolar relaxation [41, 42]. In preliminary experiments, we were able to trap about 2×10^7 atoms into an optical dipole trap created by a single laser beam of wavelength $\lambda = 1070$ nm and optical power $P = 40$ W, focused to a waist of 35 μm. Optimal efficiency of the dipole trap loading is obtained by first preparing the MOT at the lowest achieved temperature of 15 μK (corresponding to parameters $\Delta = -2\pi \times 1.8$ MHz, $s = 0.2$ and $G = 1.7\,\mathrm{G\,cm^{-1}}$), and then superimposing the dipole trap over the MOT center during 600 ms. The phase space density of $\simeq 8 \times 10^{-5}$ reached after the dipole trap loading corresponds to a good starting point to reach quantum degeneracy via evaporative cooling [1, 3].

Our study will be of direct interest for magneto-optical traps of other atomic species featuring both narrow optical transitions and a spinful electronic state, such as the other magnetic lanthanides. Future work could investigate sub-Doppler cooling to very low temperatures in optical molasses. Contrary to sub-Doppler mechanisms observed with magnetic lanthanides in broad-line magneto-optical traps [13, 43, 44], reaching temperatures below the Doppler limit of the 626 nm optical transition would require applying an optical molasses at low magnetic field [45, 46].

Acknowledgments

We thank E Wallis and T Tian for their contribution in the early stage of the experiment. This work is supported by the European Research Council (Synergy grant UQUAM) and the Idex PSL Research University (ANR-10-IDEX-0001-02 PSL⋆). L S acknowledges the support from the European Union (H2020-MSCA-IF-2014 grant no. 661433).

Appendix A. Additional temperature measurements

In this appendix we describe further temperature measurements related to the equilibration dynamics and to the influence of the atom density.

We studied the equilibration dynamics in the magneto-optical trap by measuring the time evolution of the temperature right after the trap parameters have been set to the 'compressed MOT' values. We show such an evolution in figure A1(a), corresponding to MOT parameters $s = 0.65$, $\Delta = -2\pi \times 1.84$ MHz and $G = 1.71\,\mathrm{G\,cm^{-1}}$. The temperature variation is fitted with an exponential decay of $1/e$ time constant $\tau = 29(11)$ ms, with a baseline of 23.6(9) μK. No significant atom loss is observed over the duration of equilibration. This measurement allows extracting a damping coefficient $\alpha = 1/(2\tau) = 17(6)\mathrm{s^{-1}}$, comparable but smaller than the value $\alpha = 47(2)\mathrm{s^{-1}}$ given by the simplified model leading to equation (3).

We also investigated the raise of the MOT temperature when increasing the atom number [23, 31–33]. In previous studies, such an effect was attributed to multiple scattering of photons within the atomic sample [32], leading to a temperature raising linearly with the peak atom density n_{peak}, as

$$T(n) = T_{\mathrm{single\ atom}} + \gamma\, n_{\mathrm{peak}}.$$

We investigated this behavior by measuring the gas temperature for various atom densities. The atom density was varied by loading different atom numbers $4 \times 10^7 \leqslant N \leqslant 2 \times 10^8$ or using different gradient values $1.1\,\mathrm{G\,cm^{-1}} \leqslant G \leqslant 5.3\,\mathrm{G\,cm^{-1}}$. Note that the highest atom density used for this study ($n_{\mathrm{peak}} \simeq 1.1 \times 10^{11}\,\mathrm{cm^{-3}}$) exceeds the maximum density n_{max} discussed in the main text as we use here larger magnetic field gradients. As shown in figure A1(b), our measurements are compatible with a linear variation of the temperature with density, with a slope $\gamma = 8(1) \times 10^{-11}\,\mu\mathrm{K\,cm^3}$. This value is comparable with the one obtained with Cs gray molasses [32].

Appendix B. MOT temperature in the spin-polarized regime

In this section we give a more detailed description of the MOT temperature calculation and extend the analysis to the atom dynamics in three spatial directions. We restrict the discussion to the spin-polarized regime.

In order to extract the damping coefficient, the radiative force can be expanded at the equilibrium position $\mathbf{r}_c$ as

$$\mathbf{F}_{\mathrm{rad}}(\mathbf{r}_c, \mathbf{v}) = -m\alpha\left(\frac{2}{3}v_x\mathbf{e}_x + v_y\mathbf{e}_y + v_z\mathbf{e}_z\right) + \mathcal{O}(v^2),$$

where α was introduced in the main text, see equation (3). The anisotropy of the damping comes the specific geometry of our setup (see figure 1(b)).

The momentum diffusion tensor D is calculated as the sum of the diffusion tensors D^{abs} and D^{em}, associated with the stochastic absorption and spontaneous emission events, respectively. Taking into account the geometry of our experiment (see figure 1(b)), we obtain the diffusion coefficients

$$D^{\mathrm{abs}} = \frac{1}{16\eta}\hbar^2k^2\Gamma\begin{pmatrix}2&0&0\\0&3&0\\0&0&3\end{pmatrix},$$

$$D^{\mathrm{em}} = \frac{1}{20\eta}\hbar^2k^2\Gamma\begin{pmatrix}3&0&0\\0&3&0\\0&0&4\end{pmatrix}.$$

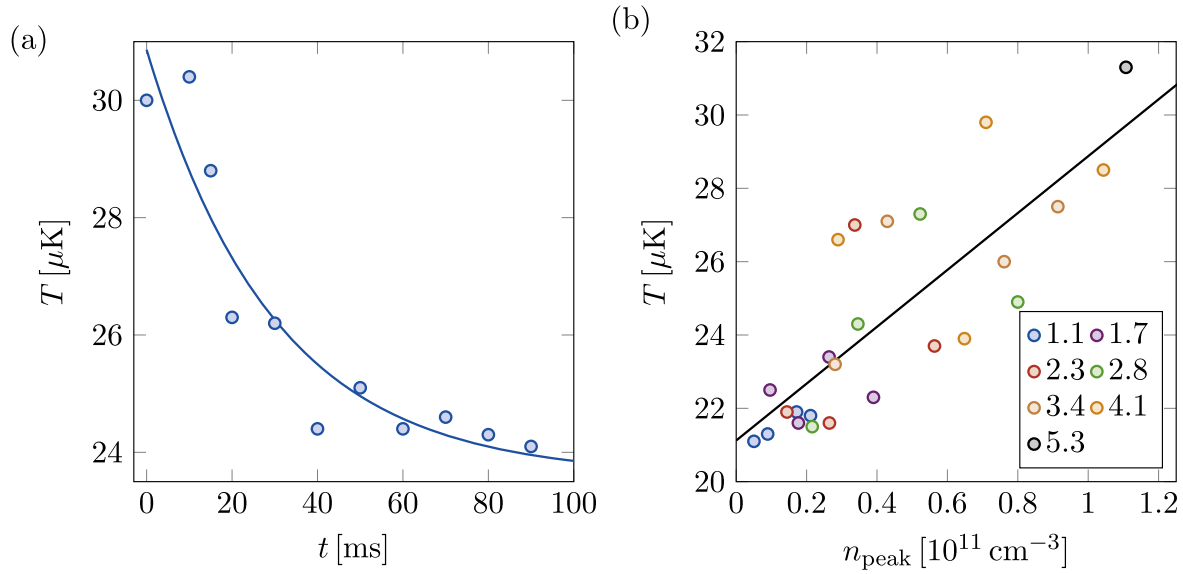

Figure A1. (a) Evolution of the gas temperature T with time t right after the MOT parameters are set to the 'compressed MOT' values. The solid line is an exponential fit of the equilibration dynamics. (b) Temperature T as a function of atom density n, measured for various atom numbers and gradient values, indicated in the legend (in G cm^{-1}). The solid line is a linear fit of slope $\gamma = 8(1) \times 10^{-11}\,\mu$K cm^3.

The temperature is then obtained according to $k_B T = D/(m\alpha)$ and reveals weak anisotropy:

$$\begin{pmatrix} T_x \\ T_y \\ T_z \end{pmatrix} = \frac{\eta s}{\sqrt{s(\eta - 2) - 1}} \begin{pmatrix} 33/120 \\ 27/120 \\ 31/120 \end{pmatrix} \frac{\hbar\Gamma}{k_B}.$$

Appendix C. Temperature increase due to the laser intensity noise

In this section we give more details on the calculation of the temperature increase due to fluctuations of the cooling laser intensity, leading to a time-dependent saturation parameter $s(t)$. The main heating effect comes from fluctuations of the trap center $z_c(t)$, which can be related to $s(t)$ using the equilibrium condition (1).

For simplicity we restrict the discussion to the atom dynamics along the z axis. The atom dynamics is described by Newton's equation

$$m\ddot{z} = -\kappa_z[z - z_c(t)] - m\alpha\dot{z} + F_{\mathrm{L}}(t). \tag{C.1}$$

Here, $F_{\mathrm{L}}(t)$ is the Langevin force associated with stochastic radiative processes, such that $\langle F_{\mathrm{L}}(t)\rangle = 0$ and $\langle F_{\mathrm{L}}(t)F_{\mathrm{L}}(t')\rangle = 2D\delta(t - t')$, involving the diffusion coefficient introduced in the main text. By integrating equation (C.1), we calculate the rms fluctuations of the velocity, as

$$\langle \dot{z}^2 \rangle = \frac{D}{m^2\alpha} + \left(\frac{\mathrm{d}z_c}{\mathrm{d}s}\right)^2 \int \mathrm{d}\omega\, \frac{\omega_0^4\omega^2}{(\omega_0^2 - \omega^2)^2 + \omega^2\alpha^2} S(\omega), \tag{C.2}$$

where $S(\omega)$ is the spectral density of the saturation parameter noise and $\omega_0 = \sqrt{\kappa_z/m}$. The equilibrium temperature is then obtained as $T = m\langle \dot{z}^2\rangle/k_B$. Note that for small damping rates α and in the absence of Langevin forces, equation (C.2) is consistent with the heating rates expected from [47] for shaken conservative traps. The dashed line in figure 4(b) is calculated using equation (C.2) and the measured noise spectrum, shown in figure C1 for the lowest saturation parameter $s = 0.065$ explored in figure 4(b). Note that, during the MOT loading and compression, the laser intensity is servo-locked to a PID controller, typically over the range $0.065 \lesssim s \leqslant 50$.

Appendix D. Calculation of the inelastic loss rate

In this section we describe the two-body loss model used in the main text to interpret the measured loss coefficients, adapting thereby standard treatments to the case of dysprosium atoms [36, 37].

We assume the nonlinear atom losses to be triggered by the light-assisted formation of molecules. Once the pair of atoms is excited to an attractive molecular state, strong Van der Waals forces induce fast atom dynamics, leading to atom losses once the molecule is de-excited after spontaneous emission.

A precise modeling is a challenging task, as it requires calculating the 646 molecular potentials and the corresponding excitation amplitudes, taking into account the local magnetic field value and the orientation of atom pairs. We consider here a single effective molecular potential $V_{\mathrm{mol}}(r) = -\lambda\hbar\Gamma/(kr)^3$, of $1/e$ lifetime $(\mu\Gamma)^{-1}$. For simplicity we consider a uniform atom density $n = N/V$. The atom loss can be described by the equation

$$\dot{N} = -\frac{n^2}{2}\int \mathrm{d}\mathbf{r}_1\,\mathrm{d}\mathbf{r}_2\, 2\Gamma_{\mathrm{asso}}(|\mathbf{r}_1 - \mathbf{r}_2|)P_{\mathrm{loss}}(|\mathbf{r}_1 - \mathbf{r}_2|), \tag{D.1}$$

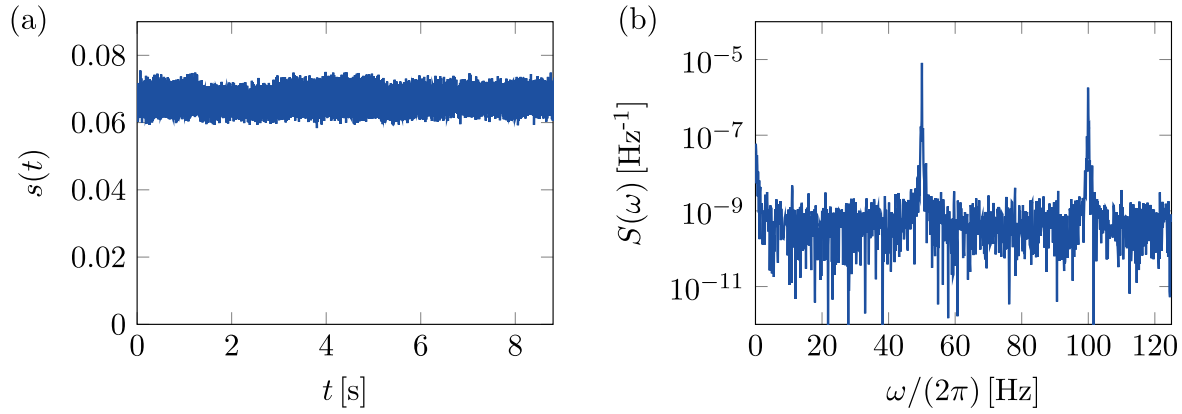

Figure C1. (a) Time evolution of the saturation parameter s, for the smallest mean value $s = 0.065$ explored in figure 4(b). The rms fluctuations of 5×10^{-3} result from the ∼80 dB dynamic range of the intensity locking system. (b) Spectral density $S(\omega)$ of the saturation parameter noise corresponding to (*a*).

where $\Gamma_{\rm asso}(r)$ is the rate of molecule formation for a pair of atoms of relative distance r, and $P_{\rm loss}(r)$ is the probability to lose this pair of atoms after de-excitation. The factor $\frac{1}{2}$ avoids double counting and the factor 2 accounts for the fact that each loss event corresponds to the loss of two atoms. Equation (D.1) can be recast as

$$\dot{N} = -\beta n N, \quad \beta = \int \mathrm{d}\mathbf{r}\, \Gamma_{\rm asso}(r) P_{\rm loss}(r).$$

Consider a pair of atoms in the MOT separated by the distance $r_{\rm i}$. We assume the rate of molecular association, triggered by the absorption of a photon ($q = -1$, 0 or 1 referring to σ_-, π or σ_+ polarizations, respectively) by an atom of spin $|J, m_J\rangle$, to be given by the standard algebra of atom-light interaction, as

$$\Gamma_{\rm asso}(r_{\rm i}) = |\langle J', m_J + q | J, m_J; 1, q\rangle|^2 \frac{\mu\Gamma}{2} \times \frac{2s}{1 + 4[\Delta_{\rm loc} - V_{\rm mol}(r_{\rm i})/\hbar]^2/(\mu\Gamma)^2}, \quad \text{(D.2)}$$

where we ignore intensity saturation effects.

Once the molecule is formed, the atom pair evolves according to Newton's law $(m/2)\ddot{r} = -\partial_r V_{\rm mol}(r)$, which can be solved implicitly. We neglect the initial atom motion as it corresponds to a weak energy scale for this problem. The electronic excitation decays after a duration τ, corresponding to a distance $r_{\rm f}(r_{\rm i}, \tau)$, such that

$$\int_{r_{\rm f}}^{r_{\rm i}} \frac{\mathrm{d}r}{\sqrt{r^{-3} - r_{\rm i}^{-3}}} = 2\sqrt{\frac{\lambda\hbar\Gamma}{mk^3}}\,\tau.$$

The acquired kinetic energy per atom $E_{\rm k}$ is obtained from energy conservation, as $2E_{\rm k}(r_{\rm i}, \tau) = V(r_{\rm i}) - V(r_{\rm f})$.

The atom pair is lost if the acquired kinetic energy exceeds a threshold energy E^*. This energy can be calculated by solving numerically the equation of motion of an atom of kinetic energy E^*, initially located at the equilibrium position $\mathbf{r}_c$, and subjected to the radiative forces. For the MOT parameters corresponding to the data of atom number represented in figure 6(a), we estimate a capture velocity v^* of about $0.6\,\mathrm{m\,s^{-1}}$, corresponding to an energy $E^* \simeq 500\,\hbar\Gamma$.

The loss probability is then obtained as the probability for the atoms to acquire enough kinetic energy during the molecular dynamics:

$$P_{\rm loss}(r_{\rm i}) = \int_0^\infty \mathrm{d}\tau\ \mu\Gamma e^{-\mu\Gamma\tau}\Theta[E_{\rm k}(r_{\rm i}, \tau) - E^*],$$

where $\mu\Gamma e^{-\mu\Gamma\tau}$ is the density probability for the spontaneous emission to occur at time τ (Θ is the Heaviside function). We obtain

$$P_{\rm loss}(r_{\rm i}) = \exp\left(-\frac{\mu}{2\sqrt{\lambda}}(kr_{\rm i})^{5/2}\sqrt{\frac{\hbar\Gamma}{2E_{\rm r}}}f \times \left[\left(1 + \frac{E^*}{|V_{\rm mol}(r_i)|}\right)^{-1/3}\right]\right),$$

where $f(x) = \int_x^1 \frac{\mathrm{d}u}{\sqrt{u^{-3} - 1}}$. As the threshold energy E^* is much larger than other energy scales, we can safely replace the factor $f[\cdot]$ by $f(0) = \sqrt{\pi}\,\Gamma_{\rm E}(5/6)/[3\,\Gamma_{\rm E}(4/3)]$.

The loss rate can then be obtained by calculating numerically the integral (D.1). We find that replacing the Lorentz absorption profile (D.2) by a strict resonance condition (i.e. the suitable Dirac δ function) only introduces minor differences for the numerical value of β. After this replacement the integral can be calculated analytically, leading to the formula (11) in the main text.

References

[1] Lu M, Burdick N Q, Youn S H and Lev B L 2011 Strongly dipolar Bose–Einstein condensate of dysprosium *Phys. Rev. Lett.* **107** 190401

[2] Aikawa K, Frisch A, Mark M, Baier S, Rietzler A, Grimm R and Ferlaino F 2012 Bose–Einstein condensation of erbium *Phys. Rev. Lett.* **108** 210401

[3] Lu M, Burdick N Q and Lev B L 2012 Quantum degenerate dipolar Fermi gas *Phys. Rev. Lett.* **108** 215301

[4] Aikawa K, Baier S, Frisch A, Mark M, Ravensbergen C and Ferlaino F 2014 Observation of Fermi surface deformation in a dipolar quantum gas *Science* **345** 1484

[5] Baier S, Mark M J, Petter D, Aikawa K, Chomaz L, Cai Z, Baranov M, Zoller P and Ferlaino F 2016 Extended Bose–Hubbard models with ultracold magnetic atoms *Science* **352** 201

[6] Ferrier-Barbut I, Kadau H, Schmitt M, Wenzel M and Pfau T 2016 Observation of quantum droplets in a strongly dipolar Bose gas *Phys. Rev. Lett.* **116** 215301

[7] Kadau H, Schmitt M, Wenzel M, Wink C, Maier T, Ferrier-Barbut I and Pfau T 2016 Observing the Rosensweig instability of a quantum ferrofluid *Nature* **530** 194

[8] Frisch A, Mark M, Aikawa K, Ferlaino F, Bohn J L, Makrides C, Petrov A and Kotochigova S 2014 Quantum chaos in ultracold collisions of gas-phase erbium atoms *Nature* **507** 475

[9] Maier T *et al* 2015 Emergence of chaotic scattering in ultracold Er and Dy *Phys. Rev.* X **5** 041029

[10] Cui X, Lian B, Ho T-L, Lev B L and Zhai H 2013 Synthetic gauge field with highly magnetic lanthanide atoms *Phys. Rev.* A **88** 011601

[11] Nascimbene S 2013 Realizing one-dimensional topological superfluids with ultracold atomic gases *J. Phys. B: At. Mol. Opt. Phys.* **46** 134005

[12] Burdick N Q, Tang Y and Lev B L 2016 Long-lived spin-orbit-coupled degenerate dipolar Fermi gas *Phys. Rev.* X **6** 031022

[13] Youn S H, Lu M, Ray U and Lev B L 2010 Dysprosium magneto-optical traps *Phys. Rev.* A **82** 043425

[14] Lu M, Youn S H and Lev B L 2010 Trapping ultracold dysprosium: a highly magnetic gas for dipolar physics *Phys. Rev. Lett.* **104** 063001

[15] Maier T, Kadau H, Schmitt M, Griesmaier A and Pfau T 2014 Narrow-line magneto-optical trap for dysprosium atoms *Opt. Lett.* **39** 3138

[16] Hemmerling B, Drayna G K, Chae E, Ravi A and Doyle J M 2014 Buffer gas loaded magneto-optical traps for Yb, Tm, Er and Ho *New J. Phys.* **16** 063070

[17] Miao J, Hostetter J, Stratis G and Saffman M 2014 Magneto-optical trapping of holmium atoms *Phys. Rev.* A **89** 041401

[18] McClelland J J and Hanssen J L 2006 Laser cooling without repumping: a magneto-optical trap for erbium atoms *Phys. Rev. Lett.* **96** 143005

[19] Berglund A J, Hanssen J L and McClelland J J 2008 Narrow-line magneto-optical cooling and trapping of strongly magnetic atoms *Phys. Rev. Lett.* **100** 113002

[20] Frisch A, Aikawa K, Mark M, Rietzler A, Schindler J, Zupanič E, Grimm R and Ferlaino F 2012 Narrow-line magneto-optical trap for erbium *Phys. Rev.* A **85** 051401

[21] Sukachev D, Sokolov A, Chebakov K, Akimov A, Kanorsky S, Kolachevsky N and Sorokin V 2010 Magneto-optical trap for thulium atoms *Phys. Rev.* A **82** 011405

[22] Kuwamoto T, Honda K, Takahashi Y and Yabuzaki T 1999 Magneto-optical trapping of Yb atoms using an intercombination transition *Phys. Rev.* A **60** R745

[23] Katori H, Ido T, Isoya Y and Kuwata-Gonokami M 1999 Magneto-optical trapping and cooling of strontium atoms down to the photon recoil temperature *Phys. Rev. Lett.* **82** 1116

[24] Binnewies T, Wilpers G, Sterr U, Riehle F, Helmcke J, Mehlstäubler T E, Rasel E M and Ertmer W 2001 Doppler cooling and trapping on forbidden transitions *Phys. Rev. Lett.* **87** 123002

[25] Gustavsson M, Lundberg H, Nilsson L and Svanberg S 1979 Lifetime measurements for excited states of rare-earth atoms using pulse modulation of a cw dye-laser beam *J. Opt. Soc. Am.* **69** 984

[26] Loftus T H, Ido T, Boyd M M, Ludlow A D and Ye J 2004 Narrow line cooling and momentum-space crystals *Phys. Rev.* A **70** 063413

[27] Lu M, Youn S H and Lev B L 2011 Spectroscopy of a narrow-line laser-cooling transition in atomic dysprosium *Phys. Rev.* A **83** 012510

[28] Leefer N, Cingöz A, Gerber-Siff B, Sharma A, Torgerson J R and Budker D 2010 Transverse laser cooling of a thermal atomic beam of dysprosium *Phys. Rev.* A **81** 043427

[29] Metcalf H J and van der Straten P 1999 *Laser Cooling and Trapping of Neutral Atoms* (New York: Springer)

[30] Wineland D J and Itano W M 1979 Laser cooling of atoms *Phys. Rev.* A **20** 1521

[31] Drewsen M, Laurent P, Nadir A, Santarelli G, Clairon A, Castin Y, Grison D and Salomon C 1994 Investigation of sub-Doppler cooling effects in a cesium magneto-optical trap *Appl. Phys.* B **59** 283

[32] Boiron D, Michaud A, Lemonde P, Castin Y, Salomon C, Weyers S, Szymaniec K, Cognet L and Clairon A 1996 Laser cooling of cesium atoms in gray optical molasses down to 1.1 μK *Phys. Rev.* A **53** R3734

[33] Kerman A J, Vuletić V, Chin C and Chu S 2000 Beyond optical molasses: 3D Raman sideband cooling of atomic cesium to high phase-space density *Phys. Rev. Lett.* **84** 439

[34] Walker T, Sesko D and Wieman C 1990 Collective behavior of optically trapped neutral atoms *Phys. Rev. Lett.* **64** 408

[35] Townsend C G, Edwards N H, Cooper C J, Zetie K P, Foot C J, Steane A M, Szriftgiser P, Perrin H and Dalibard J 1995 Phase-space density in the magneto-optical trap *Phys. Rev.* A **52** 1423

[36] Gallagher A and Pritchard D E 1989 Exoergic collisions of cold Na^*–Na *Phys. Rev. Lett.* **63** 957

[37] Julienne P S and Vigué J 1991 Cold collisions of ground- and excited-state alkali-metal atoms *Phys. Rev.* A **44** 4464

[38] Julienne P S, Smith A M and Burnett K 1992 Theory of collisions between laser cooled atoms *Adv. At. Mol. Opt. Phys.* **30** 141

[39] Dinneen T P, Vogel K R, Arimondo E, Hall J L and Gallagher A 1999 Cold collisions of Sr^*–Sr in a magneto-optical trap *Phys. Rev.* A **59** 1216

[40] Lett P D, Mølmer K, Gensemer S D, Tan K Y N, Kumarakrishnan A, Wallace C D and Gould P L 1995 Hyperfine structure modifications of collisional losses from light-force atom traps *J. Phys. B: At. Mol. Opt. Phys.* **28** 65

[41] Hensler S, Werner J, Griesmaier A, Schmidt P O, Görlitz A, Pfau T, Giovanazzi S and Rzążewski K 2003 Dipolar relaxation in an ultra-cold gas of magnetically trapped chromium atoms *Appl. Phys.* B **77** 765

[42] Burdick N Q, Baumann K, Tang Y, Lu M and Lev B L 2015 Fermionic suppression of dipolar relaxation *Phys. Rev. Lett.* **114** 023201

[43] Berglund A J, Lee S A and McClelland J J 2007 Sub-Doppler laser cooling and magnetic trapping of erbium *Phys. Rev.* A **76** 053418

[44] Youn S H, Lu M and Lev B L 2010 Anisotropic sub-Doppler laser cooling in dysprosium magneto-optical traps *Phys. Rev.* A **82** 043403

[45] Dalibard J and Cohen-Tannoudji C 1989 Laser cooling below the Doppler limit by polarization gradients: simple theoretical models *J. Opt. Soc. Am.* B **6** 2023

[46] Ungar P J, Weiss D S, Riis E and Chu S 1989 Optical molasses and multilevel atoms: theory *J. Opt. Soc. Am.* B **6** 2058

[47] Savard T A, O'Hara K M and Thomas J E 1997 Laser-noise-induced heating in far-off resonance optical traps *Phys. Rev.* A **56** R1095

Bibliography

Bibliography

[1] H. Kadau, M. Schmitt, M. Wenzel, C. Wink, T. Maier, I. Ferrier-Barbut, and T. Pfau. Observing the Rosensweig instability of a quantum ferrofluid. *Nature*, 530(7589):194, 2016.

[2] L. Santos, G. V. Shlyapnikov, and M. Lewenstein. Roton-maxon spectrum and stability of trapped dipolar Bose-Einstein condensates. *Phys. Rev. Lett.*, 90(25):250403, 2003.

[3] L. Chomaz, R. M. W. Bijnen, D. Petter, G. Faraoni, S. Baier, J. H. Becher, M. J. Mark, F. Wächtler, L. Santos, and F. Ferlaino. Observation of roton mode population in a dipolar quantum gas. *Nature Physics*, page 1, 2018.

[4] M. H. Anderson, J. R. Ensher, M. R. Matthews, C. E. Wieman, and E. A. Cornell. Observation of Bose-Einstein Condensation in a dilute atomic vapor. *Science*, 269(5221):198–201, 1995.

[5] K. B. Davis, M. O. Mewes, M. R. Andrews, N. J. van Druten, D. S. Durfee, D. M. Kurn, and W. Ketterle. Bose-Einstein Condensation in a gas of Sodium atoms. *Phys. Rev. Lett.*, 75:3969–3973, Nov 1995.

[6] B. DeMarco and D. S. Jin. Onset of Fermi degeneracy in a trapped atomic gas. *Science*, 285(5434):1703–1706, 1999.

[7] A. G. Truscott, K. E. Strecker, W. I. McAlexander, G. B. Partridge, and R. G. Hulet. Observation of Fermi pressure in a gas of trapped atoms. *Science*, 291(5513):2570–2572, 2001.

[8] M. Greiner, O. Mandel, T. Esslinger, T. W. Hänsch, and I. Bloch. Quantum phase transition from a superfluid to a Mott insulator in a gas of ultracold atoms. *Nature*, 415(6867):39, 2002.

[9] W. S. Bakr, J. I. Gillen, A. Peng, S. Fölling, and M. Greiner. A quantum gas microscope for detecting single atoms in a Hubbard-regime optical lattice. *Nature*, 462(7269):74, 2009.

[10] J. F. Sherson, C. Weitenberg, M. Endres, M. Cheneau, I. Bloch, and S. Kuhr. Single-atom-resolved fluorescence imaging of an atomic Mott insulator. *Nature*, 467(7311):68, 2010.

[11] L. W. Cheuk, M. A. Nichols, M. Okan, T. Gersdorf, V. V. Ramasesh, W. S. Bakr, T. Lompe, and M. W. Zwierlein. Quantum-gas microscope for fermionic atoms. *Phys. Rev. Lett.*, 114:193001, May 2015.

[12] E. Haller, J. Hudson, A. Kelly, D. A. Cotta, B. Peaudecerf, G. D. Bruce, and S. Kuhr. Single-atom imaging of fermions in a quantum-gas microscope. *Nature Physics*, 11(9):738, 2015.

[13] A. Görlitz, J. M. Vogels, A. E. Leanhardt, C. Raman, T. L. Gustavson, J. R. Abo-Shaeer, A. P. Chikkatur, S. Gupta, S. Inouye, and T. Rosenband. Realization of Bose-Einstein condensates in lower dimensions. *Phys. Rev. Lett.*, 87(13):130402, 2001.

[14] D. Rychtarik, B. Engeser, H.-C. Nägerl, and R. Grimm. Two-dimensional Bose-Einstein Condensate in an optical surface trap. *Phys. Rev. Lett.*, 92:173003, Apr 2004.

[15] M. Köhl, H. Moritz, T. Stöferle, C. Schori, and T. Esslinger. Superfluid to Mott insulator transition in one, two, and three dimensions. *Journal of Low Temperature Physics*, 138(3):635–644, 2005.

[16] Z. Hadzibabic, P. Krüger, M. Cheneau, B. Battelier, and J. Dalibard. Berezinskii–Kosterlitz–Thouless crossover in a trapped atomic gas. *Nature*, 441(7097):1118, 2006.

[17] A. Isacsson and S. M. Girvin. Multiflavor bosonic hubbard models in the first excited bloch band of an optical lattice. *Phys. Rev. A*, 72(5):053604, 2005.

[18] A. S. Sørensen, E. Demler, and M. D. Lukin. Fractional quantum hall states of atoms in optical lattices. *Phys. Rev. Lett.*, 94(8):086803, 2005.

[19] V. W. Scarola and S. D. Sarma. Quantum phases of the extended bose-hubbard hamiltonian: Possibility of a supersolid state of cold atoms in optical lattices. *Phys. Rev. Lett.*, 95(3):033003, 2005.

[20] T. Bourdel, L. Khaykovich, J. Cubizolles, J. Zhang, F. Chevy, M. Teichmann, L. Tarruell, S. Kokkelmans, and C. Salomon. Experimental study of the BEC-BCS crossover region in Lithium 6. *Phys. Rev. Lett.*, 93(5):050401, 2004.

[21] M. Bartenstein, A. Altmeyer, S. Riedl, S. Jochim, C. Chin, J. H. Denschlag, and R. Grimm. Collective excitations of a degenerate gas at the BEC-BCS crossover. *Phys. Rev. Lett.*, 92(20):203201, 2004.

[22] C. A. Regal, C. Ticknor, J. L. Bohn, and D. S. Jin. Creation of ultracold molecules from a Fermi gas of atoms. *Nature*, 424(6944):47, 2003.

[23] A. L. Gaunt, T. F. Schmidutz, I. Gotlibovych, R. P. Smith, and Z. Hadzibabic. Bose-Einstein condensation of atoms in a uniform potential. *Phys. Rev. Lett.*, 110(20):200406, 2013.

[24] L. M. Duan, E. Demler, and M. D. Lukin. Controlling spin exchange interactions of ultracold atoms in optical lattices. *Phys. Rev. Lett.*, 91:090402, Aug 2003.

[25] N. Strohmaier, Y. Takasu, K. Günter, R. Jördens, M. Köhl, H. Moritz, and T. Esslinger. Interaction-controlled transport of an ultracold Fermi gas. *Phys. Rev. Lett.*, 99(22):220601, 2007.

[26] D. Stadler, S. Krinner, J. Meineke, J. P. Brantut, and T. Esslinger. Observing the drop of resistance in the flow of a superfluid Fermi gas. *Nature*, 491(7426):736, 2012.

[27] L. Tarruell, D. Greif, T. Uehlinger, G. Jotzu, and T. Esslinger. Creating, moving and merging Dirac points with a Fermi gas in a tunable honeycomb lattice. *Nature*, 483(7389):302, 2012.

[28] T. Uehlinger, G. Jotzu, M. Messer, D. Greif, W. Hofstetter, U. Bissbort, and T. Esslinger. Artificial graphene with tunable interactions. *Phys. Rev. Lett.*, 111(18):185307, 2013.

[29] R. P. Feynman. Simulating physics with computers. *International journal of theoretical physics*, 21(6-7):467–488, 1982.

[30] I. Bloch, J. Dalibard, and S. Nascimbène. Quantum simulations with ultracold quantum gases. *Nature Physics*, 8(4):267, 2012.

[31] I. Bloch. Quantum coherence and entanglement with ultracold atoms in optical lattices. *Nature*, 453(7198):1016, 2008.

[32] A. Frisch. *Dipolar quantum gases of Erbium*. PhD thesis, 2014.

[33] A. Griesmaier, J. Werner, S. Hensler, J. Stuhler, and T. Pfau. Bose-Einstein condensation of Chromium. *Phys. Rev. Lett.*, 94(16):160401, 2005.

[34] J. Stuhler, A. Griesmaier, T. Koch, M. Fattori, T. Pfau, S. Giovanazzi, P. Pedri, and L. Santos. Observation of dipole-dipole interaction in a degenerate quantum gas. *Phys. Rev. Lett.*, 95(15):150406, 2005.

[35] T. Koch, T. Lahaye, J. Metz, B. Fröhlich, A. Griesmaier, and T. Pfau. Stabilization of a purely dipolar quantum gas against collapse. *Nature Physics*, 4(3):218, 2008.

[36] M. Lu, N. Q. Burdick, S. H. Youn, and B. L. Lev. Strongly dipolar Bose-Einstein Condensate of Dysprosium. *Phys. Rev. Lett.*, 107:190401, Oct 2011.

[37] K. Aikawa, A. Frisch, M. Mark, S. Baier, A. Rietzler, R. Grimm, and F. Ferlaino. Bose-Einstein Condensation of Erbium. *Phys. Rev. Lett.*, 108:210401, May 2012.

[38] I. Ferrier-Barbut, H. Kadau, M. Schmitt, M. Wenzel, and T. Pfau. Observation of quantum droplets in a strongly dipolar Bose gas. *Phys. Rev. Lett.*, 116(21):215301, 2016.

[39] L. Santos, G. V. Shlyapnikov, and M. Lewenstein. Roton-maxon spectrum and stability of trapped dipolar Bose-Einstein condensates. *Phys. Rev. Lett.*, 90(25):250403, 2003.

[40] L. C. Ha, L. W. Clark, C. V. Parker, B. M. Anderson, and C. Chin. Roton-maxon excitation spectrum of Bose condensates in a shaken optical lattice. *Phys. Rev. Lett.*, 114(5):055301, 2015.

[41] LD Landau. L. d. landau. *J. Phys. USSR*, 11:91, 1947.

[42] R. P. Feynman. Atomic theory of the two-fluid model of liquid Helium. *Phys. Rev.*, 94(2):262, 1954.

[43] P. Nozières. Superfluidity, Crystallization and Localization. *Journal of Low Temperature Physics*, 156(1-2):9–21, 2009.

[44] S. Komineas and N. R. Cooper. Vortex lattices in Bose-Einstein condensates with dipolar interactions beyond the weak-interaction limit. *Phys. Rev. A*, 75(2):023623, 2007.

[45] O. Dutta and P. Meystre. Unitary gas in an isotropic harmonic trap: Symmetry properties and applications. *Phys. Rev. A*, 74:053604, 2007.

[46] O. Dutta, R. Kanamoto, and P. Meystre. Stability of the density-wave state of a dipolar condensate in a pancake-shaped trap. *Phys. Rev. A*, 78(4):043608, 2008.

[47] A. Micheli, G. K. Brennen, and P. Zoller. A toolbox for lattice-spin models with polar molecules. *Nature Physics*, 2(5):341, 2006.

[48] B. Yan, S. A. Moses, B. Gadway, J. P. Covey, K. R. A. Hazzard, A. M. Rey, D. S. Jin, and J. Ye. Observation of dipolar spin-exchange interactions with lattice-confined polar molecules. *Nature*, 501(7468):521, 2013.

[49] I. Bloch. Ultracold quantum gases in optical lattices. *Nature Physics*, 1(1):23, 2005.

[50] A. De Paz, A. Sharma, A. Chotia, E. Marechal, J. H. Huckans, P. Pedri, L. Santos, O. Gorceix, L. Vernac, and B. Laburthe-Tolra. Nonequilibrium quantum magnetism in a dipolar lattice gas. *Phys. Rev Lett.*, 111(18):185305, 2013.

[51] S. Baier, M. J. Mark, D. Petter, K. Aikawa, L. Chomaz, Z. Cai, M. Baranov, P. Zoller, and F. Ferlaino. Extended bose-hubbard models with ultracold magnetic atoms. *Science*, 352(6282):201–205, 2016.

[52] J. R. Abo-Shaeer, C. Raman, J. M. Vogels, and W. Ketterle. Observation of vortex lattices in Bose-Einstein condensates. *Science*, 292(5516):476–479, 2001.

[53] M. W. Zwierlein, J. R. Abo-Shaeer, A. Schirotzek, C. H. Schunck, and W. Ketterle. Vortices and superfluidity in a strongly interacting Fermi gas. *Nature*, 435(7045):1047, 2005.

[54] Y. J. Lin, R. L. Compton, K. Jiménez-García, J. V. Porto, and I. B Spielman. Synthetic magnetic fields for ultracold neutral atoms. *Nature*, 462(7273):628, 2009.

[55] Y. J. Lin, K. Jiménez-García, and I. B. Spielman. Spin-Orbit-Coupled Bose-Einstein condensates. *Nature*, 471(7336):83, 2011.

[56] N. Q. Burdick, Y. Tang, and B. L. Lev. Long-lived Spin-Orbit-Coupled degenerate dipolar Fermi gas. *Phys. Rev. X*, 6:031022, Aug 2016.

[57] C. Zhang, S. Tewari, R. M. Lutchyn, and S. D. Sarma. $p_x + ip_y$ superfluid from s-wave interactions of fermionic cold atoms. *Phys. Rev. Lett.*, 101(16):160401, 2008.

[58] M. Sato, Y. Takahashi, and S. Fujimoto. Non-Abelian topological order in s-wave superfluids of ultracold fermionic atoms. *Phys. Rev. Lett.*, 103(2):020401, 2009.

[59] S. Nascimbène. Realizing one-dimensional topological superfluids with ultracold atomic gases. *Journal of Physics B: Atomic, Molecular and Optical Physics*, 46(13):134005, 2013.

[60] P. Wang, Z. Q. Yu, Z. Fu, J. Miao, L. Huang, S. Chai, H. Zhai, and J. Zhang. Spin-Orbit coupled degenerate Fermi gases. *Phys. Rev. Lett.*, 109(9):095301, 2012.

[61] L. W. Cheuk, A. T. Sommer, Z. Hadzibabic, T. Yefsah, W. S. Bakr, and M. W. Zwierlein. Spin-injection spectroscopy of a Spin-Orbit coupled Fermi gas. *Phys. Rev. Lett.*, 109(9):095302, 2012.

[62] C. Cohen-Tannoudji and W. D. Phillips. New mechanisms for laser cooling. *Phys. Today*, 43(10):33–40, 1990.

[63] M. Lu, N. Q. Burdick, and B. L. Lev. Quantum degenerate dipolar Fermi gas. *Phys. Rev. Lett.*, 108:215301, May 2012.

[64] W. C. Martin, R. Zalubas, and L. Hagan. Atomic energy levels-the Rare-Earth elements. The spectra of Lanthanum, Cerium, Praseodymium, Neodymium, Promethium, Samarium, Europium, Gadolinium, Terbium, Dysprosium, Holmium, Erbium, Thulium, Ytterbium, and Lutetium. Technical report, National Standard Reference Data System, 1978.

[65] A. Y. Cabezas, I. Lindgren, and R. Marrus. Atomic-beam investigations of electronic and nuclear ground states in the Rare-Earth region. *Phys. Rev.*, 122:1796–1801, Jun 1961.

[66] N. Leefer, L. Bougas, D. Antypas, and D. Budker. Towards a new measurement of parity violation in Dysprosium. *arXiv preprint arXiv:1412.1245*, 2014.

[67] W. Pauli and R. E. Peierls. *Phys. Z.*, 32:670, 1931.

[68] S. Kotochigova and A. Petrov. Anisotropy in the interaction of ultracold Dysprosium. *Phys. Chem. Chem. Phys.*, 13:19165–19170, 2011.

[69] H. Li, J. F. Wyart, O. Dulieu, S. Nascimbène, and M. Lepers. Optical trapping of ultracold Dysprosium atoms: transition probabilities, dynamic dipole polarizabilities and Van der Waals C_6 coefficients. *Journal of Physics B: Atomic, Molecular and Optical Physics*, 50(1):014005, 2017.

[70] N. R. Kestner. The theory of intermolecular forces, Volume 32 of International Series of Monographs on Chemistry by A. J. Stone (University of Cambridge). *Journal of the American Chemical Society*, 119(36):8584–8584, 1997.

[71] J. Weiner, V. S. Bagnato, S. Zilio, and P. S. Julienne. Experiments and theory in cold and ultracold collisions. *Rev. Mod. Phys.*, 71:1–85, Jan 1999.

[72] J. Dalibard. Collisional dynamics of ultra-cold atomic gases. In *Proceedings of the International School of Physics-Enrico Fermi*, volume 321, page 14, 1999.

[73] L. D. Landau and E. M. Lifshitz. *Quantum mechanics: non-relativistic theory*, volume 3. Elsevier, 2013.

[74] M. A Baranov. Theoretical progress in many-body physics with ultracold dipolar gases. *Physics Reports*, 464(3):71–111, 2008.

[75] R. Shakeshaft. Low energy scattering by the r^{-3} potential. *Journal of Physics B: Atomic and Molecular Physics*, 5(6):L115, 1972.

[76] B. Gao. Repulsive $1/r^3$ interaction. *Phys. Rev. A*, 59(4):2778, 1999.

[77] S. Giorgini, L. P. Pitaevskii, and S. Stringari. Theory of ultracold atomic Fermi gases. *Reviews of Modern Physics*, 80(4):1215, 2008.

[78] J. J McClelland and J. L Hanssen. Laser cooling without repumping: a magneto-optical trap for erbium atoms. *Phys. Rev. Lett.*, 96(14):143005, 2006.

[79] S. H. Youn, M. Lu, U. Ray, and B. L. Lev. Dysprosium magneto-optical traps. *Phys. Rev. A*, 82:043425, Oct 2010.

[80] A. Frisch, K. Aikawa, M. Mark, A. Rietzler, J. Schindler, E. Zupanič, R. Grimm, and F. Ferlaino. Narrow-line magneto-optical trap for Erbium. *Phys. Rev. A*, 85:051401, May 2012.

[81] T. Maier, H. Kadau, M. Schmitt, A. Griesmaier, and T. Pfau. Narrow-line magneto-optical trap for Dysprosium atoms. *Opt. Lett.*, 39(11):3138–3141, Jun 2014.

[82] Davide Dreon. *Designing and building an ultracold Dysprosium experiment: a new framework for light-spin interaction*. Theses, Ecole Normale Supérieure (ENS) ; PSL Research University, July 2017.

[83] D. Dreon, L. Sidorenkov, C. Bouazza, W. Maineult, J. Dalibard, and S. Nascimbene. Optical cooling and trapping of highly magnetic atoms: the benefits of a spontaneous spin polarization. *Journal of Physics B: Atomic, Molecular and Optical Physics*, 50(6):065005, 2017.

[84] T. H. Loftus, T. Ido, M. M. Boyd, A. D. Ludlow, and J. Ye. Narrow line cooling and momentum-space crystals. *Phys. Rev. A*, 70:063413, Dec 2004.

[85] M. Drewsen, Ph. Laurent, A. Nadir, G. Santarelli, A. Clairon, Y. Castin, D. Grison, and C. Salomon. Investigation of sub-doppler cooling effects in a Cesium magneto-optical trap. *Applied Physics B*, 59(3):283–298, Sep 1994.

[86] D. Boiron, A. Michaud, P. Lemonde, Y. Castin, C. Salomon, S. Weyers, K. Szymaniec, L. Cognet, and A. Clairon. Laser cooling of Cesium atoms in gray optical molasses down to 1.1 μk. *Phys. Rev. A*, 53:R3734–R3737, Jun 1996.

[87] T. Walker, D. Sesko, and C. Wieman. Collective behavior of optically trapped neutral atoms. *Phys. Rev. Lett.*, 64:408–411, Jan 1990.

[88] J. Vigué. Possibility of applying laser-cooling techniques to the observation of collective quantum effects. *Phys. Rev. A*, 34:4476–4479, Nov 1986.

[89] J. Weiner. *Cold and Ultracold Collisions in Quantum Microscopic and Mesoscopic Systems*. January 2004.

[90] S. Bali, D. Hoffmann, and T. Walker. Novel intensity dependence of ultracold collisions involving repulsive states. *EPL*, 27(4):273, 1994.

[91] P. Pillet, A. Crubellier, A. Bleton, O. Dulieu, P. Nosbaum, I. Mourachko, and F. Masnou-Seeuws. Photoassociation in a gas of cold alkali atoms: I. perturbative quantum approach. *Journal of Physics B: Atomic, Molecular and Optical Physics*, 30(12):2801, 1997.

[92] A. Fioretti, D. Comparat, A. Crubellier, O. Dulieu, F. Masnou-Seeuws, and P. Pillet. Formation of cold Cs_2 molecules through Photoassociation. *Phys. Rev. Lett.*, 80:4402–4405, May 1998.

[93] P. D. Lett, K. Helmerson, W. D. Phillips, L. P. Ratliff, S. L. Rolston, and M. E. Wagshul. Spectroscopy of Na_2 by photoassociation of laser-cooled Na. *Phys. Rev. Lett.*, 71:2200–2203, Oct 1993.

[94] L. Ratliff, K. Helmerson, P. Lett, and S. Rolston. High resolution molecular spectroscopy using laser cooled Sodium atoms. *Bulletin of the American Physical Society*, 38:1169WH8, May 1993.

[95] A. Gallagher and D. E. Pritchard. Exoergic collisions of cold Na-Na. *Phys. Rev. Lett.*, 63:957–960, Aug 1989.

[96] D. Sesko, T. Walker, C. Monroe, A. Gallagher, and C. Wieman. Collisional losses from a light-force atom trap. *Phys. Rev. Lett.*, 63:961–964, Aug 1989.

[97] P. S. Julienne and J. Vigué. Cold collisions of ground- and excited-state alkali-metal atoms. *Phys. Rev. A*, 44:4464–4485, Oct 1991.

[98] V. S. Letkhov and V. G. Minogin. Trapping and storage of atoms in a laser field. *Applied physics*, 17(1):99–103, Sep 1978.

[99] S. Chu, J. E. Bjorkholm, A. Ashkin, and A. Cable. Experimental observation of optically trapped atoms. *Phys. Rev. Lett.*, 57:314–317, Jul 1986.

[100] R. Grimm, M. Weidemuller, and Y. B. Ovchinnikov. Optical dipole traps for neutral atoms. volume 42 of *Advances In Atomic, Molecular, and Optical Physics*, pages 95–170. Academic Press, 2000.

[101] V. A. Dzuba, V. V. Flambaum, and B. L. Lev. Dynamic polarizabilities and magic wavelengths for Dysprosium. *Phys. Rev. A*, 83(3):032502, 2011.

[102] C. Ravensbergen, V. Corre, E. Soave, M. Kreyer, S. Tzanova, E. Kirilov, and R. Grimm. Accurate determination of the dynamical polarizability of Dysprosium. *arXiv preprint arXiv:1801.05658*, 2018.

[103] D. Guéry-Odelin, F. Zambelli, J. Dalibard, and S. Stringari. Collective oscillations of a classical gas confined in harmonic traps. *Phys. Rev. A*, 60(6):4851, 1999.

[104] A. Couvert, T. Kawalec, G. Reinaudi, and D. Guéry-Odelin. Optimal transport of ultracold atoms in the non-adiabatic regime. *EPL*, 83(1):13001, 2008.

[105] N. L. Manakov, V. D. Ovsiannikov, and L. P. Rapoport. Atoms in a laser field. *Physics Reports*, 141(6):320–433, 1986.

[106] W. Kao, Y. Tang, N. Q. Burdick, and B. L. Lev. Anisotropic dependence of tune-out wavelength near Dy 741-nm transition. *Opt. Express*, 25(4):3411–3419, Feb 2017.

[107] T. Maier. *Interactions in a Quantum Gas of Dysprosium Atoms*. PhD thesis, 2016.

[108] J. H. Becher, S. Baier, K. Aikawa, M. Lepers, J.-F. Wyart, O. Dulieu, and F. Ferlaino. Anisotropic polarizability of Erbium atoms. *Phys. Rev. A*, 97:012509, Jan 2018.

[109] T. Chalopin, V. Makhalov, C. Bouazza, A. Evrard, A. Barker, J. Dalibard, R. Lopes, and S. Nascimbene. Anisotropic light-shift and magic-polarization of the intercombination line of dysprosium atoms in a far-detuned dipole trap. *arXiv preprint arXiv:1805.06878*, 2018.

[110] N. Q Burdick, K. Baumann, Y. Tang, M. Lu, and B. L Lev. Fermionic suppression of dipolar relaxation. *Phys. Rev. Lett.*, 114(2):023201, 2015.

[111] B. Pasquiou. *Effets de l'interaction dipôle-dipôle sur les propriétés magnétiques d'un condensat de Chrome*. PhD thesis, Université Paris-Nord-Paris XIII, 2011.

[112] N. Masuhara, J. M. Doyle, J. C. Sandberg, D. Kleppner, T. J. Greytak, H. F. Hess, and G. P. Kochanski. Evaporative cooling of spin-polarized atomic Hydrogen. *Phys. Rev. Lett.*, 61(8):935, 1988.

[113] I. D. Setija, H. G. C. Werij, O. J. Luiten, M. W. Reynolds, T. W. Hijmans, and J. T. M. Walraven. Optical cooling of atomic Hydrogen in a magnetic trap. *Phys. Rev. Lett.*, 70:2257–2260, Apr 1993.

[114] K. M. Oâhara, M. E. Gehm, S. R. Granade, and J. E. Thomas. Scaling laws for evaporative cooling in time-dependent optical traps. *Phys. Rev. A*, 64(5):051403, 2001.

[115] C. Chin, R. Grimm, P. Julienne, and E. Tiesinga. Feshbach resonances in ultracold gases. *Reviews of Modern Physics*, 82(2):1225, 2010.

[116] M. Marinescu and L. You. Controlling atom-atom interaction at ultralow temperatures by dc electric fields. *Phys. Rev. Lett.*, 81(21):4596, 1998.

[117] PO Fedichev, Yu Kagan, GV Shlyapnikov, and JTM Walraven. Influence of nearly resonant light on the scattering length in low-temperature atomic gases. *Phys. Rev. Lett.*, 77(14):2913, 1996.

[118] M Theis, G Thalhammer, K Winkler, M Hellwig, G Ruff, R Grimm, and J Hecker Denschlag. Tuning the scattering length with an optically induced feshbach resonance. *Phys. Rev. Lett.*, 93(12):123001, 2004.

[119] T. Lahaye, J. Metz, B. Froehlich, T. Koch, M. Meister, A. Griesmaier, T. Pfau, H. Saito, Y. Kawaguchi, and M. Ueda. D-wave collapse and explosion of a dipolar Bose-Einstein condensate. *Phys. Rev. Lett.*, 101(8):080401, 2008.

[120] T. Maier, I. Ferrier-Barbut, H. Kadau, M. Schmitt, M. Wenzel, C. Wink, T. Pfau, K. Jachymski, and P. S. Julienne. Broad universal Feshbach resonances in the chaotic spectrum of Dysprosium atoms. *Phys. Rev. A*, 92:060702, Dec 2015.

[121] K. Baumann, N. Q. Burdick, M. Lu, and B. L. Lev. Observation of low-field Fano-Feshbach resonances in ultracold gases of Dysprosium. *Phys. Rev. A*, 89:020701, Feb 2014.

[122] A. Petrov, E. Tiesinga, and S. Kotochigova. Anisotropy-induced Feshbach resonances in a quantum dipolar gas of highly magnetic atoms. *Phys. Rev. Lett.*, 109:103002, Sep 2012.

[123] A. Frisch, M. Mark, K. Aikawa, F. Ferlaino, J. L. Bohn, C. Makrides, A. Petrov, and S. Kotochigova. Quantum chaos in ultracold collisions of gas-phase Erbium atoms. *Nature*, 507(7493):475, 2014.

[124] T. Maier, H. Kadau, M. Schmitt, M. Wenzel, I. Ferrier-Barbut, T. Pfau, A. Frisch, S. Baier, K. Aikawa, L. Chomaz, M. J. Mark, F. Ferlaino, C. Makrides, E. Tiesinga, A. Petrov, and S. Kotochigova. Emergence of chaotic scattering in ultracold Er and Dy. *Phys. Rev. X*, 5:041029, Nov 2015.

[125] C. Cohen-Tannoudji. Piégeage non dissipatif et refroidissement évaporatif. *Cours au Collège de France*, 86:87, 1996.

[126] O. J. Luiten, M. W. Reynolds, and J. T. M. Walraven. Kinetic theory of the evaporative cooling of a trapped gas. *Phys. Rev. A*, 53(1):381, 1996.

[127] Y. Tang, A. Sykes, N. Q Burdick, J. L. Bohn, and B. L. Lev. S-wave scattering lengths of the strongly dipolar bosons ^{162}Dy and ^{164}Dy. *Phys. Rev. A*, 92(2):022703, 2015.

[128] Y. J. Lin, K. Jiménez-García, and I. B. Spielman. Spin-Orbit-Coupled Bose-Einstein condensates. *Nature*, 471(7336):83, 2011.

[129] C. Weitenberg, M. Endres, J. F. Sherson, M. Cheneau, P. Schauß, T. Fukuhara, I. Bloch, and S. Kuhr. Single-spin addressing in an atomic Mott insulator. *Nature*, 471(7338):319, 2011.

[130] M. Kitagawa and M. Ueda. Squeezed spin states. *Phys. Rev. A*, 47(6):5138, 1993.

[131] R. Yamazaki, S. Taie, S. Sugawa, and Y. Takahashi. Submicron spatial modulation of an interatomic interaction in a Bose-Einstein condensate. *Phys. Rev. Lett.*, 105(5):050405, 2010.

[132] L. W. Clark, L. C. Ha, C. Y. Xu, and C. Chin. Quantum dynamics with spatiotemporal control of interactions in a stable Bose-Einstein condensate. *Phys. Rev. Lett.*, 115(15):155301, 2015.

[133] L. W. Clark, A. Gaj, L. Feng, and C. Chin. Collective emission of matter-wave jets from driven Bose-Einstein condensates. *Nature*, 551(7680):356, 2017.

[134] C. L. Kane and E. J. Mele. Quantum spin Hall effect in graphene. *Phys. Rev. Lett.*, 95(22):226801, 2005.

[135] C. L. Kane and E. J. Mele. $\mathbb{Z}_2$ topological order and the quantum spin hall effect. *Phys. Rev. Lett.*, 95(14):146802, 2005.

[136] M. König, S. Wiedmann, C. Brüne, A. Roth, H. Buhmann, L. W. Molenkamp, X. L. Qi, and S. C. Zhang. Quantum spin Hall insulator state in hgte quantum wells. *Science*, 318(5851):766–770, 2007.

[137] D. Hsieh, D. Qian, L. Wray, Y. Xia, Y. S. Hor, R. J. Cava, and M. Z. Hasan. A topological Dirac insulator in a quantum spin Hall phase. *Nature*, 452(7190):970, 2008.

[138] L. D. Landau. On the theory of phase transitions. *Ukr. J. Phys.*, 11:19–32, 1937.

[139] A. Kitaev. Periodic table for topological insulators and superconductors. In *AIP Conference Proceedings*, volume 1134, pages 22–30. AIP, 2009.

[140] A. P. Schnyder, S. Ryu, A. Furusaki, and A. W. W. Ludwig. Classification of topological insulators and superconductors. In *AIP Conference Proceedings*, volume 1134, pages 10–21. AIP, 2009.

[141] A. Kitaev. Unpaired Majorana fermions in quantum wires. *Physics-Uspekhi*, 44(10S):131, 2001.

[142] J. Bardeen, L. N. Cooper, and J. R. Schrieffer. Theory of Superconductivity. *Phys. Rev.*, 108:1175–1204, Dec 1957.

[143] M. A. Baranov, M. Dalmonte, G. Pupillo, and P. Zoller. Condensed matter theory of dipolar quantum gases. *Chemical Reviews*, 112(9):5012–5061, 2012.

[144] M. A. Baranov, M. S. Mar'enko, Val. S. Rychkov, and G. V. Shlyapnikov. Superfluid pairing in a polarized dipolar Fermi gas. *Phys. Rev. A*, 66:013606, Jul 2002.

[145] K. K. Ni, S. Ospelkaus, D. Wang, G. Quéméner, B. Neyenhuis, M. H. G. De Miranda, J. L. Bohn, J. Ye, and D. S. Jin. Dipolar collisions of polar molecules in the quantum regime. *Nature*, 464(7293):1324, 2010.

[146] S. A. Moses, J. P. Covey, M. T. Miecnikowski, D. S. Jin, and J. Ye. New frontiers for quantum gases of polar molecules. *Nature Physics*, 13(1):13, 2017.

[147] J. Zhang, E. G. M. Van Kempen, T. Bourdel, L. Khaykovich, J. Cubizolles, F. Chevy, M. Teichmann, L. Tarruell, S. Kokkelmans, and C. Salomon. P-wave Feshbach resonances of ultracold ^{6}Li. *Phys. Rev. A*, 70(3):030702, 2004.

[148] C. A. Regal, C. Ticknor, J. L. Bohn, and D. S. Jin. Tuning p-wave interactions in an ultracold Fermi gas of atoms. *Phys. Rev. Lett.*, 90(5):053201, 2003.

[149] J. P. Gaebler, J. T. Stewart, J. L. Bohn, and D. S. Jin. P-wave Feshbach molecules. *Phys. Rev. Lett.*, 98(20):200403, 2007.

[150] J. Fuchs, C. Ticknor, P. Dyke, G. Veeravalli, E. Kuhnle, W. Rowlands, P. Hannaford, and C. J. Vale. Binding energies of ^{6}Li p-wave Feshbach molecules. *Phys. Rev. A*, 77(5):053616, 2008.

[151] L. Jiang, T. Kitagawa, J. Alicea, A. R. Akhmerov, D. Pekker, G. Refael, J. I. Cirac, E. Demler, M. D. Lukin, and P. Zoller. Majorana fermions in equilibrium and in driven cold-atom quantum wires. *Phys. Rev. Lett.*, 106(22):220402, 2011.

[152] L. Huang, Z. Meng, P. Wang, P. Peng, S. L. Zhang, L. Chen, D. Li, Q. Zhou, and J. Zhang. Experimental realization of two-dimensional synthetic Spin-Orbit coupling in ultracold Fermi gases. *Nature Physics*, 12(6):540, 2016.

[153] V. Galitski and I. B. Spielman. Spin-Orbit coupling in quantum gases. *Nature*, 494(7435):49, 2013.

[154] I. S. Cojocaru, S. V. Pyatchenkov, S. A. Snigirev, I. A. Luchnikov, E. S. Kalganova, G. A. Vishnyakova, D. N. Kublikova, V. S. Bushmakin, E. T. Davletov, V. V. Tsyganok, O. V. Belyaeva, A. Khoroshilov, V. N. Sorokin, D. D. Sukachev, and A. V. Akimov. Light-assisted collisions in ultracold Tm atoms. *Phys. Rev. A*, 95:012706, Jan 2017.

[155] G. D. Telles, V. S. Bagnato, and L. G. Marcassa. Alternative to the Hyperfine-Change-Collision interpretation for the behavior of magneto-optical-trap losses at low light intensity. *Phys. Rev. Lett.*, 86:4496–4499, May 2001.

[156] K. Aikawa, S. Baier, A. Frisch, M. Mark, C. Ravensbergen, and F. Ferlaino. Observation of Fermi surface deformation in a dipolar quantum gas. *Science*, 345(6203):1484–1487, 2014.

[157] C. C. Bradley, J. J. McClelland, W. R. Anderson, and R. J. Celotta. Magneto-optical trapping of Chromium atoms. *Phys. Rev. A*, 61:053407, Apr 2000.

[158] J. G. Conway and E. F. Worden. Preliminary level analysis of the first and second spectra of Dysprosium, Dy i and Dy ii$*$. *J. Opt. Soc. Am.*, 61(6):704–726, Jun 1971.

[159] H. R. Sadeghpour, J. L. Bohn, M. J. Cavagnero, B. D. Esry, I. I. Fabrikant, J. H. Macek, and A. R. P. Rau. Collisions near threshold in atomic and molecular physics. *Journal of Physics B: Atomic, Molecular and Optical Physics*, 33(5):R93, 2000.

[160] S. Chaudhury, S. Merkel, T. Herr, A. Silberfarb, I. H. Deutsch, and P. S. Jessen. Quantum control of the hyperfine spin of a Cs atom ensemble. *Phys. Rev. Lett.*, 99(16):163002, 2007.

[161] F. W. Cummings. Stimulated emission of radiation in a single mode. *Phys. Rev.*, 140:A1051–A1056, Nov 1965.

[162] O. J. Luiten, M. W. Reynolds, and J. T. M. Walraven. Kinetic theory of the evaporative cooling of a trapped gas. *Phys. Rev. A*, 53(1):381, 1996.

[163] S. Hensler, J. Werner, A. Griesmaier, P. O. Schmidt, A. Görlitz, T. Pfau, S. Giovanazzi, and K. Rzażewski. Dipolar relaxation in an ultra-cold gas of magnetically trapped Chromium atoms. *Applied Physics B*, 77(8):765–772, 2003.

[164] F. Schreck, L. Khaykovich, K. L. Corwin, G. Ferrari, T. Bourdel, J. Cubizolles, and C. Salomon. Quasipure Bose-Einstein condensate immersed in a Fermi sea. *Phys. Rev. Lett.*, 87(8):080403, 2001.

[165] Z. Hadzibabic, C. A. Stan, K. Dieckmann, S. Gupta, M. W. Zwierlein, A. Görlitz, and W. Ketterle. Two-species mixture of quantum degenerate Bose and Fermi gases. *Phys. Rev. Lett.*, 88(16):160401, 2002.

[166] N. Goldman, J. C. Budich, and P. Zoller. Topological quantum matter with ultracold gases in optical lattices. *Nature Physics*, 12(7):639, 2016.

[167] O. Dutta and M. Lewenstein. Unconventional superfluidity of fermions in Bose-Fermi mixtures. *Phys. Rev. A*, 81(6):063608, 2010.

[168] J. Y. Zhang, S. C. Ji, Z. Chen, L. Zhang, Z. D. Du, B. Yan, G. Pan, B. Zhao, Y. J. Deng, H. Zhai, S. Chen, and J. W. Pan. Collective dipole oscillations of a Spin-Orbit Coupled Bose-Einstein condensate. *Phys. Rev. Lett.*, 109:115301, Sep 2012.

[169] Y. Li, G. Italo Martone, and S. Stringari. Sum rules, dipole oscillation and spin polarizability of a Spin-Orbit coupled quantum gas. *EPL*, 99(5):56008, 2012.

[170] T. L. Ho and S. Zhang. Bose-Einstein Condensates with Spin-Orbit interaction. *Phys. Rev. Lett.*, 107:150403, Oct 2011.

[171] Y. Li, L. P. Pitaevskii, and S. Stringari. Quantum tricriticality and phase transitions in Spin-Orbit coupled Bose-Einstein Condensates. *Phys. Rev. Lett.*, 108:225301, May 2012.

[172] E. Majorana. Atomi orientati in campo magnetico variabile. *Il Nuovo Cimento (1924-1942)*, 9(2):43–50, Feb 1932.

[173] B. Lian, T. L. Ho, and H. Zhai. Searching for non-Abelian phases in the Bose-Einstein condensate of Dysprosium. *Phys. Rev. A*, 85:051606, May 2012.

[174] J. D. Koralek, C. P. Weber, J. Orenstein, B. A. Bernevig, S. C. Zhang, S. Mack, and D. D. Awschalom. Emergence of the persistent spin helix in semiconductor quantum wells. *Nature*, 458(7238):610, 2009.

[175] B. A. Bernevig, J. Orenstein, and S. C. Zhang. Exact SU(2) symmetry and persistent spin helix in a spin-orbit coupled system. *Phys. Rev. Lett.*, 97:236601, Dec 2006.

Résumé

Dans le cadre de cette thèse, j'ai étudié le refroidissement et le piégeage d'un gaz d'atomes de Dysprosium dans des potentiels lumineux. Cet atome lanthanide possède dans son état électronique fondamental un moment magnétique très élevé, permettant l'exploration du domaine des gaz dipolaires ultrafroids. Ce caractère dipolaire enrichit la gamme des phénomènes physiques réalisés expérimentalement, en tirant avantage de la nature anisotrope et à longue-portée de l'interaction entre dipôles magnétiques. De plus, grâce à sa structure électronique riche, le Dysprosium offre la possibilité de créer un fort couplage entre le spin atomique et des champs lumineux, tout en gardant un taux de chauffage faible par rapport au cas usuel des atomes alcalins. Ceci ouvre la voie vers l'implémentation de champs de jauge artificiels, qui suscitent un vif intérêt dans le domaine des atomes froids dans un contexte de simulation quantique. Ce travail de thèse, consiste en l'étude des mécanismes d'interactions dans un gaz de Dysprosium ultrafroid, allant des collisions assistées par la lumière à la relaxation dipolaire en passant par le refroidissement par évaporation. J'expose également la réalisation expérimentale d'un champ magnétique effectif en utilisant un déplacement lumineux dépendant du spin, permettant de contrôler optiquement la force des interactions atomiques au moyen d'une résonance de Feshbach.

Mots Clés

atomes froids, dysprosium, gaz dipolaire.

Abstract

In this thesis, I present the study of the laser trapping and cooling of a Dysprosium atomic gas. This latter belong to the lanthanide family, it exhibits a large angular momentum in its electronic ground state, making it a suitable candidate for investigating dipolar quantum gases. These systems present a major interest as they can lead to the observation of novel quantum phenomena thanks to the anisotropic and long-range character of the interaction between magnetic dipoles. Moreover, Dysprosium has a rich electronic structure offering the possibility to implement strong light-spin coupling with a reduced heating with respect to alkali species, which paves the way toward the realization of synthetic gauge fields. In this work, I present the experimental investigation of different interaction mechanisms occurring in an ultracold gas of Dysprosium, ranging from light-assisted collisions to dipolar relaxation and evaporative cooling. I expose also the experimental realization of an effective magnetic field, using spin-dependent light-shift, allowing optical control over atomic interactions by means of Feshbach resonances.

Keywords

cold atoms, dysprosium, dipolar gases.